

Advancements in Nanomechanical Characterization and Biomolecular Imaging with Atomic force Microscopy

Présentée le 24 mai 2024

Faculté des sciences et techniques de l'ingénieur
Laboratoire de bio- et nano-instrumentation
Programme doctoral en biotechnologie et génie biologique

pour l'obtention du grade de Docteur ès Sciences

par

Veronika CENCEN

Acceptée sur proposition du jury

Prof. M. Dal Peraro, président du jury
Prof. G. Fantner, directeur de thèse
Prof. A. Roux, rapporteur
Dr A. Pyne, rapporteuse
Prof. J. McKinney, rapporteur

"I want to do something splendid before I go into my castle, something heroic, or wonderful—I don't know what, but I'm on the watch for it"

— Louisa May Alcott (Little Women)

Acknowledgements

When embarking on a PhD, one would always expect it to represent a major part of their early career, and have a significant impact on their life. However, I could never have envisioned the number of valuable connections, unexpected events, and valuable lessons in life that I encountered during my near-6-year journey with LBNI. After spending most of my youth moving to different countries every few years, a PhD seemed like a true commitment, but my desire to continue learning and the welcoming atmosphere of the lab persuaded me that I was making the right decision.

Firstly, I would like to thank my supervisor, Prof. Georg Fantner, for providing continuous guidance and opportunities for growth, encouraging independence even when I was in doubt of my own abilities. I extend my appreciation to my thesis examiners: Dr. Alice Pyne, Prof. Aurélien Roux, Prof. John McKinney and Prof. Matteo dal Peraro, for their valuable input before and during the defense.

Most of my thesis work would not have been possible without my collaborators. It was a pleasure to work closely with Cem Tekin, Vincenzo Caroprese, and Prof. Maartje Bastings on several projects involving the observation of self-assembly with high-speed AFM. I was also happy to work with Markku Hakala and Prof. Aurélien Roux from UNIGE on what I consider a challenging but very promising start on a project aiming to observe clathrin-mediated endocytosis with AFM in real time.

I was very lucky to have the patience and support of my senior colleagues at LBNI: Nahid Hosseini, Marcos Penedo, and Jiao Fang, who supported me through successes and challenges that come during the PhD. I am also thankful for the company and collaboration of past and current members of LBNI: Mélanie Hannebelle, Santiago Andany, Mustafa Kangül, Matthias Neuenschwander, Samuel Leitao, Bahareh Ghadiani, Navid Asmari, Esther Räth, Prabhu Prasad Swain, Augoustina Economou, Asal Ayar, Yiwei Zheng, Barney Drake, Ekin Asim Özek, Amanda Kläger, Federica Teodoro, Raphael Zingg, Gustavo Rocha, Ingrid Margot, Anouk Hein, and Lena Ong.

As most of my first few years were spent working in the bio-lab thanks to the trust of Prof. Aleksandra Radenovic, I was happy to have made connections and friends with the members of LBEN, in particular Eveline Mayner and Nathan Ronceray; I would like to specifically thank Vytautas Navikas for being a great quasi-colleague, mentor and friend during a difficult start of my PhD journey.

I cannot even begin to express how grateful I am for the support of my friends in Lausanne. Whether or not the connection was temporary, each one of you has helped me stay motivated in some way. Particularly in the last few years of my time at EPFL, I had the privilege to meet

some of the kindest and most interesting people of my life. I'm grateful to Laura Grasemann for the adventures we shared combining sports with an academic career; to members of the LANES lab for the eventful lunch breaks; to Riccardo Chiesa for staying by my side even when I was being difficult; to Cristian de Giorgio for always being up for spontaneous plans, to Arya Agarwal for being one of my first friends in chaos; to Raphael Zingg for the great times spent on the running trails; to Yuji for being a fellow appreciator of loud music in the office; and to Asya Dolgikh and other members of the Girl Dinner for the girlboss energy.

I am also able to say with confidence that some friendships are not restricted by distance or time. Although we spend most of our time in completely separate countries or even continents, I was always thankful for the remote support of my middle school bestie Paula Ripatti, my childhood forever friend Kaja Plesnik, my Hong-Kong era connections Oriana Jovanovic and Alec Nicol, Marci Meszaros, Zsofi Pluhar and the rest of the Budapest squad, and Massimiliano Berardi at conferences and through PhD-related memes.

I want to give a special mention to Roxana, Francesca, Edoardo and Diego, for bringing me energy and support when I needed it most, to push through even the hardest of times, and for giving me a new perspective on life.

Finally, and most importantly, I would like to thank my family: Marjan, Lilijana, Eva and Karolina, for always standing by my side unconditionally, for never having expectations yet always having faith in me, and for giving me no doubts that I am always welcome at home.

Abstract

Atomic force microscopy (AFM) is a widely used imaging tool for obtaining a variety of information for a range of samples. Although it was initially intended to serve as a method of observing very flat solid surfaces, its use expanded into several other fields, such as high-speed biomolecular imaging, mechanical property measurement, and sample disruption. As a result, AFM continues to be an indispensable tool in research, contributing significantly to advancements in nanotechnology, biophysics, materials science, and numerous other interdisciplinary domains.

In this work, we apply a specific mode of high-speed AFM (HS-AFM) imaging called photothermal off-resonance tapping mode (PORT), which allows us to directly control the forces exerted on the sample. We use this method to image 2D assembly of DNA 3-point stars (3PS) to investigate the impact of structural flexibility and binding strength in the growth of supramolecular networks.

We then use a variation of slow off-resonance imaging called force volume to obtain the mechanical properties of biological membranes for organs-on-a-chip. We compare the utility and reliability of AFM to the bulge test assessment for known samples as well as a membrane aimed at mimicking the extracellular matrix (ECM) scaffold of in vivo barriers of lung tissue.

In the penultimate chapter, we demonstrate promising preliminary data on imaging clathrin mediated endocytosis on unroofed cells with AFM, and the effects of using cholesterol depletion to modify the biological process.

Finally, we discuss the contributions and remaining challenges related to imaging dynamic bioprocesses in vitro and in-vivo, particularly with the use of PORT. Through further development of individual AFM components, such as the cantilever, scanner, controller, and software, and combining them with fluorescent microscopy, we hope to obtain valuable information on self-assembling biosamples that would not be possible with other imaging methods.

Keywords: Atomic force microscopy, photothermal off-resonance tapping mode, self-assembly, clathrin, Young's Modulus, DNA

Résumé de Thèse

La microscopie à force atomique (AFM) est un outil d'imagerie largement utilisé pour obtenir diverses informations sur une gamme d'échantillons. Bien qu'elle ait été initialement conçue pour servir de méthode d'observation des surfaces solides très lisses, son utilisation s'est étendue à plusieurs autres domaines tels que l'imagerie biomoléculaire à haute vitesse, la mesure des propriétés mécaniques et la perturbation d'échantillons. En conséquence, l'AFM continue d'être un outil indispensable dans la recherche, contribuant de manière significative aux progrès en nanotechnologie, biophysique, science des matériaux, et de nombreux autres domaines interdisciplinaires.

Dans ce travail, nous appliquons un mode spécifique de microscopie à force atomique à haute vitesse (HS-AFM) appelé mode de tapping hors résonance photothermique (PORT), qui nous permet de contrôler directement les forces exercées sur l'échantillon. Nous utilisons cette méthode pour imager l'assemblage en 2D d'étoiles à 3 points d'ADN (3PS) afin d'étudier l'impact de la flexibilité structurelle et de la force de liaison dans la croissance de réseaux supramoléculaires.

Ensuite, nous utilisons une variante de l'imagerie hors résonance lente appelée volume de force pour obtenir les propriétés mécaniques des membranes biologiques destinées à des organes-sur-puce. Nous comparons l'utilité et la fiabilité de l'AFM pour l'évaluation du test de bombement pour des échantillons connus ainsi qu'une membrane visant à imiter l'échafaudage de la matrice extracellulaire (ECM) des barrières in vivo du tissu pulmonaire.

Dans l'avant-dernier chapitre, nous présentons des données préliminaires prometteuses sur l'imagerie de l'endocytose médiée par la clathrine sur des cellules décapées avec l'AFM, et les effets de l'épuisement du cholestérol sur la modification du processus biologique. Enfin, nous discutons des contributions et des défis restants liés à l'imagerie des processus biologiques dynamiques in vitro et in vivo, en particulier avec l'utilisation du PORT. En développant davantage les composants individuels de l'AFM, tels que le levier, le scanner, le contrôleur et le logiciel, et en les combinant avec la microscopie fluorescente, nous espérons obtenir des informations précieuses sur l'auto-assemblage de échantillons biologiques qui ne seraient pas possibles avec d'autres méthodes d'imagerie.

Mots-clés : Microscopie à force atomique, mode de « photothermal off-resonance tapping », auto-assemblage, clathrine, module d'Young, ADN

Zusammenfassung

Die Rasterkraftmikroskopie (AFM) ist ein weit verbreitetes bildgebendes Werkzeug, um eine Vielzahl von Informationen für verschiedene Proben zu erhalten. Obwohl es ursprünglich dazu gedacht war, als Methode zur Beobachtung sehr flacher, fester Oberflächen zu dienen, hat sich ihr Einsatz auf verschiedene andere Bereiche ausgedehnt, wie z.B. die biomolekulare Hochgeschwindigkeitsbildgebung, die Messung mechanischer Eigenschaften und die Probenstörung. Als Ergebnis bleibt die AFM ein unverzichtbares Werkzeug in der Forschung, das erheblich zu Fortschritten in Nanotechnologie, Biophysik, Materialwissenschaften und zahlreichen anderen interdisziplinären Bereichen beiträgt.

In dieser Arbeit wenden wir einen spezifischen Modus der Hochgeschwindigkeits-AFM (HS-AFM)-Bildgebung namens Photothermal Off-Resonance Tapping Mode (PORT) an, die es uns ermöglicht, die auf die Probe ausgeübten Kräfte direkt zu steuern. Wir verwenden diese Methode, um die 2D-Anordnung von DNA-3-Punkt-Sternen (3PS) abzubilden und den Einfluss von struktureller Flexibilität und Bindungsstärke auf das Wachstum supramolekularer Netzwerke zu untersuchen.

Anschließend verwenden wir eine Variante der langsamen Off-Resonanz-Bildgebung namens Force Volume, um die mechanischen Eigenschaften biologischer Membranen für organ-on-a-chip Anwendungen zu erhalten. Wir vergleichen die Nützlichkeit und Zuverlässigkeit der AFM mit der Bewertung des Bulge-Tests für bekannte Proben sowie einer Membran, die darauf abzielt, die extrazelluläre Matrix (ECM) von in vivo Barrierefunktionen des Lungengewebes zu imitieren.

Im vorletzten Kapitel präsentieren wir vielversprechende vorläufige Daten zur Bildgebung der durch Clathrin vermittelten Endozytose an unroofed Zellen mittels AFM sowie den Effekten der Verwendung von Cholesterinzugsmethoden zur Modifikation des biologischen Prozesses. Abschließend diskutieren wir die Beiträge und verbleibenden Herausforderungen im Zusammenhang mit der Bildgebung dynamischer Bioprozesse in vitro und in vivo, insbesondere unter Verwendung von PORT. Durch die weitere Entwicklung einzelner AFM-Komponenten wie Hebel, Scanner, Controller und Software und deren Kombination mit Fluoreszenzmikroskopie hoffen wir, wertvolle Informationen über selbstassemblierende b zu erhalten, die mit anderen Bildgebungsmethoden nicht möglich wären.

Schlüsselwörter: Rasterkraftmikroskopie, photothermischer Off-Resonance-Tapping-Modus, Selbstorganisation, Clathrin, Elastizitätsmodul, DNA

Table of Contents

Acknowledgements.....	ii
Abstract.....	v
Résumé de Thèse	vii
Zusammenfassung	ix
1. Introduction	1
1.1 General introduction.....	1
1.2 AFM imaging modes	3
1.2.1 Contact Mode	4
1.2.2 Resonant Modes	5
1.2.3 Off-Resonance Tapping Modes.....	8
1.3 HS-AFM	11
1.4 Use of AFM to measure mechanical properties	14
1.4.1 Dynamic modes.....	15
1.4.2 Quasi-static	16
1.4.3 Off-Resonance Modes.....	17
1.5 Use of AFM for imaging DNA	19
1.5.1 Surface preparation	20
1.5.2 DNA Nanotechnology.....	20
1.5.3 Dynamic Imaging.....	22
1.6 Use of AFM in Self-Assembly	23
1.6.1 Nucleation and Growth Models.....	23
1.6.2 Use of AFM for Biological Self-Assembly	25
Contribution of the thesis	26
2. High-Speed AFM Imaging Of DNA Three-Point-Star Motif Self Assembly Using Photothermal Off-Resonance Tapping	28
Summary:.....	28
Abstract:.....	29
Introduction:	29
Protocol:.....	31
Representative results:	41

Discussion:	47
Acknowledgments:.....	51
3. Structural flexibility dominates over binding strength for supramolecular crystallinity	52
Abstract.....	52
Introduction	53
Results and discussion	56
Characterization of macromolecules with variation in structural flexibility.	56
Decoupling the contribution of intermolecular affinity.....	59
Exploring the self-assembly mechanisms in real time.....	62
Interface flexibility as determinant for stable nucleus formation.....	66
Restoring the interface rigidity.	70
Discussion.....	73
Methods.....	75
Preparation of DNA 3PS motifs.....	75
Static AFM imaging.	76
HS-AFM imaging.....	76
Automated analyses of assembled networks.	76
OxDNA simulations.	77
Patchy-particle simulations.....	77
4. Mechanical properties of soft biological membranes for organ-on-a-chip assessed by bulge test and AFM.....	79
Abstract.....	79
Introduction	80
Materials and Methods.....	82
Production of the CE-membrane and chip fabrication.....	82
Bulge test	83
AFM.....	84
Thickness measurement	85
Cell culture	85
Immunofluorescence	86
Cell shape analysis	86
Statistics	87

Results.....	87
Formation of vitrified and hydrogel CE-membranes	87
Mechanical characterization of thin membranes: AFM vs. bulge test	88
Impact of CE ratio and gelation temperature on the mechanical properties of the membranes.....	90
Impact of stiffness on cell spreading	91
Discussion.....	93
Conclusion.....	96
Acknowledgments.....	97
Supplementary Figures	98
5. AFM imaging of Clathrin Mediated Endocytosis.....	107
5.1 Introduction	107
5.1.1 Clathrin mediated endocytosis	107
5.1.2 Imaging of unroofed cells	109
5.2 Methods.....	110
5.2.1 Unroofing	110
5.2.2 AFM imaging	110
5.3 Results.....	111
5.4 Discussion and future work.....	115
6. Discussion and future work	117
6.1 Contributions of the thesis and remaining challenges	117
6.1.1 Setting Parameters in PORT	117
6.1.2 Use of PORT for imaging self assembly.....	119
6.1.3 Imaging of self-assembling structures in-vivo membrane.....	120
6.2 Closing Statement	121
Appendix	123
Supplementary Information to Chapter 3	123
Extended Methods.....	123
Supplementary Figures and Tables	130
Supplementary Movies	146
References	147
Curriculum Vitae	184

Table of Figures

Figure 1.1 (OBD schematic):	2
Figure 1.2 (AFM modes):.....	4
Figure 1.3(PORT setup):	7
Figure 1.4 (ORT interaction curve):.....	9
Figure 1.5(PORTinteraction):	11
Figure 1.6 (HS-AFM setup):.....	14
Figure 1.7 (Force separation curve):	16
Figure 1.8 (AFM indentation):.....	19
Figure 1.9 (Nucleation Pathway):.....	24
Figure 2.1 (The HS-AFM setup.):	37
Figure 2.2 (DNA 3PS sample imaged with AC10 at 100 kHz PORT rate at different line rates):.....	42
Figure 2.3 (Cantilever deflection, interaction curve, and image quality at 100 KHz and 500 kHz PORT rates):	43
Figure 2.4 (Effect of peak-to-peak AC input voltage DC offset input voltage):	46
Figure 3.1 (Steady-state assembly of hexagonal lattices formed by short and long 3PS):.....	58
Figure 3.2 (Quantifying the effect of intermolecular affinity on network crystallinity):	61
Figure 3.3 (HS-AFM detection of 2 distinct growth mechanisms):.....	65
Figure 3.4 (Importance of interface flexibility):	69
Figure 3.5 (Restoration of peripheral rigidity):	72
Figure 4.1 (Fabrication procedure of the hydrogel and vitrified CE-membranes.):	88
Figure 4.2 (Mechanical characterization of biological membranes):	90
Figure 4.3 (Mechanical characterization of biological membranes as a function of protein ratio):	91
Figure 4.4 (Effect of the substrate stiffness on cell spreading):	92
Figure 4.5 (Chip design):	98
Figure 4.6 (Thickness of the vitrified and hydrogel-based biological membranes):.....	99
Figure 4.7 (Representative image of a hydrogel CE-membrane at rest and after exposure to a negative pressure of -1.1 kPa):	100
Figure 4.8 (Determination of the Young's modulus based on the pressure-deflection curve of the hydrogel CE-membrane):.....	101
Figure 4.9 (Impact of the storage of the vitrified CE-membrane on its mechanical properties):	102
Figure 4.10 (Impact of a 2-weeks immersion in physiological medium on the mechanical properties of the vitrified CE-membrane):	103
Figure 4.11 (Force-volume image and force curves obtained by AFM):.....	104
Figure 4.12 (Young Modulus variance measured by AFM):.....	105
Figure 4.13 (Membrane production: Impact of the gelation temperature on the Young's modulus during the production of the hydrogel CE-membrane):	106

Figure 5.1 (Imaging clathrin on unroofed fixed cells):	112
Figure 5.2 (Effects of cholesterol depletion on imaging clathrin on unroofed cells):	114
Figure 6.1 (Clathrin triskelia covering a mica surface imaged on the high-speed AFM):	120

Supplementary Figures:

Figure 7.1:	130
Figure 7.2:	131
Figure 7.3:	132
Figure 7.4:	133
Figure 7.5:	134
Figure 7.6:	135
Figure 7.7:	136
Figure 7.8:	136
Figure 7.9:	137
Figure 7.10:	138
Figure 7.11:	139
Figure 7.12:	140
Figure 7.13:	141
Figure 7.14:	141
Figure 7.15:	142

Table 7-1.	143
-----------------	-----

1. Introduction

1.1 General introduction

Atomic force microscopy (AFM) has emerged as an extension of STM that, rather than being restricted to conductive sample, can be used for probing a wider range of samples in the nanoscale world with remarkable precision and sensitivity. Since its first published mention in 1986¹, AFM has evolved from a simple imaging technique²⁻⁷ to a versatile platform capable of investigating a variety of properties, such as electrical⁸, magnetic⁹, mechanical¹⁰. Its ability to visualize and manipulate nanoscale structures has opened up new avenues of research in diverse scientific fields, such as in material science¹¹, life science¹², surface science¹³, and others.

Most optical microscopy techniques, limited by the diffraction barrier, proved inadequate in resolving structures and dynamics beyond the optical resolution¹⁴. AFM, operating on the principles of force interactions between a sharp probe and the sample surface, transcended these limitations and offered a relatively non-destructive means to visualize and manipulate nanoscale features.

While there exists a variety of configurations of the AFM, the basic configuration and operating principle is similar: a nanometer-scale cantilever, usually with a sharp tip, is raster-scanned across a sample, giving information on the sample's topography (and potentially other properties, which will be discussed later). Originally and most commonly, a piezo is used to move the cantilever or sample stage.¹⁵ For readout, the most common technique in AFM remains the optical beam deflection (OBD)¹⁶, as it is relatively easy to implement (compared

to interferometer-based readout)¹⁷, and is capable of achieving sub-angstrom resolution. In OBD, we measure the angle change at the free end of the cantilever using a laser focused on its back side. The information obtained from this signal depends on the AFM imaging mode. The principle of OBD in a conventional AFM setup is shown in **Error! Reference source not found.a**, there the method to sense the change in deflection is based on sensing the change in angle of the laser reflected off the cantilever.

When using small cantilevers for HS-AFM, the OBD setup is different than in standard AFM setups, particularly because the laser spot size must be reduced. The schematic of polarization based OBD for small lever heads is shown in Figure 1.1b) below

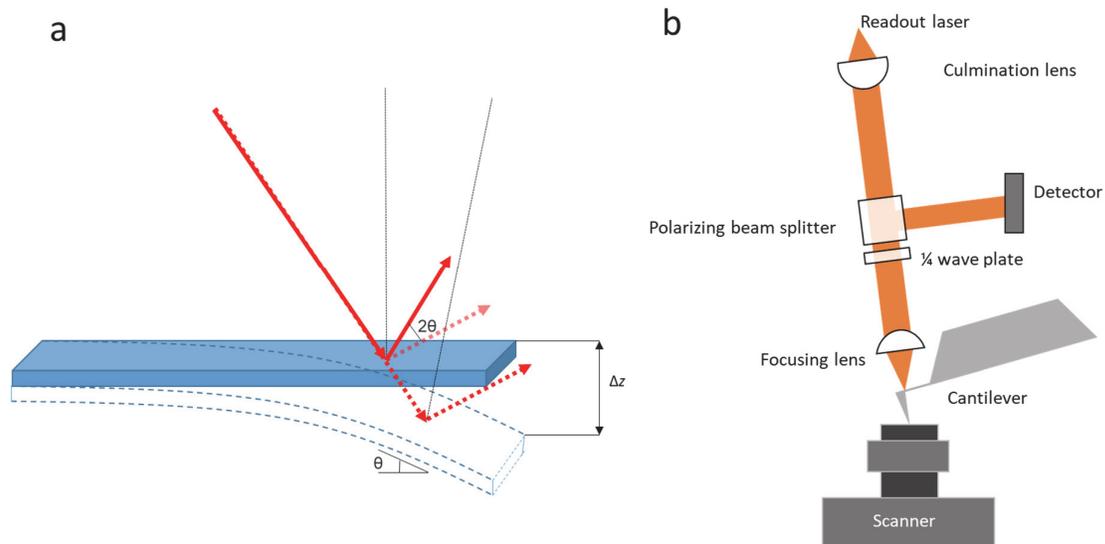


Figure 1.1 (OBD schematic): a) A schematic of OBD in conventional AFM, based on ¹⁸; When the cantilever is deflected downwards, the laser spot shifts towards the end of the cantilever. The key effect of this is the change of the angle of the reflected laser beam by 2θ (θ is the cantilever bending angle at the laser spot). The closer the laser spot is to the end of the cantilever, the more sensitive it will be to the change in deflection. b) Schematic of polarization based OBD for small lever heads; The readout laser is passed through another lens before being reflected off the cantilever to improve focus.

1.2 AFM imaging modes

Contact mode AFM imaging was useful for basic topography imaging, and eventually allowed for research to progress into imaging methods that would allow for faster and/or gentle imaging of samples. The evolution of AFM technologies has led to the development of several specialized AFM modes¹⁹, some of which, for example, were intended to reduce the lateral force damage to the sample (such as dynamic resonant modes²⁰ and non-contact modes²¹), improve control over tip-sample forces (off-resonance modes²²), or image properties other than the topography (magnetic force microscopy²³, electrical modes²⁴, and electrochemical AFM²⁵). The operating principles of the three basic different modes are summarized in Figure 1.2.

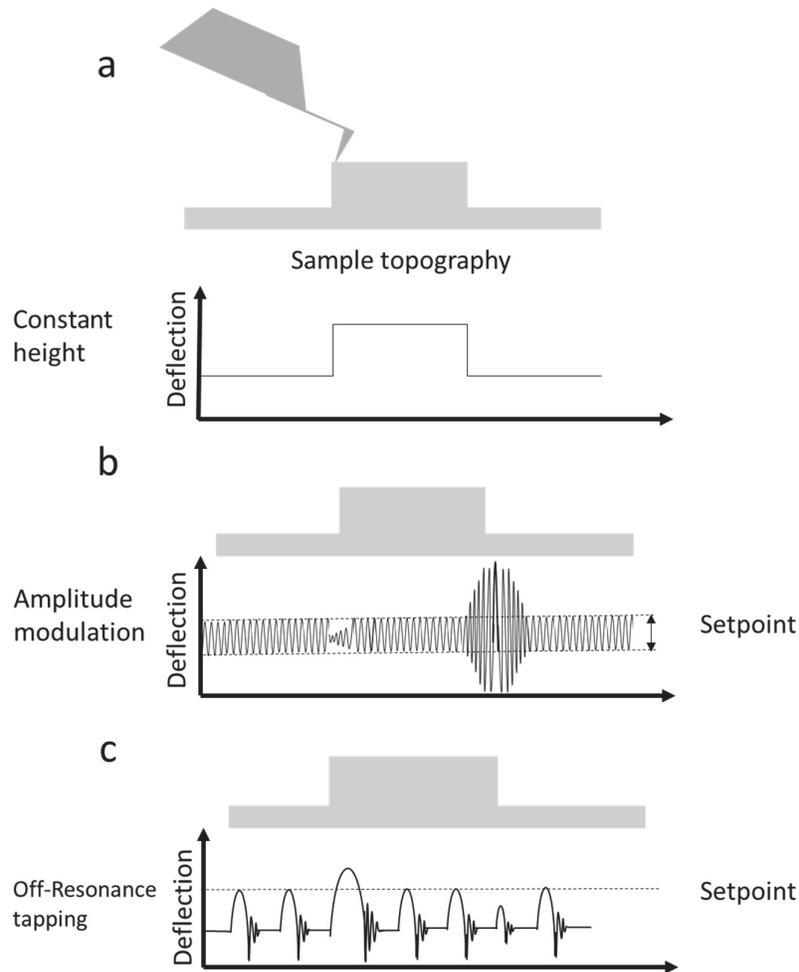


Figure 1.2 (AFM modes): The motion of the cantilever and the resulting feedback in a) static, b) dynamic, and c) off-resonance dynamic AFM modes in AFM. In a), the deflection of the cantilever is shown in contact mode; b) shows the change in tapping amplitude as the cantilever reaches the step (reduced amplitude until correction) and comes back down from it (increased amplitude until correction). c) shows the interaction curve motion of the cantilever in off-resonance tapping modes.

1.2.1 Contact Mode

Static or contact mode is the simplest mode of operating the AFM; as shown in Figure 1.2a), the probe is always in contact with the surface, and the feedback parameter is the cantilever

deflection as it scans over the topography. A feedback controller keeps the deflection constant at a specific set point. The required z output of the feedback loop to maintain a constant deflection provides information on the topography. The residual deviation of the deflection from the setpoint due to topography are shown as an error image. While this mode benefits from its simplicity, shear forces can damage fragile samples.²⁶ It is also possible to image in constant height, where the probe is maintained at a fixed height, and there is no force feedback, the recorded deflection while scanning the surface can be translated to a topographical image. This is sometimes used for atomic resolution but is otherwise uncommon.

1.2.2 Resonant Modes

In resonant dynamic modes, the cantilever oscillates at or close to the resonance frequency by means of, for example, a shaker piezo. The earliest resonant mode images were taken in air, and aimed at reducing sample damage due to drag forces which are commonly present in contact mode.²⁰ This was soon after expanded to imaging in liquid³⁵, and became popular for imaging biological samples. In amplitude modulation (AM-AFM) shown in Figure 1.2b), the feedback parameter is the oscillation amplitude. As the cantilever approaches the surface, the amplitude is reduced, and this change is used by the feedback loop to maintain a constant amplitude setpoint. The required z output of the feedback loop to maintain a constant amplitude provides information on the topography.

Because the oscillation amplitude is the feedback process variable, a reliable and stable excitation method is paramount to obtain high quality measurements. Over the years, a number

of excitation schemes have been developed. Of these excitation schemes, inertial piezo excitation and photothermal³⁶ excitation are most widely used. There are, however, also other methods of actuation, such as magnetic³⁷ and electrostatic³⁸

Photothermal Actuation

Photothermal actuation of cantilevers in AFM was first used in air³⁹, but is now also heavily used for imaging in liquid³⁶. In this method, a secondary laser is focused on the cantilever, as shown in Figure 1.3. The intensity of that laser is modulated at the driving frequency of the cantilever causing the cantilever to resonate. This is due to the bimorph effect, achieved, for example by temperature-sensitive bending of metal-coated silicon nitride cantilevers, caused by the different coefficients of thermal expansion. The efficiency is therefore very dependent on the design on the cantilever. For example, by changing the cross section from rectangular to trapezoidal changes the drive efficiency.⁴⁰ The drive efficiency can also be improved by adding a thin amorphous carbon layer to the cantilever to increase the absorption of the drive laser.⁴¹

The photothermal mechanism excites the cantilever with a single resonance peak, and does not couple to other system resonances, making imaging in fluid more convenient. The primary benefit of this is avoiding the “forest of peaks” usually present in piezo-actuated methods, and instead having one clean excitation peak even in fluids.

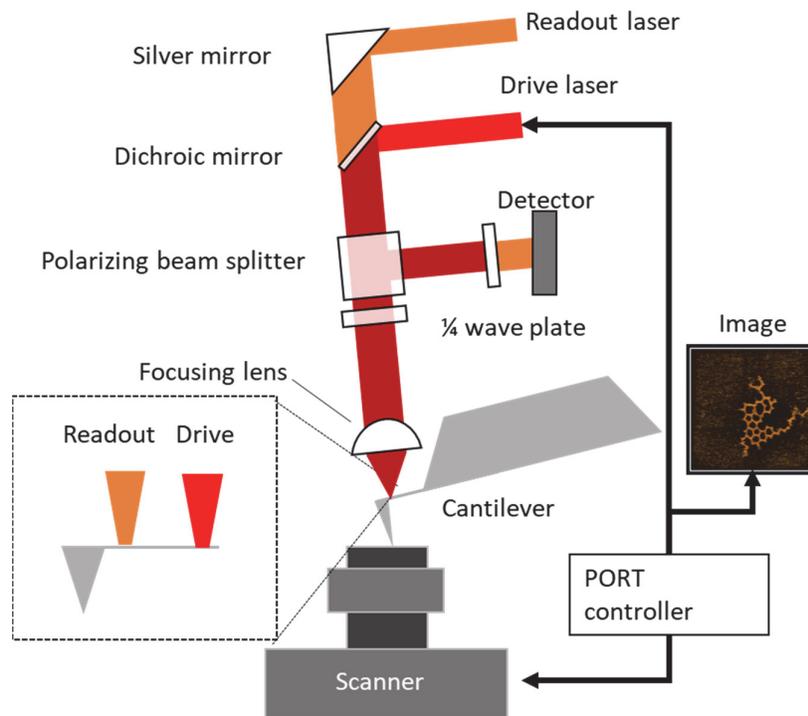


Figure 1.3 (PORT setup): In photothermal excitation, a secondary laser (in our case emitting at 685 nm) is used to actuate the cantilever, while a dedicated PORT controller is employed to discern the interactions between the tip and the sample. This information is derived from the deflection of a readout laser (in our case 635 nm) directed at the backside of the cantilever. The application of the drive laser induces localized heating within the cantilever. Due to the difference in the thermal expansion coefficient between the cantilever base and coating material, this will cause a displacement of the AFM tip⁴²

An example of successful commercialization of photothermal actuation is blueDrive.⁴³ The name stems from the fact that a blue laser is focused at the base of the cantilever; its power is modulated at the chosen frequency to oscillate exclusively the cantilever.⁴⁴ The method has been used successfully to image high-resolution DNA and video rate imaging. It is also claimed

to observe mechanical properties more accurately than other resonant modes due to its clear resonance peak⁴³

1.2.3 Off-Resonance Tapping Modes

One major disadvantage of resonant dynamic modes is the lack of direct control over the tip-sample interaction forces. For most delicate biological samples, off-resonance tapping modes (Figure 1.2c) are preferred, since the force setpoint can be directly defined. In off-resonance modes, the cantilever or sample is actuated in a sinusoidal motion. When the cantilever tip is far away from the surface, the cantilever deflection remains close to zero during this motion. When the cantilever is close to the surface, the tip touches the surface close to the maximum point of the oscillation (see Figure 1.4). The cantilever is then deflected by the surface, which can be detected by the OBD. The maximum deflection value of the cantilever is then used as the process variable for the feedback loop. In more advanced off resonance modes, a background signal is recorded just above the surface to capture all the parasitic forces that can mask the true tip-sample forces. This background signal is then subtracted from the actual deflection signal before the peak interaction force is extracted.⁴⁵ Since the interactions with the surface are in essence a series of quasi-static force curves, inertial and resonance effects of the cantilever do not play a major role in the measurement of the tip-sample force. We therefore have more direct control over the tip-sample forces. In ORT modes that use a piezo to oscillate the cantilever or sample, the limitation in speed is due to the resonance of the piezo.

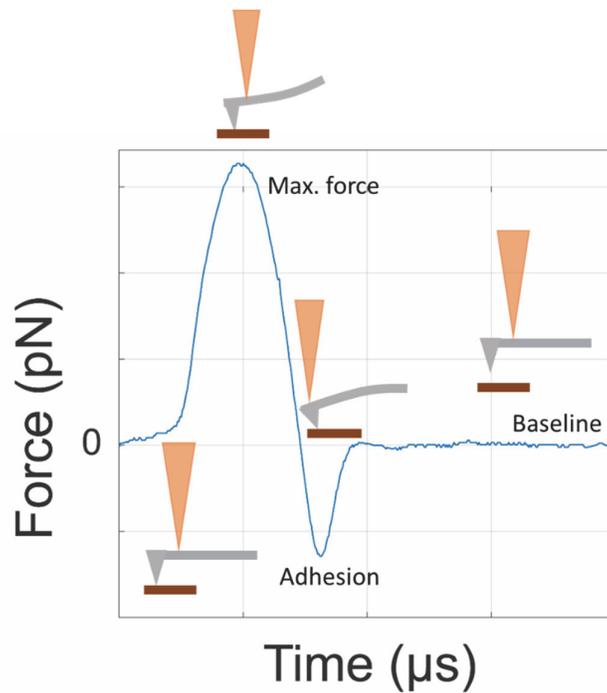


Figure 1.4 (ORT interaction curve): The approach and withdrawal of the AFM tip in a single tapping cycle in off-resonance tapping modes of AFM. The tip trajectory is shown according to the force vs time curve. The cantilever approaches the surface, bending slightly upwards when reaching contact. This causes the angle of the reflected laser to change. During the subsequent retraction, the cantilever adheres slightly to the surface (depending on the properties of the material), therefore bending slightly towards the surface and once again changing the angle of the reflected laser.

The earliest implementations of off-resonance tapping modes were pulsed force mode²² and Jumping mode⁴⁶. Pulsed force mode operates as any standard off-resonance mode, and was used for characterization of, for example, photopatterned polymer films⁴⁷. Jumping mode was introduced soon after pulsed force⁴⁸. It was used, for example, to image biomolecules in the repulsive electrical double layer.⁴⁸

PeakForce⁴⁹ mode further improved the force resolution, and is also used for quantitative nanomechanical mapping. The major advancement made in this mode was the possibility of background correction, allowing lower forces to be used, which can drastically improve the signal-to-noise (background) ratio and reduces the force needed to achieve proper tracking.⁵⁰ Other examples of off resonance modes include QI mode⁵¹ and HybriD mode⁵².

Photothermal Off-Resonance Tapping Mode

A shared disadvantage of most off-resonance modes is the fact that the excitation frequency is limited by the resonance of the scanner. Since the actuated mass is relatively large, the rate of force curves in most off-resonance tapping modes is a few kHz, reaching an order of magnitude higher for advanced designs⁵³. This limit was partially solved with the use of photothermal excitation of the cantilever (Figure 1.5a) in the photothermal off-resonance tapping mode (PORT). The intensity of the photothermal drive laser can be pulsed at up to several hundreds of kHz PORT rate.⁵⁴ If the cantilever is far from the surface, the cantilever tip performs a sinusoidal motion called the background motion due to the photothermal actuation (grey curve of Figure 1.5b).

If the cantilever is actuated closer to the surface, the cantilever will intermittently touch the surface, which results in a cantilever deflection curve similar to the orange curve in Figure 1.5b). As the intensity of the drive laser reduces, the cantilever is bent up away from the surface. However, adhesion keeps the tip attached to the surface for a while, which results in the orange curve crossing the gray curve (A). Once the cantilever bending force exceeds the

adhesion force, the cantilever detaches from the sample and snaps back to the gray curve. The abrupt snap-off excites the resonances of the cantilever, and the cantilever oscillates around the gray curve until the oscillation is damped (B). The overall cantilever deflection is a superposition of the deflection due to photothermal actuation and the deflection due to the tip-sample interaction. The tip-sample interaction curve can therefore be reconstructed by subtracting the background curve from the overall cantilever deflection curve (orange curve in Figure 1.5b).

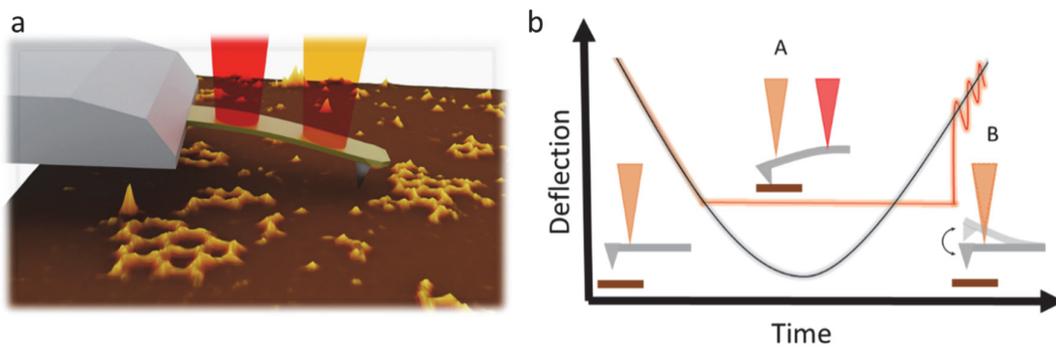


Figure 1.5 (PORT interaction): a) A close up render of an AFM cantilever bending with the effects of the secondary laser, with a b) graph showing the sinusoidal cantilever modulation (grey) and the tip-surface interaction (orange curve) in air.

1.3 HS-AFM

In its early days, AFM was considered a relatively slow imaging method, which was an issue when trying to image time sensitive bioprocesses. Increasing the speed, however, would reduce the image quality. In 1990, Quate et al. presented the effects of increasing scan rates in contact mode AFM at a conference. The first published mention of high-speed AFM was in 1991,

where a GaAs metal-semiconductor field-effect transistor was imaged at a 600 Hz line rate in constant height mode.⁵⁵

There are two major challenges in HS-AFM: the tip-sample interaction forces and the compromise between scan size and scan rate. Interaction forces made it difficult to achieve high-speed imaging on sensitive samples. This was partially solved with the introduction of tapping mode in fluid. In 1994, motion and enzymatic degradation of DNA was imaged at 8 Hz line rate.³³ A few years later, publications on short cantilevers for AFM emerged, but their availability was very limited.⁵⁶⁻⁵⁹ With increasing popularity of HS-AFM, however, they were eventually made more widely commercially available.⁶⁰ High-speed scanners were also an important component that lead towards achieving HS-AFM⁶¹⁻⁶⁵, and need have a good compromise between resonant frequency and scan range. Finally, a good control system (in terms of electronics, control algorithms and data acquisition)^{61,63,66,67} needs to keep up with the speed of the hardware. It is only with a combination of components that HS-AFM gained value, not only for increasing the speed of imaging for the purpose of saving time, but also to achieve the temporal resolution required to image biological processes. By 2000, for example, Hansma imaged GroES to GroEL interaction at 10.2 Hz.⁶⁸ In 2001, Ando et al. achieved frame rates of 12.5 fps (tip speed 0.6 mm/s) to image myosin V on mica.⁶¹

Not only are tip-sample interaction forces an issue, but they are also difficult to measure precisely in high-speed imaging. If the cantilever and sample properties are precisely defined, the forces of tapping mode AFM can be defined through models obtained from linking resonance frequency as a function of amplitude.⁶⁹ Another common approach for doing so, for example, is imaging a sample with known binding strength.^{42,70} By combining these two

approaches, however, the forces can be quite accurately defined, but are unfortunately still quite high (several nN) in tapping mode.⁷¹ Tapping mode is therefore not ideal for imaging more delicate samples, particularly for a longer duration.

The above-described PORT mode can, to some extent, provide a solution to the problem of compromise between imaging speed and control over tip-sample interaction forces. This mode has been successfully used to image in-vitro processes such as SAS6 ring dynamics^{42,72} and live cells⁷³. The dynamic force during imaging is easier to define; while it is shown to surpass the force set-point, reaching close to 1 nN even for low setpoints, this is still lower than in most other current imaging methods.⁴² For the setup used in our group, shown in Figure 1.6, work has already been done in improving the speed of the electronic components, the customizing the scanner and small-lever head, and continues to be done for further improving the imaging speed through development of ultra-short cantilevers.

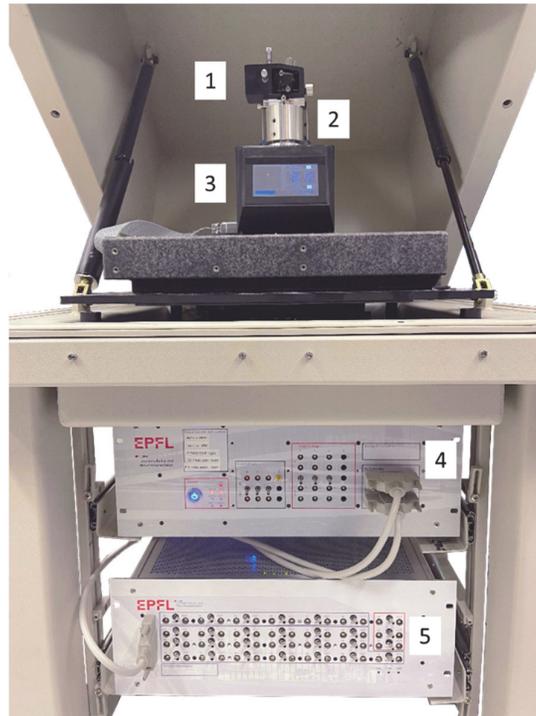


Figure 1.6 (HS-AFM setup): The High-Speed AFM setup used in our group, including 1. The small-lever head 2. The custom built scanner and the sample stage 4. The base 5. The high-voltage amplifier and 6. The controller.

1.4 Use of AFM to measure mechanical properties

In addition to imaging, AFM can also be used to measure the mechanical properties of biological samples, such as stiffness, elasticity, and adhesion^{74–82}. AFM gauges the mechanical attributes of a surface through either tracking the tip-sample interaction force versus distance or assessing the impact of this interaction force on specific parameters of the tip's oscillation.⁸³

Earlier examples of AFM use for measuring mechanical properties of bio samples was done in contact mode at constant force to give information about the compressibility (for example, on

gap junction membranes⁸⁴, DNA⁸⁵ and cells⁸⁶). In tapping mode, the phase image can also be used to observe a difference in elasticity within a sample.⁸⁷

1.4.1 Dynamic modes

Multifrequency AFM makes use of additional frequencies to gain information about the sample⁸⁸. Excitation frequencies are adjusted to align with two flexural eigenmodes of the cantilever (typically the first and second). The imaging of surface topography relies on the output signal from the first mode (either amplitude or frequency shift), while changes in mechanical properties are measured using the output signals from the other eigenmode.

Intermodulation AFM⁸⁹, dual frequency resonance tracking (DFRT)⁹⁰, HarmoniX⁹⁰ and bimodal⁹¹ AFM are a few examples belonging to this approach. In bimodal AFM, the amplitude of the first mode is used for topography imaging while the signal from the second mode is used for obtaining different mechanical or electromagnetic properties.^{92,93} Bimodal AFM is more sensitive to compositional changes than amplitude modulation AFM, and has been used to measure the properties of isolated antibodies in air and liquid. In adding additional harmonics, more properties can be extracted⁹⁴. There are a few reasons, however, why these methods were originally not as popular in measuring mechanical properties. The tip-sample forces are quite high, and the amplitude in other harmonics is much lower.⁹⁵ Solutions to these issues include adapting the cantilever design or reducing the noise.^{96,97}

1.4.2 Quasi-static

Force volume maps are less complex and provide accurate data in individual force curves⁹⁸. The method was first published in 1994.⁹⁹ By applying a controlled force to the sample and measuring the resulting deformation, AFM can provide insights into the underlying physical and mechanical properties of biological materials at the nanoscale, as shown in Figure 1.7.

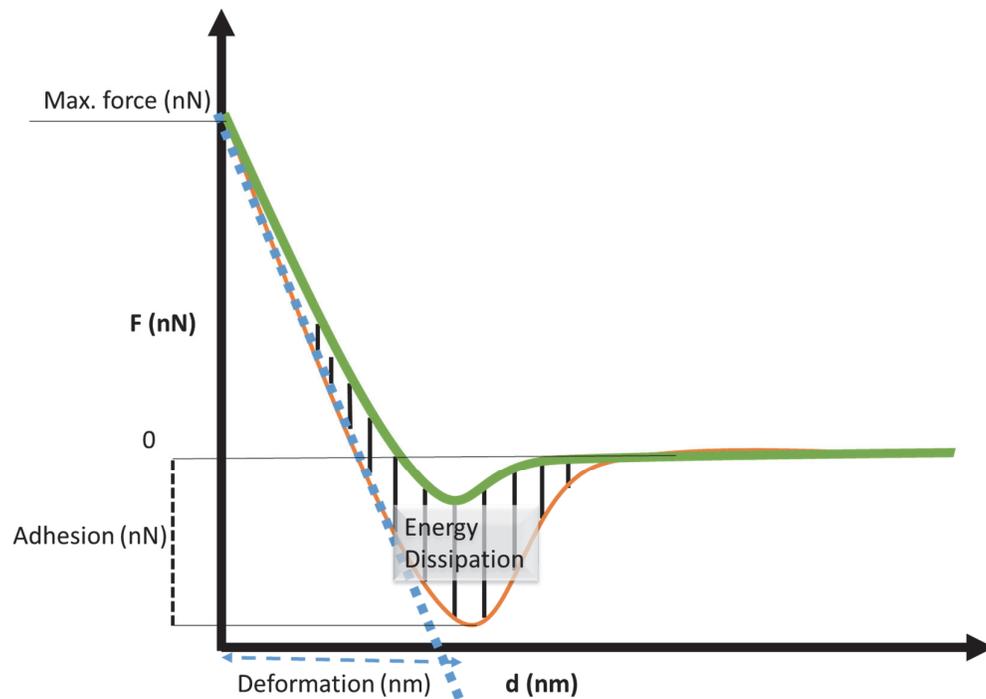


Figure 1.7 (Force separation curve): Force separation curve with scheme of evaluation of mechanical properties that can be extracted from a force-distance curve obtained by AFM. F is the force of the cantilever on the sample and d is the vertical displacement. The approach is represented in green and the retract in orange. The area between the two curves represents the energy dissipation, the depth of the retract curve below 0 gives the adhesion, the distance to the most negative point of the curve gives the distance of deformation.

The main issue with standard force-volume mapping is that it is relatively slow.¹⁰⁰ Fast force mapping¹⁰¹ and PeakForce Tapping^{TM102} provide a solution to this. Fast force mapping, for example, can provide accurate data at around 100 times faster rate ($\sim 100 \mu\text{m/s}$ instead of $\sim 1 \mu\text{m/s}$).¹⁰¹

1.4.3 Off-Resonance Modes

The previously described off-resonance modes such as Pulsed Force Mode¹⁰³, PeakForce Tapping^{TM102}, HybriD¹⁰⁴, QI^{TM105}, PinPoint^{TM106} and others further increased this mapping speed. However, the increased speed comes at the cost of increased noise, as well as a lack of consensus on modeling and difficulty in calibration. Of these off-resonance modes, PeakForce QNM¹⁰² is most commonly used. In these modes, the ratio between the probe spring constant and the elasticity and adhesion of the sample has an important influence on the measurements. The probe should be of similar stiffness to the sample, which is difficult in case the sample has large variations in mechanical properties across its surface. The applied force and the shape of the tip also play important roles in the measurements.¹⁰⁷

The calculation of force as a function of indentation relies heavily on the tip geometry. The selection of tip geometry depends on the desired resolution and the fragility of the sample. Spherical tips give a more global value of stiffness. Conical tips give more local stiffness measurements but are not recommended for samples that are likely to be penetrated. The simplified equations that link the measured force and indentation to the materials properties require the assumption of the tips to be an exact shape¹⁰⁸:

For a conical tip (shown in Figure 1.8a)

$$F = \frac{2}{\pi} \frac{E}{1 - \nu^2} (\tan\theta) h^2$$

Eq. 1-1

For a paraboloid tip (shown in Figure 1.8b)

$$F = \frac{4}{3} \frac{E}{1 - \nu^2} \sqrt{R} h^{3/2}$$

Eq. 1-2

F is the applied force, h is the indentation depth, θ is the cone half opening angle, E is the Young's modulus, ν is the Poisson's ratio and R is the radius of the curvature of the AFM probing tip. The diagrams showing a visual representation of this are shown in Figure 1.8.

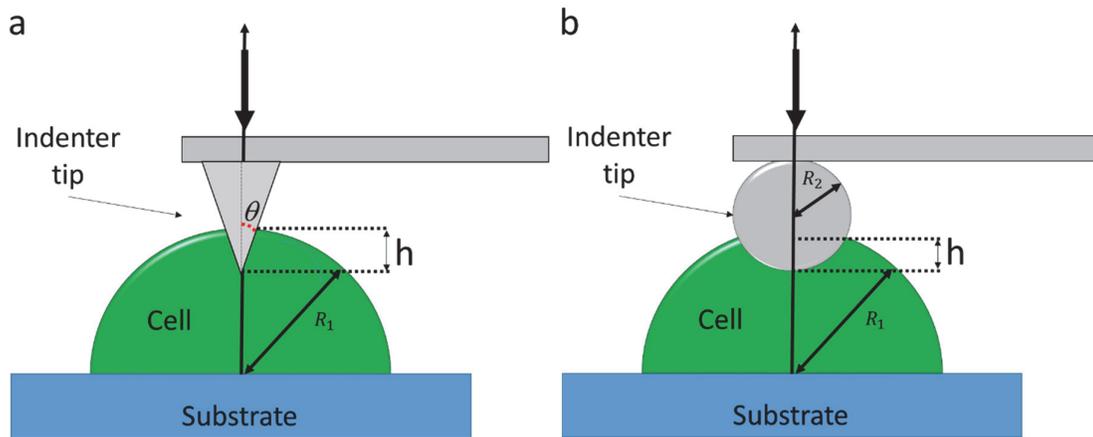


Figure 1.8 (AFM indentation): Diagram of AFM indentation experiment. On the left, a conical probe is used. In the center panel, a spherical probe is used. θ is the conical tip half angle. R_2 is the radius of the spherical AFM probe, R_1 is the approximate radius of the biostructure, and d is the deformation distance.

The reliability of AFM in the study of mechanical properties is uncertain but is particularly useful in giving a relative comparison between samples, as is presented in Chapter 4.

1.5 Use of AFM for imaging DNA

AFM has been used for imaging DNA for over 30 years. The first images were taken in air^{109–111}, but, sample humidity was kept at 30-60% to prevent solvation¹¹² or sample detachment. Imaging in fluid was shown and became the standard shortly after.¹¹³ It is of high importance

to use the correct liquid/buffer for the imaging purpose. Eventually, it was also possible to visualize individual functional groups within the DNA, in addition to the double helix^{114 115}. The structure of individual elongated molecules was observed without the need of crystallization, and it was possible to resolve intramolecular variations in groove depth, which is not achievable with methods that depend on ensemble averaging; it is also possible to image different structural conformations of the DNA double helix.¹¹⁶

1.5.1 Surface preparation

In the earliest cases of imaging DNA with AFM, mica was soaked in magnesium acetate for stronger binding to the phosphate groups of the DNA, a method which was earlier applied for preparation of EM samples¹¹⁷ (the Mg^{2+} increase the affinity of the negatively charged mica surface). Later, metal cations were used (Co^{2+} , La^{3+} , and Zr^{4+}) to prevent circular DNA from coiling during the drying process when imaging in air¹¹⁸. Eventually, it was shown that surface preparation is unnecessary, and it is sufficient if the cations are present in the buffer.^{119–122} It is also possible to use carbon coated mica¹²³ or a cationic lipid bilayer¹²⁴ for improved resolution.

Besides the cation-assisted method, chemical functionalization was also sometimes used, such as APTES^{125–127} or 1-(3-aminopropyl)silatrane (APS)^{128–131}, particularly for functionalization of glass or silica based surfaces.

1.5.2 DNA Nanotechnology

By controlling its molecular interactions and information, DNA can also be used as a building material for assembling nanostructures, such as DNA origami and tile-based assembly.¹³² This was originally developed as an algorithm by Seeman¹³³ In summary, he discovered that branched junctions are connectable through base-pairing of single-stranded overhangs (sticky ends) into a crystalline material. He discussed the possibility of designing oligonucleotide sequences that form immobile nucleic acid junctions instead of the usual linear duplexes, by removing sequence junctions. These so-called sticky-end ligation techniques allow linking of junctions and networks that can grow large enough for analysis; incorporating recognition sequences can add the possibility of protein binding in the structures. The first immobile nucleic acid junction constructed from oligonucleotides in practice was created in 1983.¹³⁴ This was an important step, since naturally-occurring junctions in DNA are inherently unstable, and it was difficult to investigate the forms structurally at high resolution in short-chain molecules until then. The tetrameric junction complex was observed with UV optical absorbance experiments.¹³⁴

Eventually, it was possible to observe self-assembly of hexagonal 2D arrays of DNA. The designed three-point star motifs can organize into hexagonal 2D arrays. These lattices can be as large as 1 mm.¹³⁵ This type of assembly is possible due to pi-pi (π - π) interactions.¹³⁶ These are noncovalent interactions between nucleobases in DNA, and help stabilize the structure of DNA duplexes; around 60% aromatic side chains are estimated to take part in π - π stacking.^{137,138} In 1991, the first closed polyhedral object (cube) made from DNA was created.¹³⁹ Since then, a variety of 3D structures self-assembled from DNA bricks were made.^{140,141}

1.5.3 Dynamic Imaging

Initially, dynamic imaging of DNA with AFM was done by creating time lapses rather than with high-speed imaging.¹⁴² However, these studies were only able to show slow, minute-level timescale processes, which is insufficient for the detection of most dynamics. After the development of HS-AFM described earlier, it was soon possible to image in the sub-second timescale, for example of site-specific DNA binding proteins,¹⁴³ which eventually progressed towards the possibility of imaging more complex interactions with improved speed and resolution, such as dynamic protein conformational changes for multistep DNA-binding mechanisms.¹⁴⁴

HS-AFM is now extensively used for imaging self-assembly of DNA patterns. For example, it is possible to observe the effects of Mg^{2+} and Na^+ ion concentration ratios on the assembly process and stability using HS-AFM.¹⁴⁵ It is also possible to observe the dynamics of photoresponsive DNA origami nanostructures; UV irradiation is used to reversibly disassemble hexagonal dimers into monomers, which then reassembly into their full hexagonal origami structure with visible light irradiation.¹⁴⁶ As further work is being done towards increasing the scan range of high-speed imaging,¹⁴⁷ more complex structures may eventually be observed, such as the multicomponent (origami) structure formation that is currently observed at standard imaging rates.¹⁴⁸

1.6 Use of AFM in Self-Assembly

1.6.1 Nucleation and Growth Models

The study of nucleation and crystallization pathways continues to draw interest for its role in biological and technical applications.¹⁴⁹ Solid materials all form via nucleation (shown in Figure 1.9), where a stably formed nucleus determines the location and nucleus size, and the subsequent growth through directional interaction defines the size, shape and aggregation.¹⁵⁰ Unlike the strong, directional bonding found in covalent interactions¹⁵¹, supramolecular crystals are more flexible and dynamic in their formation process^{152,153}. At high concentrations (supersaturations), the crystals may already form in the bulk solution, otherwise they only begin the assembly process on the surface.¹⁵⁴ The speed of growth is also dependent on surface energy of the crystals, where lower values lead to a faster growth rate.^{154,155} Other effects on the growth process include temperature and pressure, pH, concentration, diffusion, as well as others.^{156–158}

Primary nucleation is used to describe an aggregate forming from monomers, and can be divided into homogenous nucleation (forming in bulk solution) and heterogenous nucleation (forming on the surface of another substrate or the air-water interface). Secondary nucleation is used to describe monomers starting the nucleation process on a surface of an already existing aggregate. Secondary nucleation is what leads to the formation of 3D protein crystals and molecules^{159–161}

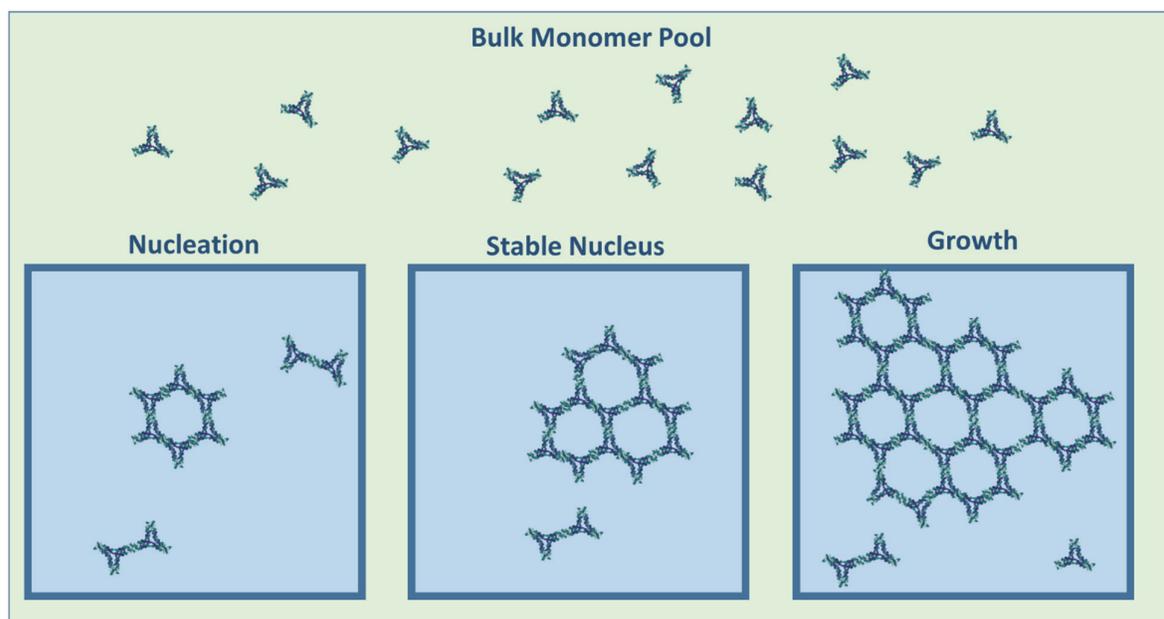


Figure 1.9 (Nucleation Pathway): Nucleation pathway in the example of DNA 3PS, showing the formation of a (hexagonal) nucleus, stabilization of the nucleus, and growth of the patch.

There are several theories and models used to describe the nucleation process. Classical nucleation theory (CNT) provides a good framework for explaining solid nucleation. However, the spherical assumption of CNT may not be applicable when the nuclei contain fewer than 100 molecules. There are other assumptions made in CNT that may not always be applicable; for example, that the nucleus has the same density, structure and composition of the stable phase, that the nucleus is spherical, that the interface with the solution has a clear boundary, and that the vapor-liquid interface is always planar. This is mostly applicable for large clusters.¹⁶² Non-classical nucleation theory take into account oriented attachment and intermediate stages.¹⁵⁰ The balanced nucleation-growth process model, for example, quantifies

the rates of nucleation and maximum growth, as well as supersaturation, in relation to nucleation efficiency. This is useful in industrial processes where final crystal size needs to be controlled.¹⁶³ The validity of nucleation theories can be tested with Monte Carlo simulations, which can show the nucleation rate, the spreading rate and the size of the clusters.¹⁶⁴

1.6.2 Use of AFM for Biological Self-Assembly

In the early stages of AFM, bioimaging was not as common due to the drawbacks of imaging in contact mode. To some extent, it was possible using low spring constant cantilevers.²⁷⁻²⁹ Therefore, even in the early stages of AFM, contact mode allowed for imaging of biosamples in-vitro at high resolution.^{30,31}, or provide some information on biomolecular dynamics, through time lapse imaging.³²⁻³⁴ The benefit of AFM in observing self-assembly is the possibility to directly observe the structure and dynamics of, for example, protein self-assembly or biomineralization.¹⁶⁵ One of the earliest biological self-assemblies observed by AFM were of collagen, at first by time lapse imaging,^{166,167} by now, it is possible to image this process at high speed, and even include nanomechanical mapping.¹⁶⁸ Actin was also originally observed with time-lapse AFM,¹⁶⁹ but with the use of HS-AFM one can now visualize the polymerization at 8 fps.¹⁷⁰ There have also been attempts to image dynamics of microtubules, but thus far it was only possible to observe the de-polymerization rather than the assembly.¹⁷¹ This is mainly due to the issues in tip-sample interaction forces and their effects on the sample, as well as the quality of sample preparation. Some effects of imaging parameters on the sample behavior in HS-AFM for our setup are further explored in Chapter 2 of this thesis. In custom design of multivalent interaction, usually with the help of models and simulations^{172,173} affinity and valence are of particular importance, while structural contributions are often not taken into

account. As the functionality of current AFM systems continues to be improved, and we branch out into advanced and combined AFM modes, it will become increasingly possible to image more complex assembly systems, in increasingly complex environments (e.g. live cells).

Contribution of the thesis

Atomic force microscopy is a valuable tool for bio-imaging but is often not customized or used to its full potential when relying on commercial setups. Our group uses home-built AFM components that allow for adaptations and optimizations to be more compatible for the sample and measured property. The thesis will be composed of three research papers, one in revision, one accepted and one published. My contribution to each of the papers is stated at the beginning of each chapter.

The first chapter of this dissertation focuses on the optimization of a setup of custom-built high speed AFM components for applications in dynamic biomolecular imaging, while determining the limits tracking the effects of various imaging parameters specific to the setup on imaging quality.

In the second chapter, this same setup is applied for investigation of self-assembly patterns of various samples, with a focus on DNA 3-point stars for better focus on details. This enables us to identify self-correction mechanisms based on structural flexibility and binding strength that will eventually be useful in more complex samples.

The third chapter investigates the use of AFM in determining mechanical properties of soft biosamples, in this case a soft membrane mimicking lung tissue. A similar method for

measuring the Young's Modulus was then used on cells for checking the effects of cholesterol depletion on cell stiffness¹⁷⁴, which lead to the idea of the fourth chapter.

The fourth chapter shows the current progress in imaging clathrin dynamics on unroofed cells depleted of cholesterol, showing the current issues in imaging bio-sample dynamics with AFM.

The thesis ends with a discussion on the future opportunities using the methods discussed.

2. High-Speed AFM Imaging Of DNA Three-Point-Star Motif Self Assembly Using Photothermal Off-Resonance Tapping

This chapter is a copy of the manuscript accepted by the peer-reviewed Journal of Visualized Experiments. We investigate the effects of changing various parameters of the PORT excitation on imaging of DNA 3 point stars. My contribution includes establishing the precise imaging protocol, identifying the limitations in various parameters, collecting, analyzing the imaging data and writing the manuscript.

Cencen, V., Ghadiani, B., Andany, S. H., Kangül, M., Tekin, C., Penedo, M., Bastings, M., Fantner, G. E. High-Speed Atomic Force Microscopy Imaging of DNA Three-Point-Star Motif Self Assembly Using Photothermal Off-Resonance Tapping. *J. Vis. Exp.* (Pending Publication), e66470, In-press (2024).

Summary:

Here, we show the imaging protocol for observing biomolecular interactions with photothermal off-resonance tapping (PORT), where we optimized imaging parameters, identified system limits, and investigated potential improvements in imaging three-point-star DNA motif assembly.

Abstract:

High-speed atomic force microscopy (HS-AFM) is a popular molecular imaging technique for visualizing single-molecule biological processes in real-time due to its ability to image under physiological conditions in liquid environments. The photothermal off-resonance tapping (PORT) mode uses a drive laser to oscillate the cantilever in a controlled manner. This direct cantilever actuation is effective in the MHz range. Combined with operating the feedback loop on the time domain force curve rather than the resonant amplitude, PORT enables high-speed imaging at up to ten frames per second with direct control over tip-sample forces. PORT has been shown to enable imaging of delicate assembly dynamics and precise monitoring of patterns formed by biomolecules. Thus far, the technique has been used for a variety of dynamic *in vitro* studies, including the DNA 3-point-star motif assembly patterns shown in this work. Through a series of experiments, this protocol systematically identifies the optimal imaging parameter settings and ultimate limits of the HS-PORT AFM imaging system and how they affect biomolecular assembly processes. Additionally, it investigates potential undesired thermal effects induced by the drive laser on the sample and surrounding liquid, particularly when the scanning is limited to small areas. These findings provide valuable insights that will drive the advancement of PORT mode's application in studying complex biological systems.

Introduction:

High-speed atomic force microscopy (HS-AFM) is a rapidly growing imaging technique¹⁷⁵⁻¹⁷⁸. It operates at speeds that allow researchers to visualize biomolecular interactions in real

time^{170,179–182}. Photothermal off-resonance tapping (PORT) is an off-resonance imaging mode similar to peak force tapping^{183,184}, pulsed force mode^{22,103}, or jumping mode⁴⁶. However, rather than vertically oscillating the scanner, PORT vertically oscillates only the cantilever through an excitation laser focused on the cantilever (usually close to the clamping point). The cantilever deforms due to the bimorph effect: a power-modulated excitation laser periodically heats the coated cantilever, which bends due to the different thermal expansion coefficients of the cantilever and the coating materials³⁹. Cantilever and sample heating can be minimized by using a drive laser that is periodically switched off and back on during each oscillation cycle, rather than using a full sinusoidal drive¹⁷⁹.

DNA has been used to form biologically relevant, structurally interesting, and biochemically useful motifs for a number of years^{135,185–188}. In addition, DNA structures have been proven ideally suited to characterize AFM imaging quality¹⁸⁹ and to assess the tip-effect of high speed AFM⁷⁰. Blunt-end DNA three-point-stars (3PS) became practical as a programmable model system for investigating the supramolecular organization of similarly structured molecules in otherwise complex biological systems¹³⁵. Previously, the self-assembly of lattices formed by blunt-ended trimeric DNA monomers was tracked via HS-AFM¹⁴⁷. Eventually, these organize into large networks with hexagonal order. Here, the self-assembly of DNA 3-point stars¹³⁵ is imaged with the PORT technique at scanning speeds fast enough to track the self-assembly and its correction mechanisms¹⁹⁰ while assuring minimal disruption of the process or sample damage. As with any HS-AFM mode, there is a trade-off between achievable imaging quality, imaging speed, and the unwanted disturbance of the sample. By choosing the right

compromise, one can better understand the self-organization patterns of supramolecular assemblies. This protocol will, therefore, use a similar setup with DNA 3PS as a model system to optimize the parameters specific to PORT. This will allow operation at fast imaging speeds at large enough scan sizes while minimizing sample damage.

Protocol:

1. Sample and buffers

NOTE: The DNA tile used in this study is the 3-point-star motif developed at the Mao laboratory at Purdue University^{19,25}. All oligonucleotides used in this study were purchased from Integrated DNA Technologies, Inc. Gather the necessary materials and reagents.

1.1. Mix the single-stranded DNAs (ssDNAs) at a 1:3:3 molar ratio (S1 0.6 μM , 1.8 μM for S2, and 1.8 μM for S3) in the annealing buffer (5 mM TRIS, 1 mM EDTA, and 10 mM MgAc_2). The final concentration of the DNA motif must be 0.6 μM (49 ng/ μL with the molecular weight of 3PS being 82020.3 g/mol).

1.2. Place the DNA solution in a heat-resistant container and heat it to 80 °C. Slowly cool the DNA solution from 80 °C to 20 °C over a period of 4 h. This annealing process helps the ssDNA oligonucleotides to form the desired double-stranded DNA motif.

1.3. For purification, load the annealed DNA solution onto a 3% agarose gel to remove the excess ssDNAs and any unwanted side product. Run the 3% gel at 60 V for ca. 2.5 h in a running buffer containing 0.5x Tris-Borate-EDTA (TBE) and 10 mM $\text{Mg}(\text{CH}_3\text{COO})_2$.

- 1.4. Identify and locate the band on the gel that contains the DNA motif. Ensure that the band has migrated to a specific position based on its size.
- 1.5. Excise the band containing the DNA motif from the gel carefully. Extract the DNA motif from the excised gel fragment by placing it in a gel extraction spin column and centrifuging at 3,000 x g and 4 °C for 10 min.
- 1.6. Replace the buffer in the extracted DNA motif with the annealing buffer using a centrifugal concentrator. Centrifuge at 3000 x g at room temperature (or lower) until the concentrated solution is less than 100 µL. Then, add 300 µL of annealing buffer and repeat this step twice to ensure the buffer is replaced.
- 1.7. Dilute the DNA motif to 6 nM for imaging purposes. Use a spectrophotometer or other appropriate methods to accurately determine and adjust the concentration. The DNA motif is now ready for imaging.

NOTE: All buffers in the protocol are of pH 8.0. The sequence information for the three respective bands is as follows:

S1:

AGGCACCATCGTAGGTTTCTTGCCAGGCACCATCGTAGGTTTCTTGCCAGGCA
CCATCGTAGGTTTCTTGCC

S2: ACTATGCAACCTGCCTGGCAAGCCTACGATGGACACGGTAACG

S3: CGTTACCGTGTGGTTGCATAGT

2. Cantilever tip growth

2.1. Cantilever mounting on the SEM cantilever holder: Ensure that cantilevers are clean and free from any contaminants. Mount the cantilevers onto a suitable holder compatible with the SEM system. The custom-built cantilever holder design can be shared upon request.

2.2. Gas injection: Heat up the precursor gas (e.g., phenanthrene $C_{14}H_{10}$ precursor for amorphous carbon tips) to be used on the gas injection system to grow the new tip. As soon as the vacuum is below 10^{-5} mbar, purge the gas injection line 10 times for 2 s to be sure no undesired remnant air is in the nozzle line (that must be done with the valve to the gun chamber closed).

2.3. Tip position adjustment: Use scanning electron microscopy (SEM) to locate the end of the cantilever. Tilt the cantilever holder to an angle (e.g., 11° in this case) equivalent to the one the cantilever will present when placed on the AFM cantilever holder with respect to the surface so the grown tip will be perpendicular to the surface while imaging. Adjust the position and focus of the SEM to obtain a clear view of the cantilever's tip, where a sharp carbon nano-tip will be grown.

2.4. Focused electron beam-induced deposition (FEBID):

Set the deposition parameters on the selected software (in this case, SmartFIB), such as beam current (I) and acceleration voltage (V), working distance (WD), magnification, exposed shape, dose/deposition time, and dwell time. The following parameters were used to grow amorphous carbon tips, which present good mechanical properties for AFM imaging, leading to lengths around 130 nm and radii in the range of 2–4 nm:

Select spot/dot as exposed shape

WD = 5 mm

I = 78 pA, and V = 5 kV

Dwell time = 1 μ s

Dose = 0.05 nC, and deposition time = 0.64 s

Magnification = 20000x

2.5. Begin the deposition process to grow the tip by irradiating the electron beam in a spot onto the cantilever tip while simultaneously injecting the precursor gas, closing the gas when the deposition is done. In this case, the SmartFIB software performs this automatically after setting up the recipe mentioned above.

2.6. Post-growth analysis: Perform post-growth SEM imaging to examine the newly grown tip and ensure its quality and characteristics (tip radius and length). Wait 1–2 min after tip growth to be sure all the precursor gas is pumped out to avoid re-deposition during the SEM imaging. Remove the sample holder from the SEM chamber.

2.7. Cantilever recycling: In case the SEM system also has a combined focused ion beam (FIB) installed, remove a damaged or dirty previously grown tip by milling it with the FIB system using low FIB currents (e.g., 1 pA, to avoid cantilever damage). Perform the tip removal by milling in a cross-section form, from tip end to base, to avoid tip collapse. This will let re-growing a new one.

3. HS-AFM hardware

3.1. The imaging setup is composed of the custom-built PORT head^{179,191} (Figure 2.1A), high-speed scanner¹⁹¹ with a sample disc with mica on top, compatible controller¹⁹², high voltage amplifier with the high bandwidth required for high-speed imaging, AFM base, and PC with the required software to control the before mentioned equipment¹⁹².

NOTE: In this case, these are open-source components for which plans can be obtained from the Laboratory for Bio- and Nano- Instrumentation at EPFL^{192,193}. It is also possible to attend workshops on how to build the PORT head and controller¹⁹⁴, as well as to download and use the LabView based software.

3.2. Carefully place an ultra-short cantilever (e.g., AC10DS or equivalent) under the spring clip on the cantilever holder using tweezers. Assure that the cantilever chip is fixed and stable.

3.3. Add 50 μL of liquid using a syringe through the left fluid access port, as demonstrated in Figure 2.1B. With the excitation laser still off, align the read-out laser on the cantilever using the three dedicated knobs on the AFM head shown in Figure 2.1A. Do this by observing the shadow of the cantilever on a white paper while maximizing the sum (shadow method). Then, center the laser spot on the photodiode using the two dedicated knobs.

3.4. Switch on and align the drive laser by checking the Excitation Enable box in Excitation VI, so it actuates and oscillates the cantilever. Show the cantilever excitation signal and the cantilever deflection signal on a connected oscilloscope. If the deflection oscillation is too low (or not existent) it might be that the drive laser is very far off from the cantilever. In that case, use the shadow method and turn off the deflection laser for

easier alignment. Maximize the oscillation amplitude using the drive laser adjustment knobs shown in Figure 2.1A.

3.5. To adjust the cantilever oscillation amplitude in PORT, input in the corresponding control of the software the peak-to-peak voltage sent to the laser diode control circuit (from now on, peak-to-peak AC input) in Excitation VI. To keep the laser diode in the conduction regime and, therefore, lasing, add a DC voltage to the laser diode control circuit (from now on, DC offset input), which is also done from a configuration box in Excitation VI. Both will also affect the laser power, which can be measured with a laser power meter and is used to tune the cantilever oscillation amplitude.

3.6. Determine the maximum photothermal excitation frequency that can be applied to the cantilever, which must be below the resonance frequency of the cantilever. Determine the resonance frequency by a thermal tune or a frequency sweep. The cantilevers used in this study (AC10DS), whose resonance frequency in liquids is around 400 kHz (1 MHz in air)¹⁷⁹, have a quasistatic bending region below 300 kHz¹⁷⁹. Thus, PORT frequencies below that limit (around 100–200 kHz) must be used.

3.7. Adjust the imaging parameters and settings for PORT rate and scan rate to the required values in the Excitation and Scan Vis respectively (the parameters used in this article are stated in the figure descriptions). Once the setup and imaging parameters are configured, perform the required imaging experiments to observe and track the molecular interactions.

NOTE: Since AC10DS cantilevers are no longer sold, an alternative such as Fastscan D or BioLever¹⁹⁵ may need to be used until an equivalent is available.

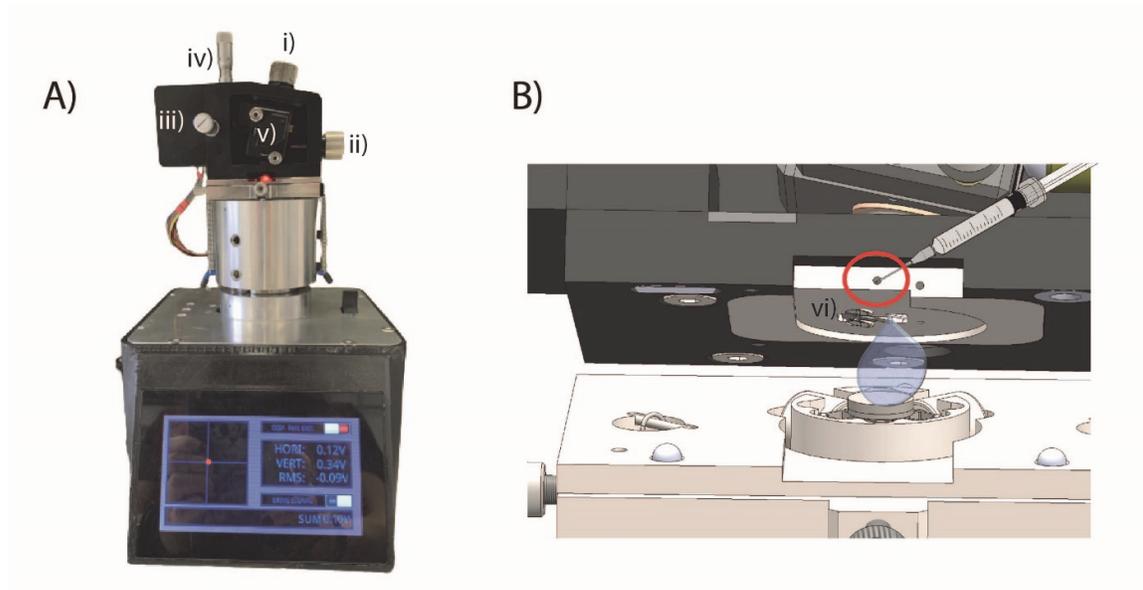


Figure 2.1 (The HS-AFM setup.): (A) The PORT head on the scanner and base of the AFM, showing the (i) knob for adjusting the read-out laser focus on the cantilever, (ii) knob for adjusting the read-out laser position on the cantilever, (iii) knob for adjusting the horizontal position of the laser on the photodiode, (iv) knob for adjusting the vertical position of the laser on the photodiode, and (v) knobs for adjusting the position of the photothermal drive laser on the cantilever. (B) A close-up of the cantilever in the cross-section view of the head with the sample stage, where (vi) is the spring clip holding the cantilever. The channel for liquid injection is marked in red.

4. Obtaining proper interaction curves

4.1. Initially, approach the sample surface in contact mode by clicking Start on the Z-controller VI set to Contact Mode.

4.2. In this mode, the AFM tip comes into direct contact with the sample. Once the surface is reached, perform a force versus distance curve in Ramp VI to obtain the cantilever deflection sensitivity calibration.

- 4.3. Also, estimate the cantilever spring constant, either from cantilever provider specifications (less accurately), obtained with an interferometer, or through a thermal tune-based calibration after the deflection sensitivity calibration. A precise cantilever calibration is essential for an accurate tip-sample force control.
- 4.4. After completely retracting the Z-piezo from the surface where the tip cannot reach the surface by clicking Up in the Z controller VI, switch to the PORT mode in the Z controller VI, and turn on the excitation laser in the Excitation VI checkbox. To begin, set the PORT mode to operate at the desired frequency in Excitation VI, which, in this experimental case, is 100 kHz, using an AC10DS cantilever.
- 4.5. Record the cantilever-free oscillation close but not touching the surface. Then, turn the Feedback in the Z controller ON in contact with the surface to record and click Correct to obtain the oscillation of the cantilever when the cantilever is intermittently in contact with the surface, both in nanometers. Subtract the free oscillation curve from the intermittent contact curve to obtain the true interaction curve, converting them to pN using the cantilever spring constant (in this case, 0.1 N/m).

5. HS-AFM imaging

- 5.1. Prepare a solution of $\text{Mg}(\text{CH}_3\text{COO})_2$ at a concentration of 10 mM. Using a Hamilton syringe, inject 50 μL of the prepared 10 mM $\text{Mg}(\text{CH}_3\text{COO})_2$ solution into the fluidic channel of the cantilever holder, creating a drop of liquid that englobes the cantilever.
- 5.2. Gradually approach the cantilever to the surface by clicking Start on the Z Controller VI. Once the surface is detected, turn the Feedback ON, and find the peak of the

- interaction curve in the ORT Force Curves VI. Find the lowest force setpoint that allows proper tracking (below 300 pN to avoid the damaging of fragile bio-samples).
- 5.3. Set the Scan Size in the Scan VI to 800 nm by 800 nm and the Line Rate to 100 Hz. Scan the surface by clicking the Frame (down) arrow in Scan VI to check the surface quality. If any contaminations are detected, address the issue by cleaning the surface, cantilever, and/or cantilever holder before proceeding.
 - 5.4. After scanning, retract the cantilever from the surface by clicking Withdraw in the Z controller VI. Remove the buffer solution from the hole in the cantilever holder with a Hamilton syringe to prevent dead volume issues.
 - 5.5. Prepare a diluted DNA 3PS solution from part 1 of the protocol. Inject 50 μ L of the diluted DNA 3PS solution into the dedicated channel of the cantilever holder.
 - 5.6. Start the imaging process by repeating steps 5.2–5.3, scanning an 800 nm by 800 nm area at a default line rate of 100 Hz (256 lines \times 256 pixels). After the initial scan, adjust the imaging size and speed in Scan VI to the specified values for further data acquisition.
 - 5.7. Keep the input force setpoint of the tip-sample interaction in the Z Controller VI Setpoint box at the lowest level required for proper tracking (below 300 pN) throughout the imaging process to minimize sample damaging/disturbance unless otherwise specified. Repeat this process for all the required sample areas.

6. Image processing

- 6.1. Set up the environment for running the customized Pygwy (Python for Gwyddion) batch processing code, ensuring that Python and all the necessary libraries. More information can be found on Gwyddion's website¹⁹⁶ are properly installed on the system. This ensures that the code runs smoothly and can access the required functionalities.
- 6.2. Open the customized Pygwy batch processing code (provided on request). This will provide access to the tools and functionalities needed for image processing and analysis.
- 6.3. Begin the image processing by performing horizontal median line correction on the images. This step aims to remove any irregularities or artifacts present in the scan lines, ensuring that subsequent processing steps are based on accurate data. After plane background removal, apply the line correction. Use scar removal to further enhance the images by eliminating any unwanted marks or imperfections caused by external factors. This step improves the overall visual appearance of the images.
- 6.4. Enhance the visibility and contrast of the images by adjusting the color height map. This ensures that features of interest are clearly visualized and stand out in the images.
- 6.5. Select the processed images that need to be combined into a video. Determine the desired frame rate for the video. In this case, set it to 7 frames per second (fps).
- 6.6. Calculate the duration of each frame. Use Fiji (ImageJ) to combine the processed images into a video. Ensure that the frame rate and frame duration are correctly set.

Representative results:

In this investigation, the dynamic assembly process of DNA 3-point-star motifs into stable islands was successfully observed utilizing the capabilities of the HS-PORT AFM. This technique allowed us to capture the assembly of these structures in real-time. In Figure 2.2A,B, we get a clear image scanning at 100 Hz and 200 Hz line rates, respectively, for 100 kHz PORT rate (800 nm by 800 nm scan size). This corresponds to 3.9 and 1.95 oscillation cycles per pixel, respectively. However, imaging at higher speeds without concurrent increases in the PORT rate that would allow above 1 oscillation cycle per pixel will drastically reduce the image quality, as can be seen in Figure 2.2C (0.78 of an oscillation cycle per pixel). The DNA 3 point star patches are poorly resolved and the polygons no longer discernible. The imaging speed is limited by the rate at which the cantilever probes the surface with appropriate tip-sample force control since the rate of topography change becomes too fast to track at the surface sampling rate.

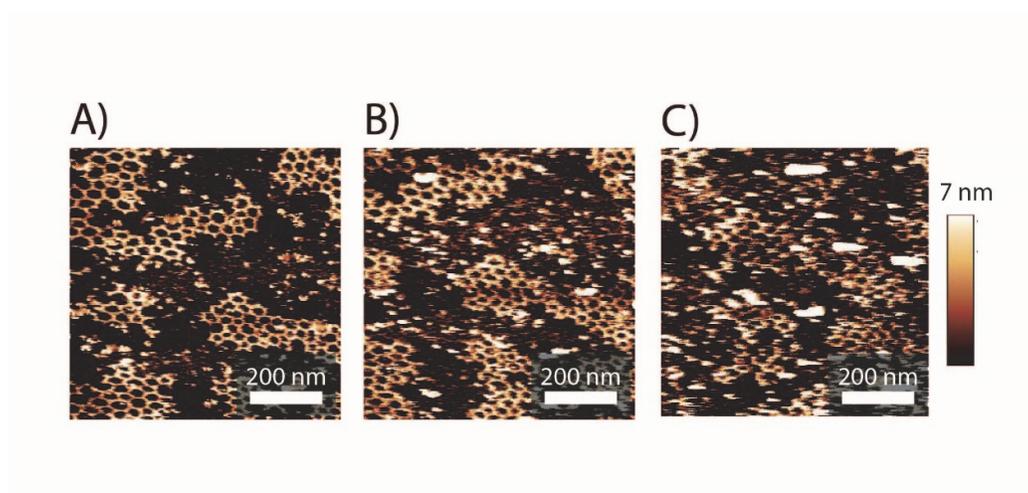


Figure 2.2 (DNA 3PS sample imaged with AC10 at 100 kHz PORT rate at different line rates): (A) 100 Hz (3.9 oscillation cycles per pixel), (B) 200 Hz (1.95 oscillation cycles per pixel), and (C) 500 Hz (0.78 oscillation cycles per pixel). The images were taken at setpoints of 350 pN or less. Scale bar 200 nm. A force curve to obtain deflection sensitivity was taken after imaging.

In addition to setting a high enough PORT rate, it is important that the PORT curves contain the information necessary to control the forces. Especially hydrodynamic drag and low detection bandwidth can obscure the applied force. Figure 2.3 displays the cantilever deflection at different distances from the sample's surface and excitation frequency rates using an average of 4096 curves to reduce the noise. The blue curves in Figure 2.3A (for 100 kHz PORT rate) and Figure 2.3D (for 500 Hz PORT rate) represent the cantilever motion when the cantilever is far from the surface and oscillates freely (not touching the surface during one oscillation cycle). The red curves show the cantilever deflection when the cantilever oscillates close to the surface and intermittently contacts the surface, probing the sample. To obtain the true interaction curve and, thus, the tip-sample interaction, we subtract the blue curve from the red curve to obtain Figure 2.3B,E, respectively. An example of a clear interaction curve required for non-destructive bio-sample imaging is depicted in Figure 2.3B. This configuration leads to the good imaging quality shown in Figure 2.3C, where the PORT rate is 100 kHz. As we increase the excitation frequency close to the cantilever resonance, at some point, the feedback control deteriorates, even when the cantilever displays enough amplitude oscillation to detach from the surface after raising the excitation laser power (Figure 2.3E). If the PORT frequency is too close to the cantilever resonance frequency, the cantilever resonance limits the time response of the cantilever dynamics. The cantilever bending, therefore no longer accurately

represents the tip-sample interaction, and the interaction curve we obtain is obscured. This leads to a degradation of the image quality through poor tracking, and sample damage as a result of poor control of the force setpoint, as displayed in Figure 2.3F.

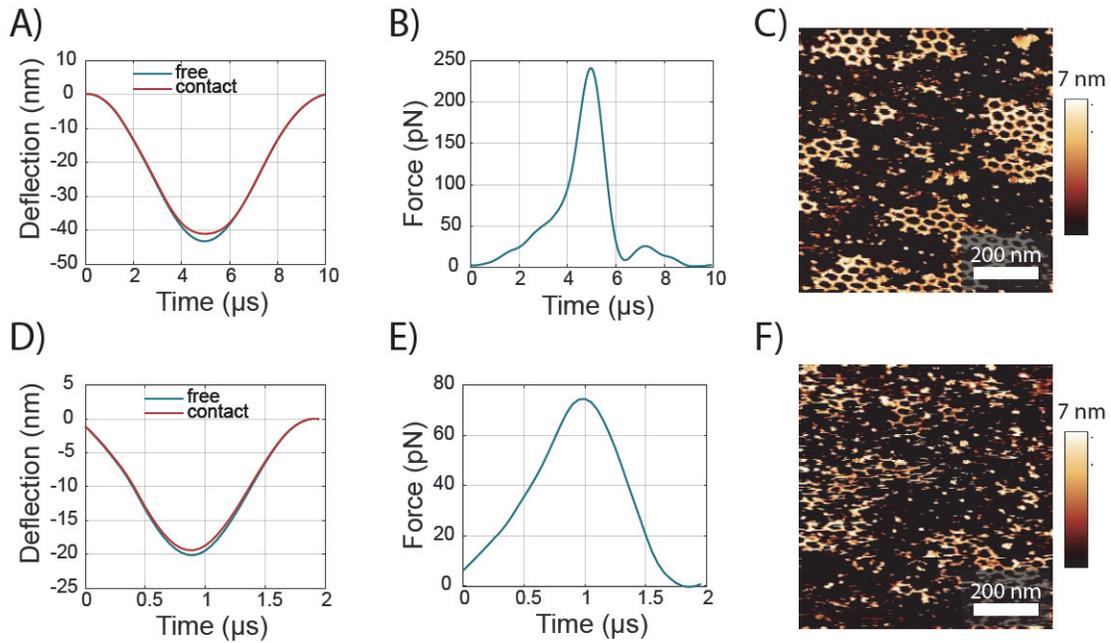


Figure 2.3 (Cantilever deflection, interaction curve, and image quality at 100 kHz and 500 kHz PORT rates): (A) Cantilever deflection (cantilever free oscillation close but not touching the surface in blue, and the oscillation of the cantilever when the cantilever is intermittently in contact with the surface in red), (B) interaction curve and (C) respective image quality for 100 kHz PORT rate. (D) Cantilever deflection (cantilever free oscillation close but not touching the surface in blue, and the oscillation of the cantilever when the cantilever is intermittently in contact to the surface in red), (E) interaction curve and (F) respective image quality for 500 kHz PORT rate. Images were taken at a line rate of 100 Hz. Scale bar 200 nm. A force curve to obtain deflection sensitivity was taken after imaging.

A compromised interaction curve at higher PORT frequencies might also happen due to the reduced actuation efficiency at higher frequencies¹⁹⁷, which is currently one of the limiting

factors of commercial high-speed AFM cantilevers. This decrease eventually reaches a threshold level in the roll-off, at which proper imaging is hindered: the oscillation amplitude might be insufficient to detach from the surface, and the tip is always in contact, damaging the sample structures. To counteract the decrease in amplitude caused at higher PORT rates, we explored an increase in laser power. We used a PORT head that can reach higher laser powers to better observe this effect. The laser power of the excitation laser, which we measured with a power meter, was divided into the DC and AC components. The total power is controlled by adjusting on the software the peak-to-peak voltage (peak-to-peak AC input) and the DC voltage (DC offset input) sent to the laser diode control circuit. Figure 2.4A displays the peak-to-peak cantilever oscillation amplitude resulting from an increased peak-to-peak AC input. As expected, the oscillation amplitude correlates well with the AC input value. It is important to note that these peak-to-peak amplitudes are higher than what is normally used in PORT imaging. When imaging fragile samples, the AC amplitude is on the order of 10–30 nm. Figure 2.4B displays the peak-to-peak cantilever oscillation amplitude for increased DC offset inputs. The peak-to-peak oscillation amplitude remains fairly constant over the DC offset voltage range. We attribute the small variations to nonlinearities in the detection. Figure 2.4C depicts the increase of the AC and DC laser power components resulting from the increasing peak-to-peak AC. Figure 2.4D depicts the increase of the AC and DC laser power components resulting from the increasing DC input offset.

The effects of increasing the peak-to-peak AC input and DC offset input were tested separately to determine the respective effects on total power and oscillation amplitude. An increase in

laser power causes the sample to be disrupted, likely through temperature increase, whereas an increase in oscillation amplitude will increase the impact force on the sample¹⁷⁹. Increasing exclusively the peak-to-peak AC input will have less impact on the total laser power increase, as shown in Figure 2.4C, and will predominantly increase the cantilever oscillation amplitude (and consequentially the impact force), as shown in Figure 2.4A. Increasing the DC offset input will have a greater effect on the increase of laser power output, as shown in Figure 2.4D, which heats the sample but will have a negligible effect on the deflection amplitude, as seen in Figure 2.4B. Imaging results are represented in Figure 2.4E,F. Figure 2.4E depicts DNA 3PS for the lowest peak-to-peak AC input (left image, circled in blue) and highest peak-to-peak AC input (right image, circled in red), which results in sample damage presumably through the higher forces. Figure 2.4F exhibits DNA 3PS for the lowest DC offset input (left image, circled in blue) and highest DC offset input (right image, circled in red), where structures are damaged.

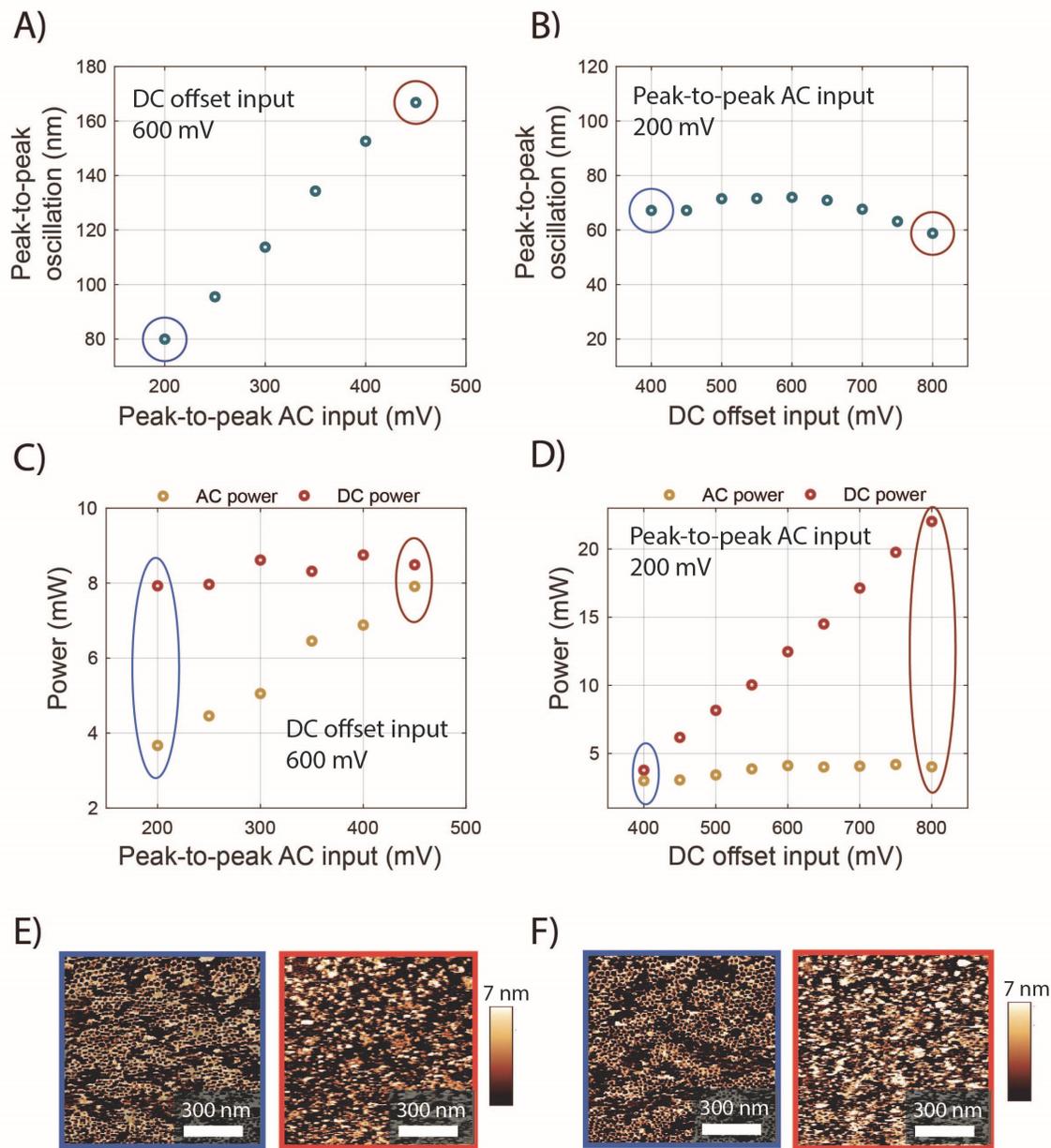


Figure 2.4 (Effect of peak-to-peak AC input voltage DC offset input voltage): Effect of increasing the (A) peak-to-peak AC input voltage and (B) DC offset input voltage on the peak-to-peak oscillation of the cantilever. Effect of increasing (C) peak-to-peak AC input voltage and (D) DC offset input voltage on AC and DC laser power. Imaging quality at minimum (circled in blue) and maximum (circled in red) (E) peak-to-peak AC input voltage and (F) DC offset input voltage. When increasing the

peak-to-peak AC input voltage, the DC offset input voltage was kept at 600 mV. When increasing the DC offset input voltage, the peak-to-peak AC input voltage was kept at 200 mV. Sample integrity is compromised for the high-power configuration. The PORT rate was kept at 100 kHz, and the line rate at 100 Hz. Scale bar 200 nm. A force curve to obtain deflection sensitivity was taken after imaging.

Discussion:

When imaging delicate biological samples, off-resonance tapping imaging modes in AFM are particularly useful since they can directly control the tip-sample interaction forces¹⁸³. Among them, the PORT mode stands out due to the higher oscillation rates it can reach, which enables higher scan rates. As PORT directly and only actuates the cantilever with a laser, it allows excitation at much higher frequencies than conventional off-resonance tapping modes, particularly when using ultrashort cantilevers with high resonant frequencies¹⁷⁹. However, when using PORT for HS-AFM, one must be careful with the imaging parameters to achieve good imaging quality.

As depicted in Figure 2.2, increasing scan rates without simultaneously raising PORT rates will lead to bad-quality imaging. First, PORT rates resulting in less than one oscillation cycle per pixel will drastically reduce the image quality. The imaging speed is inherently limited by the rate at which the cantilever probes the surface with appropriate tip-sample force control. In PORT, the feedback control discretely acts at the end of every oscillation cycle¹⁹⁸. This limited sampling rate induces a pure delay in the feedback loop, thereby limiting the achievable feedback bandwidth. If the rate of topography change becomes too fast to track at the PORT

sampling rate, the topography can no longer be accurately detected or tracked by the feedback loop. The PORT rate, therefore, needs to be increased to faithfully resolve the sample at higher surface speeds. However, the cantilever's resonance frequency intrinsically limits the maximum PORT rate we can use. If the PORT rate is close to the cantilever's resonance frequency, the deflection measured by the optical lever method no longer faithfully represents the tip-sample forces. To obtain a proper tip-sample interaction curve, both the mechanical bandwidth of the cantilever and the electrical bandwidth of the AFM system must be large enough to detect Fourier components of the deflection curve that are several times that of the PORT frequency. If any of these bandwidths are too low, the interaction curve no longer shows the one-sided cut off (Figure 2.3A), but rather a sinusoidal behavior (Figure 2.3D) which obscures the actual tip sample interaction (Figure 2.3E). This leads to poor force control in the imaging (Figure 2.3F). Even smaller cantilevers displaying high resonance frequency, which possess at the same time low spring constants are therefore required to increase the PORT rate further. Such high PORT rates and scan speeds present a challenge for AFM electronics, requiring a careful software and electronic design that features the required high bandwidths and optimized digital signal processing strategies.

One of the advantages of PORT compared to tapping mode high-speed AFM is that the surface sampling speed can be tuned. In tapping mode AFM, the surface sampling rate is given by the resonance frequency of the cantilever. When operating in PORT well below the cantilever resonance frequency, we assume that each surface sampling provides a valid data point. As such, the PORT detection bandwidth is given by the Nyquist frequency at half the PORT rate.

In the case of tapping mode, the detection bandwidth is given by $f_0/2Q$ ¹⁹⁹. With the latest developments in PORT, we can gradually increase the PORT rate up to the resonance frequency. In that situation, PORT and tapping mode become almost identical because, at those frequencies, PORT cannot accurately detect the cantilever-to-tip sample interaction, as shown in Figure 2.3E. When operating at the resonance frequency, the larger oscillation amplitude of PORT compared to the tapping mode becomes a disadvantage. The goal for increasing the PORT imaging rate, therefore remains to increase the cantilever resonance frequency to maintain operation with the PORT rate far enough below the resonance frequency.

As we increase the PORT rate to enable faster scan rates, we will face another problem inherent to photothermal cantilever excitation: at higher frequencies, the oscillation amplitude reduces due to a decrease in photothermal excitation efficiency, eventually to the point that we need to increase the laser power, resulting in sample's temperature rising. Increasing the PORT rate will encumber the balancing of laser power and oscillation amplitude, since a higher excitation power is required to compensate for a reduced actuation efficiency that leads to sample damage. At higher levels of laser power, we could no longer observe the sample, despite using the lowest possible force set point (right panels in Figure 2.4E,F). We need to be careful about how we will increase the cantilever oscillation amplitude and increase the laser power. There are two parameters we can tune to increase the laser power. First, the peak-to-peak AC input which controls the sinusoidal signal sent to the laser diode to sinusoidally vary the delivered laser power intensity. Second, the DC offset input voltage that keeps the laser diode on the conduction regime and, therefore lasing. An increase of the first one has to be combined with

an increase of the second one since an increase in the amplitude of the AC signal sent to the laser requires an increase of the DC voltage to avoid crossing the lasing threshold. However, only the peak-to-peak AC input influences the cantilever oscillation amplitude, as displayed in Figure 2.4A. DC voltages do not lead to variations in oscillation amplitudes (Figure 2.4B). Thus, if we want sinusoidal actuation, we need to set the DC voltage to the minimum voltage that lets the diode laser be in the lasing regime. Alternatively, we can minimize the heating by periodically switching the laser diode off and back on during each oscillation cycle rather than using a full sinusoidal drive¹⁷⁹. The temperature oscillation required to actuate the cantilever in photothermal excitation can be more efficiently reached by switching off the laser during a portion of the cycle, which drops the temperature of the cantilever and, therefore, leads to cantilever bending. This will minimize the delivered energy to the cantilever and sample and thus decrease the total temperature in the surroundings, mitigating sample heat damage.

In this study, we show the limits of imaging parameters in HS-PORT that prevent heat sample damage and proper feedback control. Understanding these limits will help make the best use of the current state of the PORT AFM method, allowing better control over the tip-sample interaction and helping to preserve the native state of the DNA motifs in these measurements. Thanks to the high scan rates reached combined with good feedback control, PORT allowed us to obtain clear and detailed images of the DNA 3PS and their interactions^{7,8,36}. With the possibility of increased imaging speed and direct tip-sample force control¹⁴⁷, we are able to track the growth and reorganization of biomolecular assemblies more precisely and observe detailed dynamics.

Acknowledgments:

The authors thank Raphael Zingg for help with programming of the python script for image series processing. GEF acknowledges funding from H2020 - UE Framework Programme for Research & Innovation (2014-2020); ERC-2017-CoG; InCell; Project number 773091. VC acknowledges that this project has received funding from the European Union's Horizon 2020 research and innovation programme under the Marie Skłodowska-Curie grant agreement No. 754354.

3. Structural flexibility dominates over binding strength for

supramolecular crystallinity

This chapter is a copy of the manuscript in review with the peer-reviewed journal, Nature Chemistry. We use static and high-speed AFM to observe the assembly of DNA 3 point star, and observe the effects of changing the terminal ends and arm lengths on the patterns. My contribution to this chapter includes developing the imaging protocol, collecting and analyzing the high-speed imaging data and contributing to ideas for future work.

The temporary version of the article is available at:

Structural flexibility dominates over binding strength for supramolecular crystallinity

Veronika Cencen*, Vincenzo Caroprese*, Cem Tekin*, Majid Mosayebi, Tanniemola B. Liverpool, Derek N. Woolfson, Georg Fantner, Maartje M.C. Bastings

bioRxiv 2023.09.04.556250; doi: <https://doi.org/10.1101/2023.09.04.556250>

* The authors contributed equally to this work

Supplementary information and figures for this article are provided in the Chapter 7 (Appendix) of the thesis.

Abstract

Supramolecular crystallinity is a phenomenon abundantly present in nature that results from directional non-covalent interactions between components. Bottom-up nanotechnology aims to use this approach to control the self-assembly of 2D ordered networks through rational design

of macromonomers. Like all crystalline materials, 2D supramolecular crystals develop from an initial nucleation site, followed by growth, based on directional interactions. Traditionally, the binding strength and directionality of interactions is thought to dictate the nucleation and crystal growth, whereas structural mobility favors defects. Usually, macromonomers present multiple binding units, which exhibit a relative intramolecular flexibility, affecting their intermolecular interactions. The effect of this relative flexibility has thus far not been elucidated. Here we introduce the concept of “interface flexibility” and demonstrate its critical importance to nucleation and growth of supramolecular crystalline networks from DNA-based macromonomers. We show that tuning the interface flexibility greatly expands the available design space for synthetic supramolecular crystalline materials.

Introduction

Crystal formation is a complex process that involves both physical and chemical mechanisms, yet always starts with several molecules coming together to create a stable nucleation event.²⁰¹ This process is driven by many properties of the system, balancing concentration, diffusion and surface energies.^{202,203} In traditional covalent crystals, the bonding between atoms is typically strong and directional, yielding a highly ordered and stable crystal structure.²⁰⁴ Supramolecular crystals show a more flexible and dynamic structure, often attributed to the weaker and non-directionally of their intermolecular bonds.^{205,206} This implies that structural mechanics of the macromolecular unit cell plays a critical role in the formation of supramolecular crystals.

Dynamic, yet controlled self-organisation of macromolecules into temporal geometric domains allows for the engineering of functional interfaces for catalysis, materials and

nanotherapeutics.^{207,208} While challenging for engineers, these supramolecular crystalline networks are fundamental for many biological processes. The assembly of clathrin triskelions into polygonal patches enables cellular uptake^{209–211}, while the organisation of TRIM5a in hexagonal patterns on the HIV-1 capsid combats viral infection.²¹² Traditionally, the main parameters used to design directional multivalent interactions are binding strength (affinity) and number of binding events (valency).²¹³ Interestingly, both clathrin and TRIM5a use additional structural changes to transition from monomer into their characteristic geometric pattern.^{209,212} Consequently, the nucleation of these crystalline networks is influenced by local changes in mechanical properties of the monomers, which influence the spatial tolerance of the intermolecular binding interface and thereby impact the systems' capacity to acquire long-range crystalline order. While the structure-function connection of these biological phenomena is evident, their complex multicomponent environment limits a systematic manipulation of molecular parameters to explore the role of interface mechanics in nucleation and growth of supramolecular crystalline networks.

Similar to nucleation in covalent crystals, non-covalent interactions in supramolecular crystalline materials showcase a directional component at the intermolecular interface.²¹⁴ A deepened understanding of the flexibility limits of bond directionality at the supramolecular interface could translate into novel engineering strategies to tailor the nucleation of such materials. To enable a detailed molecular analysis of the structural design parameters that influence the nucleation and growth mechanisms of supramolecular networks, modular monomers without complexity of biology are essential. While protein-engineering approaches toward geometric networks have shown beautiful lab-made examples^{215–217}, modulation of

flexibility and affinity is not straightforward without fully altering the monomer building block. In doing so, one risks to disrupt the integrity of secondary structural components as well as the global geometry of the original molecule. Furthermore, directional interactions at protein-protein interfaces quickly engage a large number of amino acids and render the detailed understanding of local effects challenging. At micron length scales, colloidal supramolecular crystals guided by molecular recognition at the interface present impressive degrees of programmable design,^{218–220} yet the effect of nuanced changes in structural mechanics get lost in the overall system dimensions.

Contrary to protein-based monomers and colloids, DNA-nanotechnology¹³² offers a predictable and modular platform to decouple the interplay between macromolecular flexibility and monomer-monomer affinity. When using synthetic DNA as material tool, structural flexibility can be controlled by the balance of single-strand (ss) versus double-strand (ds) sections, as well as the overall length compared to the persistence length of the DNA double helix.²²¹ Affinity can be manipulated through the length of single strand complementary ends (so called “sticky ends”) or the nucleotide sequence at the end of a “blunt end” double helix, as GC presents a stronger π - π stacking interaction than TA.¹³⁶ Utilizing the multivalency concept, a higher affinity interaction can be designed by systematic multimerization of adjacent DNA blunt-ends. Combined, these characteristics make DNA an ideal model material to explore if changes in structural rigidity at the intermolecular interface can indeed control the nucleation-growth mechanisms in supramolecular 2D crystalline materials.

Results and discussion

Characterization of macromolecules with variation in structural flexibility.

DNA-based macromonomers assembled from a limited number of oligonucleotides (“tiles”) have been designed and used to engineer a range of simple to highly complex supramolecular systems.²²² When multiple helices are present in parallel, the distance from a DNA cross-over junction affects the spatial freedom at the end of a DNA helix extension.²²³ We used the established DNA 3-point-star (3PS) motif as starting point, which allows to build upon existing work on the supramolecular crystalline self-organisation of DNA-tiles²²⁴ (Supplementary Figure 0.1). This macromolecule presents a 3-fold rotational symmetry and consists of seven ssDNA strands - three unique sequences - organised in three four-arm junctions (Figure 3.1a). The conventional approach to obtain supramolecular crystals from DNA tiles is via the display of short ssDNA terminal ends that enable so-called “sticky-end” hybridization with their sequence-complement. These networks assemble in solution and show long-range order with very few defects.²²⁵ However, the use of sticky-ends comes at the cost of kinetic control and renders the analysis of self-assembly mechanisms related to monomer design obsolete. In a blunt-ended variant, the interaction-interface consists of a multivalent array of π - π stacking units, presented by the nucleobases. The geometric alignment of multiple of these weak interactions allows for a sufficiently strong directional force to self-assemble into 2D crystalline networks, while the inherent dynamics permit to target the nucleation-growth mechanisms of network formation.^{226,227}

To explore the impact of monomer mechanics on the growth and lattice structure, a second 3PS containing a 0.5 turn extension per arm was designed (Figure 3.1a, “long”). Not

only does this modification generate a larger star motif in terms of absolute size and corresponding global flexibility, the spatial tolerance of the arm termini (terminal flexibility) is also increased, as the two parallel helices have more freedom after the cross-over point to independently move. We let both systems assemble overnight (Supplementary Figure 0.2) and imaged the steady-state networks by atomic force microscopy (AFM). Clear differences between the steady state assembly of long and *short* 3PS were observed (Figure 3.1b). The *short* monomers predominantly formed large hexagonal networks, whereas the *long* monomers assembled into smaller, elongated islands. To explore if the difference between the designs was related to the monomer concentration, we imaged both systems at decreasing concentrations (Figure 3.1c). Measurements at higher concentrations were not relevant as these led to surface crowding and multilayer assembly (Supplementary Figure 0.3). For all dilutions, we consistently observed large islands for short 3PS and many small structures for long 3PS.

We developed a tailored detection algorithm in MATLAB²²⁸ which reliably identifies each island, 3PS monomer center and polygon present in a frame (Methods, Supplementary Figure 0.4). By considering each island as a network of polygons, we applied the concept of network density (ND)²²⁹ to quantify the degree of ideal radial growth within the assembled islands. In particular for our case, ND is expressed as the ratio between the number of observed polygons in an island, R_o , and the number of polygons R_i in ideal island formed by the same number of particles, arranged in a hexagonal symmetry and assembled by radial growth (Supplementary Figure 0.5). For values of the ND closer to 1, the island resembles an ideal crystalline network. When the values reported are less than 1, monomers are organized in a less efficient way, as is the case for more elongated assemblies. Application of the ND to all

steady state results confirmed the presence of 2 distinct, molecular architectures (Figure 3.1d.). The *short* 3PS follow the assembly of a radial crystalline network much closer than the *long* variant. From the *ND* approaching 1 for the lowest short 3PS concentration measured, we deduct that radial growth is hindered by coalescence of multiple islands in the higher concentration samples. Contrarily, the low *ND* value characteristic of the elongated assemblies seen in the long 3PS, is concentration independent. The small change in arm-geometry and terminal flexibility thus creates a significant impact on the global network self-assembly.

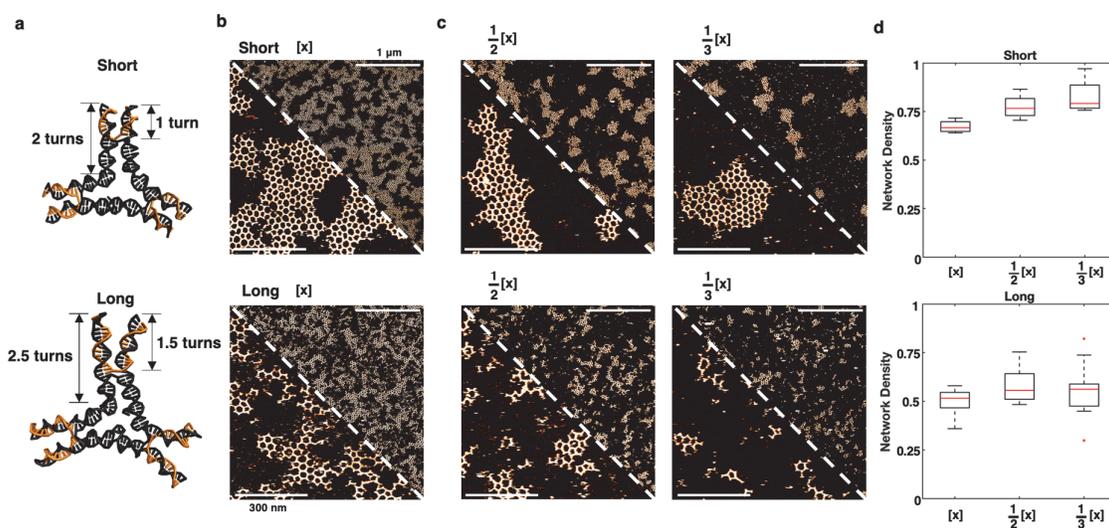


Figure 3.1 (Steady-state assembly of hexagonal lattices formed by short and long 3PS): a, DNA blueprint of the short and long monomers obtained from Molecular Dynamics simulations, indicating the overall and terminal arm-lengths in helix turns. b, AFM images of the steady-state networks formed by the short (top row) long (bottom) monomer. c, AFM images of the steady-state networks formed by the short (top row) long (bottom) monomer at decreasing concentration (x). d, Weighted mean of the Network Density as a function of monomer concentration. The red lines indicate the median. Outliers, defined as data points beyond 1.5 times the interquartile range, are represented as individual points. Upper scale bars 1 μm , zoomed-in lower scale bars 300 nm.

Decoupling the contribution of intermolecular affinity.

We next wondered if changes of intermolecular affinity could overcome the negative effects on lattice formation caused by structural flexibility. Within a DNA-based macromonomer, the intermolecular affinity can be tuned by the number of parallel helices (two in each 3PS arm) or the sequence of terminal nucleotides participating in the blunt-end π - π stacking interactions.¹³⁶ When fully surrounded by neighbours in a hexagonal arrangement, 3×2 directional π - π interactions are formed, stabilizing this rather weak binding through the strength-in-numbers principle of multivalency. Since the π - π stacking energy is defined by the chemical structure of the DNA nucleobase, the overall affinity between monomers can be controlled through the sequence of the terminal nucleotides. We therefore modified the original long and short 3PS motifs, displaying GC-TA as terminal nucleotide couple, to present either TA-TA or GC-GC as terminal nucleotide base couple (Figure 3.2a, Supplementary Figure 0.6 and Figure 0.7). This modification directly affects the π - π stacking energy, expected to range from $\Delta G \sim 2 \text{ kcal mol}^{-1}$ for TA-TA, to $\Delta G \sim 6.8 \text{ kcal mol}^{-1}$ for GC-GC.¹³⁶ The free energy of our supramolecular crystal is the lowest when monomers arrange into a hexagonal array, in which all arms of the 3PS are in a relaxed orientation and the number of π - π binding events is maximized. However, due to the flexibility present in the monomer structure, different polygons can be formed (so-called “errors”), which can be corrected by breakage of the π - π interaction and reorganization of the macromolecules into the ideal hexagonal lattice structure. We hypothesized that besides affecting global network formation, the choice of terminal nucleotide identity might also impact the local polygonal composition.

The sequence-library of 3PSs were left to assemble overnight and qualitatively, the steady state AFM showed consistent patterns within the groups of long and short monomers, respectively (Figure 3.2b), suggesting that intermonomer affinity had no significant impact on the global structure of the networks. When measuring the *ND* for all systems, increased affinity for short 3PS slightly enhances radial crystal organization, whereas no clear effect within the long 3PS was observed (Figure 3.2c).

For a quantitative analysis of the internal polygon composition, we extended the aforementioned image processing algorithm to automate the detection and labelling of polygonal geometries from 3 to 9 monomers in short GCTA versus long GCTA assemblies (Figure 3.2d, same analyses of TATA and GCGC are in Supplementary Figure 0.8). Indeed, the hexagonal organization is prevailing, with pentagonal and heptagonal assemblies responsible for the majority of defects. Upon plotting the hexagonal content within all polygons (Figure 3.2e), 2 conclusions can be drawn. First, the total amount of assembled polygons is significantly higher for the short 3PS compared to long 3PS molecules, indicative of a favored network growth mechanism. Second, the hexagonal content within the short 3PS is moderately dependent on the terminal affinity, with short GCGC and short GCTA presenting the most crystalline network, showcasing the fewest polygonal defects and highest *ND* (Figure 3.2e). This observation suggests that rigidity and affinity work together to create a more crystalline organization and that an affinity threshold exists after which hexagonal order is favored.

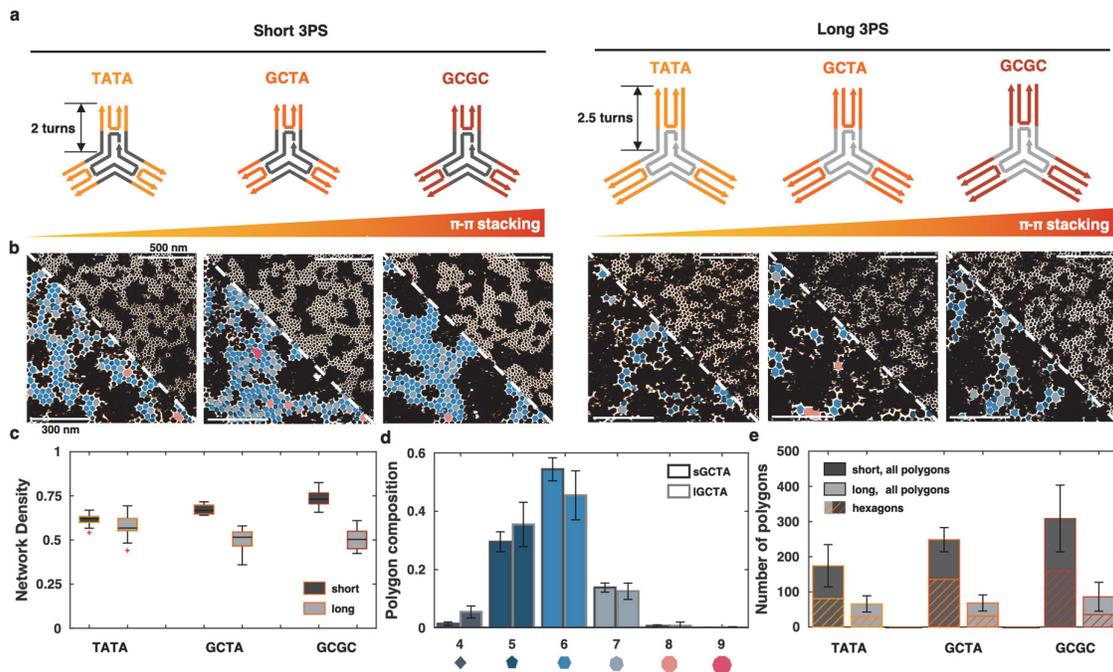


Figure 3.2 (Quantifying the effect of intermolecular affinity on network crystallinity): a, 3PS library, where each monomer has a unique combination of an arm length (2 or 2.5 turns) and a terminal base-pair (TA-TA, GC-TA or GC-GC). The blunt-end π - π interaction strength increases from left to right (from TA-TA to GC-GC). b, (top right triangle) AFM images of the assembly in steady-state (after 24 h) for each 3PS design. (bottom left triangle) Higher magnification and overlay of the polygon identification algorithm (pentagons=dark blue, hexagons=blue, heptagons=light gray). c, ND of all 3PS assemblies showcasing a moderate effect of affinity in short 3PS systems yet marginal impact in long 3PS systems. The boxes represent the middle 50% of the data, with the bottom and top of the box representing the 25th and 75th percentiles, respectively. The red lines indicate the median. Outliers, defined as data points beyond 1.5 times the interquartile range, are represented as individual points d, Polygon distributions for short GCTA versus long GCTA assemblies, using at least 12 regions with an area of 750x750 nm in at least 2 independent experiments. e, Average count of all polygons, with the hexagon contribution highlighted by the striped surface. Error bars represent the standard deviation.

Exploring the self-assembly mechanisms in real time.

The steady-state data of the 3PS library suggests fundamental differences in the assembly mechanism between the short and long monomer variants. Unfortunately, static AFM cannot provide details on the real-time dynamics of network formation. We therefore turned to high-speed (HS)-AFM^{230,231} in an attempt to visualize and analyze the mechanisms of assembly from the earliest interactions. Since its establishment, HS-AFM has become a popular and useful technique for visualizing biological processes in real time and at single molecule resolution. Using photothermal off-resonance tapping (PORT) mode^{226,232}, the risk of interference with the self-assembly process is significantly reduced, since we have better control over the tip-sample interaction forces. With a frame rate of 0.4 fps, the organization of 3PS macromolecules into the typical hexagonal patterns could be observed, starting from the moment of monomer injection (Figure 3.3a, Supplementary Videos 1 through 6). This approach allows to focus on the initial phases of supramolecular crystal nucleation, whereas previous static AFM analysis was performed after overnight annealing to visualize the systems' steady-state.

Upon qualitative observation, the long and short 3PS monomers show a distinct self-assembly pattern: where the short monomers quickly create stable assemblies, the long 3PS displays high dynamics and seems to not enter a stable growth regime. Few large islands, as seen for the short rigid 3PSs, suggest the presence of a stable initial nucleation event, followed by a radial growth. The multiple small and elongated islands observed in the long 3PS samples indicate a potential lack of stable nucleation. To quantify these differences, we identified all islands and particles present over time through the previously mentioned in-house pipeline (Figure 3.3b, Supplementary Figure 0.4). Indeed, the density of islands stays constant for the

short rigid 3PS, whereas for long flexible 3PS the number of islands continue to grow, all while the density of monomers steadily increases (Supplementary Figure 0.6) This confirms that all new incoming monomers attach to a stable nucleus and contribute to the growth of the supramolecular crystal for the short 3PS, whereas incoming large 3PS monomers try to form a nucleus and eventually upon crowding the surface, coalesce with other seeds into larger elongated structures.

Expanding the particle and polygon detection algorithm, we counted the fraction of polygons present on the border of biggest island (labeled as “1” versus those in the center labeled as “0”) and expressed it as a ratio in respect of the total number of polygons in said island (Figure 3.3c). Following an initial nucleation time, which for the short 3PS systems seem to last roughly 10 minutes, the first center-monomers (e.g. scores lower than 1) start to appear. Subsequently, the border fraction is decreasing making way for internally located polygons, a strong confirmation of radial island growth from an initial stable nucleus. The long 3PS shows a very different profile, as for the time of measurement, all monomers remained present in a border, either as polygon (“1”) or in an elongated polymeric conformation (“0”).

Combining HS-AFM and tailored particle detection analyses, the kinetic pathway behind the 2 different assembly behaviors can be composed. As π - π stacking is a weak interaction, the blunt-ended 3PS motifs only laterally interact when on a surface where they can freely diffuse when in a monomeric state. Due to the parallel alignment of DNA helices in the arms of the 3PS motifs, a multivalent array of π - π interactions is presented. Together with the structural tri-symmetry, stability of the assembly increases by multimerization of the stacking interactions when polygonal nuclei are formed. Nuclei are less diffusive than free

3PSs, because the larger contact area increases the amount of salt bridges with the mica surface. This reduced mobility of the 3PS allows the formation of stable nuclei and subsequent growth of supramolecular crystals. Contrary, for the long flexible 3PS, visibly no stable nuclei are formed, preventing the transition to a growth phase. Eventually, however, upon density increase the many small nuclei coalesce which creates the characteristic elongated island structures (Figur 3.3d) as previously observed in steady-state analysis.

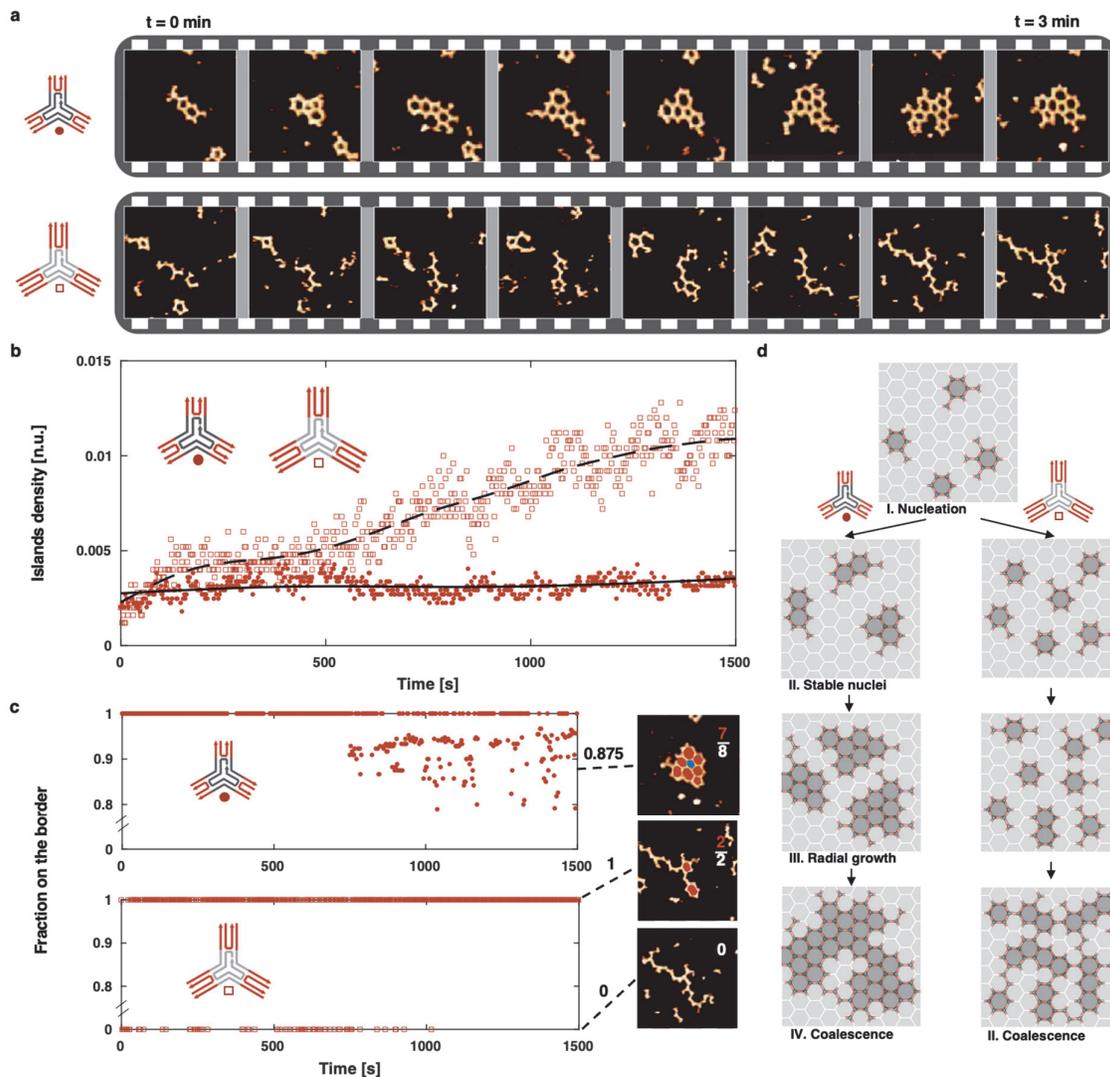


Figure 3.3 (HS-AFM detection of 2 distinct growth mechanisms): *a*, Time-lapse of short (top) and long (bottom) 3PS self-assembly over 3 minutes highlighting the difference in nucleation. Snapshots taken from full length timeseries. *b*, Detected Island density over time (25 minutes imaging) using tailored particle tracking algorithms for long and short 3PS. *c*, Quantification of radial crystal island growth through detection of fraction of polygons on a border (count=1) over the total number of polygons. When no polygons are present, count = 0. *d*, Schematic representation of the nucleation-growth self-assembly mechanism of short 3PS and coalescence-based elongated island formation of long 3PS.

Interface flexibility as determinant for stable nucleus formation.

With two such distinct kinetic pathways, the apparent next effort was to explore the main molecular feature causing this vast change in assembly mode. The observed differences in stable nucleus formation suggest the interface between both monomers to be significantly different. Said interface, per arm in a monomer, is formed by a pair of double stranded DNA helices. Considering the strong directional nature of the π - π stacking, the strength of interaction between two different particles is directly affected by the possible orientations that these helices (and in particular their termini) can assume: it will reach a maximum when the helices in each arm are parallel and rapidly fade away if the termini face in different directions, up to the point where at maximum one weak π - π bond can form. This lets us distinguish two possible states for an arm, respectively “open”, if the segments are tilted towards different directions, and “close”, if sufficiently parallel to form a double π - π interaction (Figure 3.4a). To quantify the distributions of long and short 3PS in either state, we used oxDNA^{233,234} (Supplementary Figure 0.10 and Figure 0.11) and a series of Molecular Dynamics simulations (Supplementary Methods). The sampled probability distribution functions of the end-to-end distance between DNA helices in an arm (Figure 3.4b) show that short 3PS presents a narrow distribution centered around ~ 2.7 nm, while long 3PS averages at ~ 3.2 nm but spans a wide range up to 6 nm. Comparing the distributions to the spatial tolerance to form two simultaneous π - π stacking interactions, expected to be 1.5-2.5 nm, the arms of short 3PS are almost four times more likely to be oriented in a strong bond-forming conformation than the arms of long 3PS. Therefore, the chance that long 3PS makes strong interactions, and thus stable nuclei, is significantly

reduced. This change in interface flexibility provides a potential explanation for the observed different mechanisms in supramolecular assembly.

We turned to Monte Carlo simulations²³⁵ as means to further explore the effect of interface flexibility and spatial tolerance of the π - π interface and its impact on supramolecular crystal nucleation in greater detail. A patchy-particle model was used to describe the 3PS motif as a particle formed by a repulsive core and 3 attractive sites equally distributed on its perimeter (Figure 3.4c) as this is a common approach to study directional interactions in macromolecular systems.²³⁶⁻²³⁹ The aforementioned “close” and “open” states were introduced into a classical Kern-Frenkel²⁴⁰ potential through the concept of “state” of a patch, where the variable assumes a value of 1 when representing close arms (indicating that the interface is available for binding) or 0 when the interface is open (detailed formulation in Supplementary Methods). Similar to an Ising model^{241,242}, each interface can switch states through a dedicated move following preassigned probabilities. We explored the parameter space representing the ensemble of interface flexibility by varying the state-switching probabilities and the strength of interaction. This allowed us to recover states that are qualitatively and quantitatively similar to the ones obtained in our steady state AFM measurements (Figure 3.4d), confirming that solely the interface flexibility can define the nucleation-growth mechanism. Finally, using the Network Density and island size as observables to distinguish between different assembly mechanisms, akin to experimental interpretation, we constructed a complete phase diagram (Figure 3.4e). We were able to observe states that match our long 3PS and short 3PS, labelled respectively: long-like and short-like. Additionally, we report conditions where only gas or small aggregates are present, conform to literature reports.²⁴³ We here show that when a sufficient strength of

interaction is combined with a corresponding probability of opening, it is always possible to observe aggregates that do not grow following a radial symmetry, even if they form reversible bonds (long-like state). This state, to the best of our knowledge, represents a unicum since elongated structures are typically observed only when approaching the Diffusion Limited Aggregation conditions (i.e. to the limit of infinite interaction strength).²⁴⁴⁻²⁴⁶

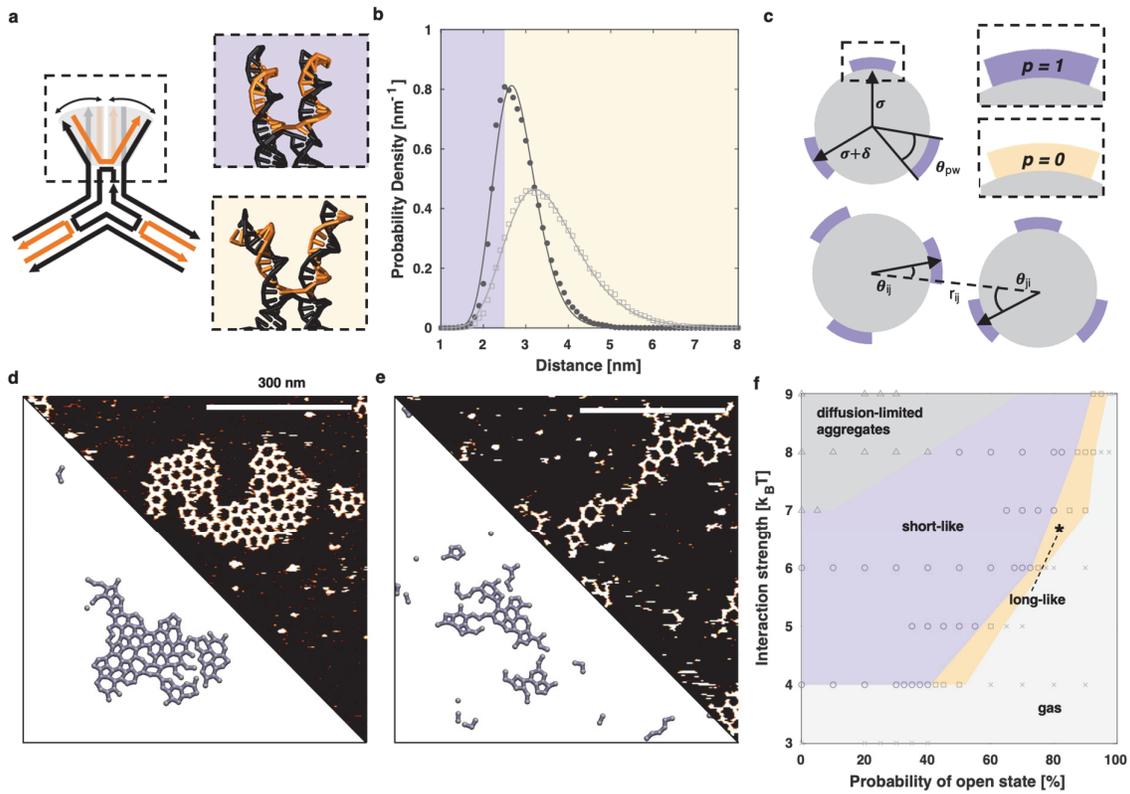


Figure 3.4 (Importance of interface flexibility): *a*, Representation of interface flexibility related to the mobility of the peripheral segments of DNA following the Holiday junction. The detail in the upper box represents an aligned, “close” configuration that allows directional binding; the detail in the lower box represents a wider, “open” configuration that is unavailable for binding. *b*, Probability distribution of end-to-end arm distances at the π - π interface based on oxDNA simulations of the 3PS monomers. The purple area highlights when the arms are in a close state, whereas yellow is used for the open state. *c*, Patchy particle model for Monte Carlo simulations with highlight on the patch state variable p , showing when it represents close ($p=1$) and when open ($p=0$). The other represented variables are: σ , the diameter of the hard core repulsion; δ , the attractive range; ϑ_{pw} , the patch width; r_{ij} , the center-to-center distance connecting particle i to particle j ; ϑ_{ij} (ϑ_{ji}), the angle formed by the orientation of the interacting patch on i (j) and the direction of the distance r_{ij} (r_{ji}). *d*, *e*, Comparison of simulation results, bottom, and experimental measurements, top of short 3PS (*d*) and long 3PS (*e*). The selected frames are taken from simulations presenting similar values of average MND as the experiments. *f*, Phase diagram in function of probability to be in the open state and interaction strength. In dark gray diffusion-limited aggregates, purple short-like phase, in orange long-like phase, in light gray gas phase. Each datapoint represents a set of conditions simulated.

Restoring the interface rigidity.

The significant change in self-assembly mechanism caused by differences in interface flexibility prompted us to redesign the long 3PS and restore the more rigid interface as present in the original short 3PS. For the initial long 3PS design, the arms were terminally extended by 5 nucleotides while the central DNA strand, and with that the cross-over point to the arms, was unaffected. As such, 2 sites of flexibility are present: a global arm flexibility due to the extended overall length, and secondly, the prolonged distance from the cross-over point results in a considerable local flexibility at the 3PS periphery (Figure 3.5a,b). To restore the interface flexibility by peripheral alignment of terminal helices, and hypothetically return to a nucleation-growth profile for long 3PS, we modified the position of the cross-over point of a new “rigid” long 3PS design (Figure 3.5a,b, Supplementary Figure 0.12). Simply moving the DNA cross-over position does not alter the chemical composition or overall monomer design, yet is an effective modification to change structural rigidity, exemplary of the strategic modularity present within DNA nanotechnology.²²³ OxDNA simulations of all 3PS designs indeed show changes in global and peripheral flexibility between design and confirm that by moving the cross-over position, the new long “rigid” 3PS monomer presents the same local interface rigidity of the short 3PS (Supplementary Figure 0.13). Since the overall arm length is the same as the original long 3PS, the global flexibility resulting from the overall arm length corresponds to that found in the original long 3PS.

To experimentally confirm that interface flexibility is the leading regulator of supramolecular nucleation and crystal formation, we repeated all assembly experiments with

the new rigid long 3PS motif. To our excitement, radially grown large networks were visible (Figure 3.5c) and moreover, these were present in all dilutions with a network density score matching that of the original short 3PS (Figure 3.5d). Interestingly, the polygonal composition seemed to contain more pentagonal defects as observed for the short 3PS monomers. Indeed, polygonal quantification confirmed the distribution to be more similar to that observed for the original long 3PS (Figure 3.5e), however, with increased contributions of pentagons and higher order polygons. While the peripheral rigidity and restores the interface flexibility and mechanism of nucleation and growth, the crystallinity of these networks is still dominated by global flexibility.

Finally, we investigated whether the restoration of the radial growth could have been the result of a confounding factor such as the increased width of the interface resulting from the increased global flexibility. For this reason, we explored in our Patchy Particle model the parameter space described by the patch width, reflecting the global flexibility contribution to the interface, and the probability of being in an open state (Figure 3.5e). For the interaction strength defined by the regime of DNA blunt-end stacking, the dependency of the short-long phase boundary to the open/close probability fades away for increasing of the patch width (value for 3PS particles is ~ 0.3 , based on the polygon fractions reported in Supplementary Figure 0.14). This signifies that the assembly mechanism is indeed independent of global flexibility, and fully controlled by interface flexibility.

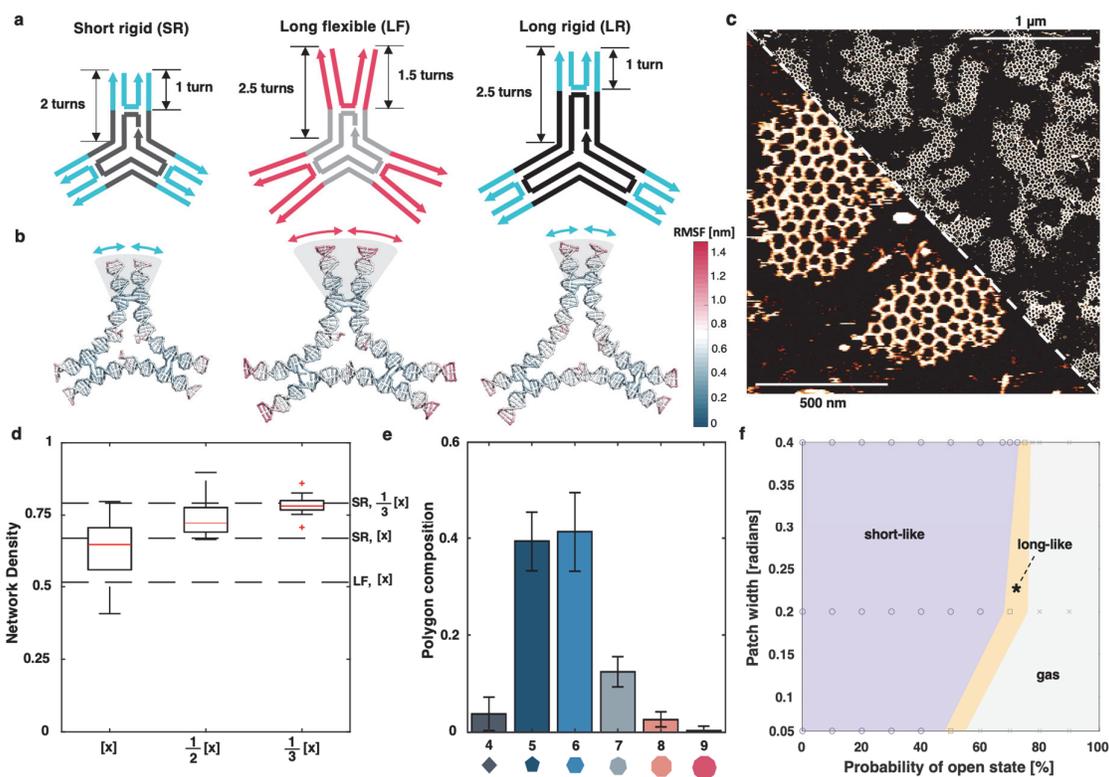


Figure 3.5 (Restoration of peripheral rigidity): *a*, Design of long “rigid” (LR) 3PS and comparison of local and global flexibility with the original short (rigid) (SR) 3PS and long (flexible) (LF) 3PS. *b*, representative frames from oxDNA simulations of the 3PS, colored by the average RMSF. *c*, Steady-state AFM of LR 3PS, showing a restored radial large network assembly. *d*, ND of long rigid 3PS assemblies at decreasing concentrations (x , $1/2x$ and $1/3x$), dashed lines represent references for short rigid (SR) and long flexible (LF) monomers. The AFM images of $1/2x$ and $1/3x$ are shown in Supplementary Figure 0.15. *e*, Polygon distributions for long rigid 3PS assemblies, using at least 12 regions with an area of 750×750 nm. Error bars represent the standard deviation. *f*, Phase diagram in function of probability to be in the open state and patch width. In purple short-like phase, in orange long-like phase, in gray gas phase. Each datapoint represents a set of conditions simulated.

Discussion

In this study, we set out to explore the interplay of affinity and structural rigidity to control the growth and geometric order of supramolecular crystalline materials. To this end, we choose to exploit the programmable nature inherent to the DNA macromolecule, in order to engineer a series of monomers of matching molecular content, yet containing nuanced differences in structural mechanics and chemical composition. As such, affinity was controlled through terminal nucleotide identity, directly impacting the π - π stacking energy. While only a weak interaction in solution, no self-assembly happens when monomers are freely moving in their solvent. Following surface adsorption, the planar tri-symmetry of the monomer stabilizes the directional multivalent π - π interactions and long-range ordered networks can be formed. The short 5nt arm extensions caused the introduction of global flexibility of the full arm, as well as local flexibility at the 3PS periphery. This change in structural mechanics not only affected the polygon composition, but drastically altered the global self-assembly mechanism. HS-AFM allowed to visualize and understand that the dynamics of nucleation in the more flexible monomer was too high, challenging stable nucleation. Only small, elongated islands formed via coalescence of nuclei were observed.

The π - π stacking interaction has a high directionality and thus a low spatial-tolerance. Consequently, small changes in orientation directly impact directional assembly. Nucleation seeds need to have a certain stability and lifetime to allow their transition into stable seeds and promote network growth, which is lost when the interface is too flexible. With the help of Monte-Carlo simulations, we demonstrated the critical effect of interface flexibility as defining parameter of network formation. When the interface is too flexible, no stable nuclei can be

formed and supramolecular network formation is compromised. Only when interactions fall within the directional spatial tolerance of the non-covalent interaction engaged in the molecular design, the system can form stable nuclei and continue into a growth phase. We experimentally confirmed that when the interface rigidity was restored, the nucleation-growth mechanism was recovered. Spatial tolerance in directional multivalent interactions, classified as *interface flexibility*, is therefore a critical parameter for the supramolecular self-assembly of macromonomers when long range growth and order is desired.

Taken together, our study shows that a subtle change in local structural flexibility can have a significant effect on the systems' global self-assembly, guided by interface flexibility. While demonstrated with DNA-based monomers in this study, these fundamental insights translate beyond the DNA helix. While any supramolecular network is assembled through non-covalent interfaces between macromonomers, the size and nature of the macromolecular building block defines the extent of interface flexibility to play a critical role in its' growth mechanism. As is evident, fully rigid macromonomers will not be affected as a certain degree of flexibility at the intermolecular binding interface needs to be present. Flexible-to-rigid transitions in biological macromonomers are surprisingly common, resulting from lateral interactions between monomers as seen in the example of the clathrin triskelion as well as via the addition of helper proteins in the case of the TRIM5a organization. While constructed from very different biological building blocks, these systems only assemble into geometric networks when the macromonomers are temporarily rigidified. Indeed, clathrin's ability to "shapeshift" is thought to contribute to the diversity of lattice structures and therefore its multiple cellular functions.⁵² With insights obtained in this study, we may start to look at

biological transitions of flexibility and order with new appreciation for structural protein monomer design and their transient interfaces. Reversibly, the intentional introduction of interface flexibility can be used strategically when the formation of large supramolecular networks is not desired or should be disrupted (e.g. in the case of plaques, fibres, amyloids or even viral (dis)assembly). The presented study on the fundamental role of interface flexibility to control the mechanisms behind dynamic self-organization, enables the design of synthetic macromolecular building blocks showcasing predictable organization at the liquid-solid interface. Exploiting the global and local rigidity/binding affinity balance at biological interfaces presents new opportunities for the engineering of dynamic cellular nanotherapies and controlled growth -or disruption- of molecular networks.

Methods

Full materials and methods and additional characterization can be found in the Supporting Information to this manuscript.

Preparation of DNA 3PS motifs.

For each 3PS, ssDNAs were mixed at the assigned molar ratios in the annealing buffer containing 5mM TRIS (Bio-Rad), 1mM EDTA (ITW Reagents) and 10mM MgAc₂ (abcr GmbH) to give a final solution of 0.6 μ M DNA motif in 50 μ L (pH adjusted to 8.0). The DNA solutions were annealed at: 80 °C for 5 minutes, 60 °C for 10 minutes, cooled from 60 °C to 20 °C by 1 °C every 10 minutes, 20 °C for 10 minutes and stored at 4 °C.

Static AFM imaging.

40 μL of DNA tile at designated concentration was deposited on a freshly cleaved mica (grade V1, Ted Pella). Mica was placed in a petri dish containing 1mL water to create a humid environment and sealed with Parafilm. The sample was left overnight for self-organization on mica surface before imaging. All AFM images were acquired in tapping mode in liquid on a Cypher VRS (Asylum Research Inc.) using BioLever mini cantilever (BL-AC40TS-C2, Olympus).

HS-AFM imaging.

Images have been acquired on a home-built small cantilever AFM with photothermal excitation as described elsewhere.^{226,232} All images were acquired in photothermal off-resonance tapping mode at frequencies of 100kHz using AC10DS cantilevers (Olympus). 50 μL of 10mM MgAc₂ was injected close to the cantilever in the dedicated channel of the cantilever holder. The cantilever was approached to the surface and the surface was scanned to check for contaminations. The cantilever was retracted from the surface, the buffer extracted from the holder, and 50 μL of the DNA 3-point-star (3PS) solution injected and imaged immediately. The sample was scanned at a line rate of 100 Hz (256 lines \times 256 pixels) unless otherwise specified. The setpoint was kept at the lowest level required for proper tracking.

Automated analyses of assembled networks.

Extraction of information from AFM images has been carried through a custom MATLAB²²⁸ routine of (1) opening and standard AFM artefacts removal, (2) segmentation and skeletonization, (3) polygon and particle detection, and (4) collection of observables per connected component (island).

OxDNA simulations.

We prepared a vHelix²⁴⁷ in Maya²⁴⁸ model for all compounds with GC TA as terminal base couple, which was subsequently converted it in oxDNA^{233,234} compatible formats for coordinates and topology using TacoxDNA.²⁴⁹ Unless stated otherwise, simulations follow standard settings for the base dependent forcefield (oxDNA2) and a salt concentration of 0.5M. The pipeline involved a minimization of 1e6 steps using the steepest descent algorithm. 8 sets of molecular dynamics run in NVT ensemble where we progressively increased the temperature using the following ramp: 1, 1, 10, 10, 20, 20, 25, 25. Until this moment we kept the restraints between base-pairs using the standard settings generated with the related tool in OxView^{250,251} and used a timestep of 5e-4. We then set the timestep to 1e-3 and proceeded with a last simulation at 25 °C for 5e6 steps where we halved the strength associated to the restraints before starting our production run at the same temperature without base pair restraints. During the production runs, configurations were stored every 5e5 steps. Resulting files were converted to psf, pdb, and mdcrd files using an inhouse python script. Analysis, snapshots and measures were then performed using VMD^{252,253} and MATLAB.

Patchy-particle simulations.

MonteCarlo simulations are run on a modified version of the engine developed by Hedges²⁵⁴, available on line. A modified version of the Kern-Frenkel potential²⁴⁰ was implemented in order to take into account patch states and adhesion to mica. Detailed formulation of the potential and specific parameters used in each set of simulations are given in SI. The recorded trajectories were rendered as images using VMD and analyzed in MATLAB following similar

procedures as for the experimental AFM data. Details about the potential used and the specifics of the simulations are reported in Supplementary Notes.

4. Mechanical properties of soft biological membranes for organ-on-a-chip assessed by bulge test and AFM

This chapter is a copy of the manuscript published in the peer-reviewed journal ACS Biomaterials. We measure the young's modulus of two types of hydrogel membranes using AFM force-volume measurements, as well as the bulge test. My contribution to this work includes AFM stiffness measurements of the samples, including adapting the sample design to the combined systems AFM setup and analysis of the data.

Mechanical Properties of Soft Biological Membranes for Organ-on-a-Chip Assessed by Bulge Test and AFM

Pauline Zamprogno*, Giuditta Thoma*, Veronika Cencen, Dario Ferrari, Barbara Putz, Johann Michler, Georg E. Fantner, and Olivier T. Guenat

ACS Biomaterials Science & Engineering 2021 7 (7), 2990-2997 DOI: 10.1021/acsbmaterials.0c00515

*The authors contributed equally to this work

Abstract

Advanced *in vitro* models called “organ-on-a-chip” can mimic the specific cellular environment found in various tissues. Many of these models include a thin, sometimes flexible, membrane aimed at mimicking the extracellular matrix (ECM) scaffold of *in vivo* barriers. These membranes are often made of polydimethylsiloxane (PDMS), a silicone rubber that poorly mimics the chemical and physical properties of the basal membrane. However, the ECM and its mechanical properties play a key role in the homeostasis of a tissue. Here, we report about biological membranes with a composition and mechanical properties similar to those

found *in vivo*. Two types of collagen-elastin (CE) membranes were produced: vitrified and non-vitrified (called “hydrogel membrane”). Their mechanical properties were characterized using the bulge test method. The results were compared using atomic force microscopy (AFM), a standard technique used to evaluate the Young’s modulus of soft materials at the nanoscale. Our results show that CE-membranes with stiffnesses ranging from several hundred of kPa down to 1kPa can be produced by tuning the CE ratio, the production mode (vitrified or not), and/or certain parameters such as temperature. The Young’s modulus can easily be determined using the bulge test. This method is a robust and reproducible to determine membrane stiffness, even for soft membranes, which are more difficult to assess by AFM. Assessment of the impact of substrate stiffness on the spread of human fibroblasts on these surfaces showed that cell spread is lower on softer surfaces than on stiffer surfaces.

Introduction

In vivo, cells reside in a complex microenvironment that is constantly exposed to endogenous and exogenous forces. These forces are transferred to the cytoskeleton via integrins and the extracellular matrix (ECM). The mechanical properties of the ECM strongly influence cellular morphology, proliferation, and differentiation.^{255–257} In the human body, the mechanical properties of different tissues vary according to composition and location. Most organs, such as the lungs, brain, or kidneys, are compliant and have a stiffness lower than 15 kPa.²⁵⁸ Therefore, soft materials are required to reproduce the physiological microenvironment of cells in *in vitro* systems.

Organ-on-a-chip (OOC) technology often uses polydimethylsiloxane (PDMS) membranes to reproduce the *in vivo* barrier. Because of the mechanical properties of this material, OOC membranes can stretch to mimic breathing^{259,260} or heartbeat^{261,262} motion. PDMS has several advantages: it can easily be microstructured using soft lithography, it is permeable to oxygen, optically transparent, biocompatible, and cost-effective.²⁶³ However, it also has several limitations, of which an important one is a high propensity for ad- and absorption of small molecules such as drugs.^{264,265} In addition, it is an artificial substance and thus does not mimic the chemical composition of the ECM. To overcome these limitations, collagen-based membranes integrated in OOCs were recently developed.^{266–269}, The biological and structural properties of the membrane can be tuned by changing the composition and concentration of the membrane materials to mimic the ECM properties of a specific tissue.²⁷⁰ Collagen is biocompatible, biodegradable, and can easily be structured into a scaffold. Collagen-based membranes can mimic the chemical composition and structure of the *in vivo* ECM, and unlike PDMS, they do not show high ab- and adsorption capacity.²⁶⁷ Combinations of collagen and elastin are used to develop living tissues such as cardiovascular, skin, liver, and musculoskeletal tissues.²⁷¹

Atomic force microscopy (AFM)-based testing is one of the most commonly used methods to characterize biological membranes.^{272,273,274} However, although imaging and mechanical sensing by AFM appear straightforward, several intricacies complicate the acquisition of quantitative data, making the method time- and labor-intensive.²⁷² Furthermore, AFM provides local stiffness values that do not necessarily reflect the average stiffness of the material. Sheng *et al.*²⁷⁵ recently reported the use of the bulge test, a method developed for rigid thin films²⁷⁶,

for the mechanical characterization of soft membranes. In this non-destructive method, the mechanical properties of the analyzed material are determined by measuring the relationship between the deflection of freestanding membranes and the applied pressures.^{277,278,279}

In this study, we describe two types of biological membranes made of collagen and elastin (CE) supported by a gold mesh, namely, vitrified and non-vitrified (called “hydrogel”) CE-membranes. We report the mechanical characterization of these membranes using AFM and the bulge test method. The mechanical properties of the membranes were assessed as a function of several parameters, such as the concentration of collagen and the fabrication temperature. The effect of the membrane’s stiffness on biological systems was assessed by evaluating the morphological behavior of lung fibroblasts cultured on the membranes.

Materials and Methods

Production of the CE-membrane and chip fabrication

The production of the vitrified CE-membrane and the chip fabrication procedure were described earlier.²⁸⁰ In brief, the biological membranes were made of rat-tail collagen type I, high concentration (Corning, New York, NY, USA), and bovine neck elastin lyophilized powder (Sigma-Aldrich, Buchs, Switzerland). The two molecules were mixed at a ratio of 1:1 to a final concentration of 3.5 mg/mL in a pH 7.4 buffer. An 18 μm -thin gold mesh (Plano GmbH, Wetzlar, Germany) with hexagonal pores of 500 μm was used as a scaffold to create the biological membrane. The CE solution was pipetted directly over the gold mesh. After pipetting, the chip was immediately incubated at 37°C, 100% humidity, and 5% CO₂ for 1 h to

allow gelation of the membrane. For membranes produced at 4°C, the membrane was placed in the refrigerator overnight. For the hydrogel CE-membrane, the membrane was immediately hydrated using cell culture medium. For the vitrified CE-membrane, the membrane was dried at room temperature for 48 h before rehydration using cell culture medium for 2 h at 37°C. The membrane was sandwiched between a PDMS top layer and a polycarbonate bottom with double-sided tape (Figure 4.5). Prior to the membrane fabrication, the microfluidic device was sterilized with ozone (CoolCLAVE, Genlantis) and exposed to UV light for 45 min. A 10 µm-thin PDMS Sylgard 184 membrane produced as described previously²⁸⁰ was used as a reference material.

Bulge test

In the bulge test, uniform air pressure is applied to one side of a freestanding membrane, and the resulting deflection, called the bulge height, is measured. For a membrane with a circular shape, the pressure (P) is expressed as a function of the bulge height (h) as follows:

$$P = \frac{4\sigma_0 t}{a^2} h + \frac{8Et}{3a^4(1-\nu)} h^3$$

Eq. 4-1

where E and σ_0 are the Young's modulus and the residual stress of the membrane, respectively; t is the thickness; a is the radius; and ν is the Poisson ratio.²⁷⁶ Eq. 4.1 was applied to the hexagonal gold mesh, and the radius was obtained by averaging the diameters of the circles inscribing and circumscribing the hexagons. The membrane was deflected using a homemade electro-pneumatic system that generates a negative pressure that can be tuned up to 30 kPa.

The deflection was visualized with a 3D optical profiler (S neox, Sensofar, Spain), whereas deflection measurements were obtained using an AxioPlan2 Zeiss microscope equipped with an incubator. The deflection values were obtained by measuring the difference in height between the stretched and unstretched membrane using focus variations on the membrane surface at the center of a hexagon. The deflection of the gold mesh itself was subtracted from the total deflection value. The deflection values of the PDMS, the vitrified CE-membrane, and the hydrogel CE-membrane were determined using the following pressure ranges: 0–4 kPa for the PDMS and CE-vitrified membranes, and 0–2 kPa for the CE-hydrogel membrane, with increments of 0.5 kPa and 0.3 kPa, respectively. At least three membranes were tested per condition. The experimental pressure-deflection curves were analyzed using MATLAB software and fitted to Eq. 1, from which the Young's modulus was extrapolated. The membrane was in contact with the cell culture medium in the basolateral compartment during all deflection measurements.

AFM

AFM stiffness measurements were performed in-liquid (cell culture medium on the apical side of the membrane) using a customized Dimension Icon AFM head (Bruker Nano Surface, Santa Barbara, California, US) mounted on an inverted optical microscope.²⁸¹ For the measurement, seven layers of 10 μm -PDMS membranes were bonded on a glass slide and 4 layers of CE-vitrified membrane (pipetted at 3.2 $\mu\text{L}/\text{cm}^2$) were directly produced on this substrate. Force-volume image was acquired among a square of 30 μm x 30 μm at the center of the membrane. A minimum of 256 points were measured per membrane. The bead cantilevers CP-qp-CONT-

PS (sQube) with a 3.6 μm radius bead were used for indenting the membrane. Data analysis was performed using Nanoscope Analysis software (Bruker) and the Young's modulus was calculated using the Hertzian model.

Thickness measurement

The thickness of the vitrified CE-membrane was measured as described previously.²⁸⁰ In brief, the membrane was cut at the center and imaged using the reflective light microscopy mode of the AxioPlan2 Zeiss microscope. The thickness was measured using Axiovision software. For the hydrogel membrane, the thickness was measured with the same microscope as a Z-stack between the bottom and the top of the gel. To help identify the membrane surface and thus increase the accuracy of the measurement, graphite powder (obtained by scratching a pencil tip with a scalpel) was spread on the hydrogel CE-membrane. Four samples were measured for each condition.

Cell culture

The human fetal lung fibroblast cell line HFL-1 was obtained from ATCC (CCL-153) and cultured in F-12K medium (Gibco) supplemented with 1% FBS (Sigma) and 1% p/s. Cells were used between passages 25 and 27, and seeded on chips at a density of 8×10^3 cells/cm². The PDMS membrane was coated overnight with a solution of collagen I (Sigma-Aldrich) and fibronectin (Corning). The membrane was washed and then dried under UV for 45 min. After 24 h, cells were fixed and analyzed by immunofluorescence. All cell manipulations were

performed in a sterile flow hood, and cells were maintained at 37°C, 100% humidity, and 5% CO₂.

Immunofluorescence

The chips were washed three times with PBS (Phosphate-buffered saline), fixed with 4% paraformaldehyde (Sigma-Aldrich) for 10 min, and rinsed again three times with PBS. The cells were permeabilized with 0.1 % Triton X-100 (Sigma-Aldrich) for 10 min, washed three times with PBS, blocked for 45 min in a 2% BSA (Sigma-Aldrich) solution, and incubated in blocking solution containing Hoechst and actin for 1 h. After the incubation, the chips were washed three times with PBS. All immunostaining steps were performed at room temperature. Images were acquired using a confocal microscope (CLSM, Zeiss LSM 710) and Leica DMI400 (Leica Microsystems, Buffalo Grove, IL, USA), and analyzed using Fiji software.

Cell shape analysis

To quantify the variation in cell morphology, the cell shape index (CSI), a dimensionless quantitative measure, was calculated using the following equation:

$$CSI = 4\pi \frac{S}{p^2}$$

Eq. 4-2

where S is the surface of the cell and p is the perimeter. The surface and the perimeter were measured using Fiji software.

Statistics

Data are presented as the mean \pm standard deviation (SD). The significance of differences was assessed using the two-tailed unpaired Student's t-test. Statistical significance was defined as follows: * $p < 0.05$, ** $p < 0.01$, *** $p < 0.001$, and **** $p < 0.0001$. Statistical analysis was performed using GraphPad Prism 6 software.

Results

Formation of vitrified and hydrogel CE-membranes

The biological membranes were generated using a simple process based on surface tension (Figure 4.1). A drop of CE solution was pipetted onto a thin gold mesh. Two fabrication procedures were evaluated to produce a vitrified membrane or a hydrogel membrane. First, a gelation step was used to promote crosslinking of the CE molecules. This step created a hydrogel CE-membrane that could be used immediately as support for cells. To generate the vitrified CE-membrane, the CE solution was dried at room temperature for 2 days. This evaporation process created a vitrified CE-membrane that was 12-fold thinner than the hydrogel CE-membrane (Figure 4.6). The thickness of the vitrified CE-membrane was $8.2 \pm 2.0 \mu\text{m}$, whereas that of the hydrogel CE-membrane was $100.1 \pm 28.8 \mu\text{m}$ when $32 \mu\text{L}$ of the CE solution was pipetted onto the mesh. The vitrified CE-membranes were rehydrated in cell culture medium for 2 h before characterization.

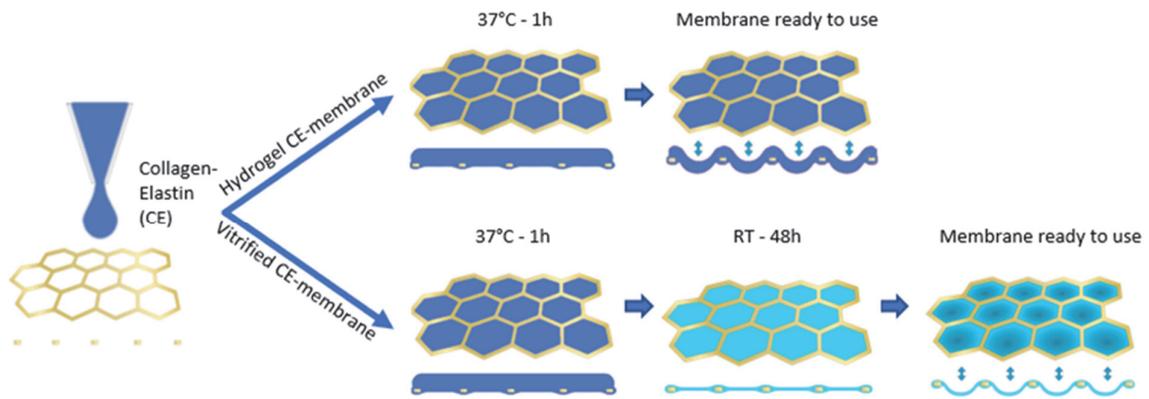


Figure 4.1 (Fabrication procedure of the hydrogel and vitrified CE-membranes.): Modified from Zamprogno et al.²⁸⁰ A drop of collagen and elastin is pipetted on a thin gold grid, which results in the spreading of the solution by surface tension force. Two membrane types were investigated. After gelation, the hydrogel membranes (top) were left in cell culture medium, whereas the vitrified membranes (bottom) were dried and rehydrated prior to characterization.

Mechanical characterization of thin membranes: AFM vs. bulge test

The two types of developed biological membrane were flexible and could be deflected when exposed to negative pressure (Figure 4.2A and Figure 4.7). The fabrication process affected the stretchability of the biological membranes (Figure 4.2B). At 0.5 kPa, the deflection was $51.4 \pm 3.1 \mu\text{m}$ for the hydrogel CE-membrane and $20.4 \pm 3.8 \mu\text{m}$ for the vitrified CE-membrane. Deflection was 2- to 3-fold higher for biological membranes than for the $10 \mu\text{m}$ PDMS membrane used as reference (Figure 4.2B). At 2 kPa, the deflection was $156.6 \pm 9.2 \mu\text{m}$ for the hydrogel CE-membrane, $65.0 \pm 5.0 \mu\text{m}$ for the vitrified CE-membrane, and $46.7 \pm 2.0 \mu\text{m}$ for the PDMS membrane. Young's modulus was extrapolated from the relation between the deflection of the membrane and the pressure applied (Figure 4.8). The Young's modulus

of the PDMS membrane ($E_{\text{PDMS}} = 380 \pm 46$ kPa) evaluated using the bulge test method was approximately 2-fold higher than that of the vitrified CE-membrane ($E_{\text{CE, v.}} = 173 \pm 37$ kPa), and approximately 200-fold higher than that of the hydrogel CE-membrane ($E_{\text{CE, h.}} = 0.79 \pm 0.36$ kPa) (Fig 4.2C). A slight, but not significant, increase in stiffness was observed after storing the vitrified CE-membrane at room temperature for 14 days (Figure 4.9). However, the membrane stiffness did not change after immersion in cell culture medium for 2 weeks at 37°C (Figure 4.10). The Young's moduli were also determined by AFM via the acquisition of force volume images (Figure 4.11). As the measurement of thin, suspended membranes is difficult with the AFM, layers of the respective materials were produced on a glass slide. The stiffness for the PDMS was of 629.7 ± 77.7 kPa, and 85.9 ± 19.1 kPa for the vitrified CE-layer. The variation of the AFM data is shown in Figure 4.12. The thicknesses of the layers were chosen so that the stiffness of the glass would not affect the measurement. The stiffness of the hydrogel CE-membrane was only evaluated with the bulge test because of the difficulty in identifying the contact point between the cantilever tip and the surface of the hydrogel using AFM.

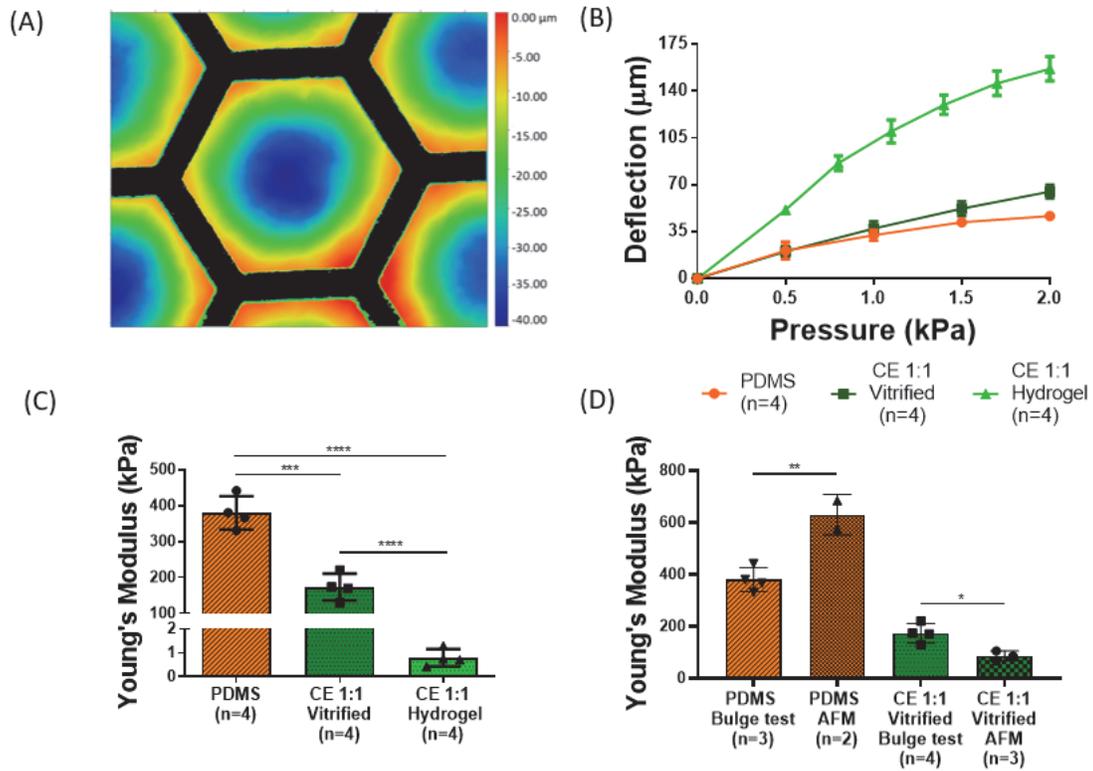


Figure 4.2 (Mechanical characterization of biological membranes): (A) Visualization of the vitrified CE-membrane deflection under a negative pressure of -0.5 kPa with an optical profiler. (B) Deflection of hydrogel and vitrified CE-membranes as a function of applied pressure. A 10 μm -thin PDMS membrane was used as a reference. (C) Young's modulus of membranes extrapolated from the pressure-deflection curves. (D) Comparison of Young's modulus obtained via AFM and bulge test.

Impact of CE ratio and gelation temperature on the mechanical properties of the membranes

The mechanical properties of the vitrified CE-membranes varied according to the composition of the solution pipetted onto the gold mesh. At lower collagen concentrations, the vitrified CE-membrane was softer, which resulted in larger deflection values. For example, at -1 kPa, the deflection was $83.2 \pm 8.9 \mu\text{m}$ at a 1:3 ratio and $37.5 \pm 5.2 \mu\text{m}$ at a 1:1 ratio of collagen to elastin

(Figure 4.3A). The resulting Young's modulus for the vitrified CE-membrane 1:3 ($E_{CE,v,1:3} = 74.9 \pm 42.7$ kPa) was approximately one-half of that for the 1:1 membrane ($E_{CE,v,1:1} = 173 \pm 37$ kPa) (Figure 4.3B). However, the protein ratio (1:1 or 1:3) had no significant effect on the mechanical properties of the hydrogel CE-membranes. Another factor affecting the stiffness of CE-membranes is the gelation temperature. The Young's modulus of the hydrogel CE-membrane produced at 37°C ($E_{CE,h,37^\circ C} = 0.79 \pm 0.36$ kPa) was approximately 2-fold lower than that of the membrane produced at 4°C ($E_{CE,h,4^\circ C} = 2.0 \pm 0.54$ kPa) (Figure 4.13).

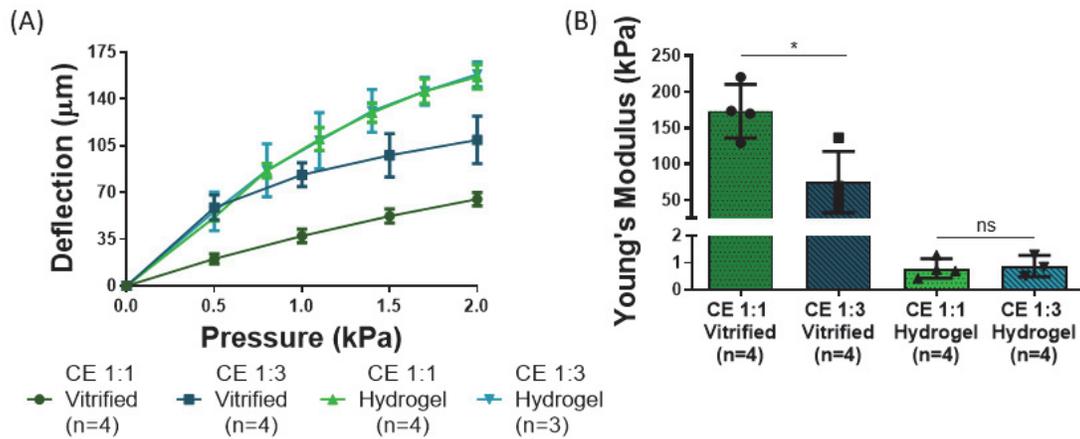


Figure 4.3 (Mechanical characterization of biological membranes as a function of protein ratio): (A) Pressure-deflection curves of vitrified and hydrogel CE-membranes with varying ratios of collagen to elastin. (B) Young's modulus extracted from pressure-deflection curves as a function of chemical composition.

Impact of stiffness on cell spreading

To determine the effect of substrate stiffness on cell spreading, human lung fibroblasts were cultured on PDMS-, vitrified CE-, and hydrogel CE-membranes. As shown in Figure 4.4A, the substrate type directly affected the shape and the cell surface characteristics. The fibroblasts on

the hydrogel CE-membrane have a circular shape characterized by a CSI of 0.62 ± 0.27 , whereas on PDMS and on the vitrified CE-membrane the cells are elongated ($CSI_{PDMS} = 0.21 \pm 0.13$ and $CSI_{V.CE} = 0.25 \pm 0.2$) (Figure 4.4B). Additionally, the surface area of fibroblasts grown on PDMS and vitrified CE-membranes was similar ($2153 \pm 1479 \mu\text{m}^2$ on PDMS and $1883 \pm 1041 \mu\text{m}^2$ on the vitrified CE-membrane), whereas that of cells grown on the hydrogel CE-membrane was approximately 4-fold smaller ($517 \pm 333 \mu\text{m}^2$) (Figure 4.4C). These data indicate that the stiffness of the surrounding ECM affects cell morphology.

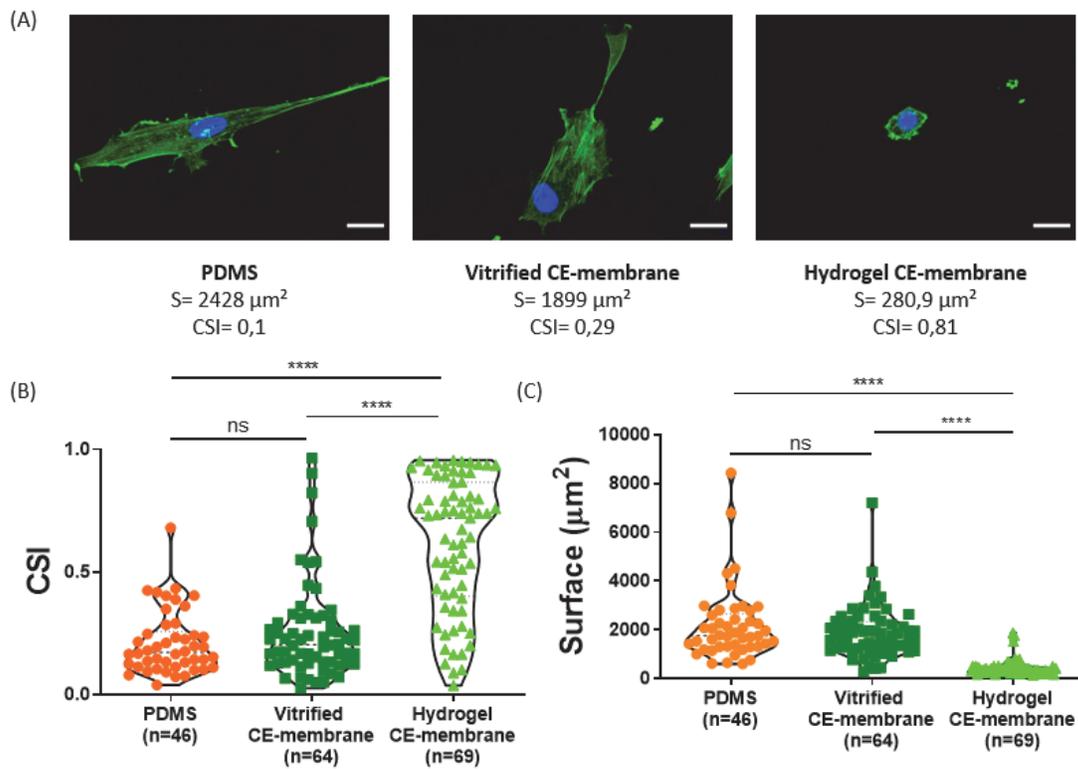


Figure 4.4 (Effect of the substrate stiffness on cell spreading): (A) HFL-1 on PDMS, CE 1:1 vitrified and CE 1:1 hydrogel membrane. Scale bar: 20 μm . (B) Cell Shape Index (CSI) and (C) cell surface of HFL-1 on PDMS, CE 1:1 vitrified, and CE 1:1 hydrogel membranes.

Discussion

The structure, stiffness, elasticity, and composition of the ECM are important for the maintenance of tissue homeostasis in health and disease.^{282,283} Therefore, reproducing ECM characteristics in advanced *in vitro* models is critical. In OOC devices, thin and flexible membranes made of PDMS (Sylgard 184) mimic the basal membrane and act as a substrate for cells.^{259,260} However, despite several advantages for cell culture, the composition and mechanical properties of PDMS differ from those of soft tissues. To achieve better simulation of physiological systems, biological vitrified²⁶⁶ and hydrogel^{284,285} membranes were developed and integrated into *in vitro* models. Collagen I has been used extensively in this context because of its capacity to form a stable gel rapidly at the physiological temperature. In this study, we report the mechanical characterization of biological membranes produced with or without vitrification. The simple fabrication process based on surface tension reported earlier²⁶⁷ was extended and used for hydrogel membranes enabling the reproduction of stiffnesses, with elastic moduli in the low kPa range, typically found in soft tissues. The membranes are composed of collagen I and elastin, two of the most abundant ECM proteins²⁸². The mechanical characterization of the membranes is carried out by AFM and compared with the bulge technique, which is reported here for the first time to the best of our knowledge.

The mechanical characterization of a cell-substrate, particularly the measurement of stiffness, is important because this parameter strongly affects cellular behavior.²⁸⁶ The AFM indentation

technique is a widely used method to characterize the stiffness of soft biological materials at the nanoscale. However, it only provides a local value of the stiffness, whereas the global stiffness of a tissue – here of a membrane – is often of interest. In addition, the fine-tuning of the indentation parameters is sample-specific and time-consuming²⁸⁷. In terms of instrumentation, the AFM method requires a specific setup for each biological material to be tested, particularly the cantilevers used. The bulge test is an alternative method for the determination of the average stiffness of freestanding membranes.²⁷⁵ In this study, we demonstrate that this non-destructive technique is a valuable tool to determine the Young's modulus of thin and soft membranes, in particular those with low stiffness (in the kPa range). The Young's modulus determined for the collagen-elastin hydrogel membrane (0.79 ± 0.36 kPa) is in the range of the values found in the literature for collagen based hydrogel (about 0.5-2.4 kPa^{284,288,289,290} of similar concentration (about 3 mg/mL)). Very few studies have estimated the Young's modulus of reswollen vitrified collagen-based membrane. Huh *et al.* reported a value of 660 kPa for a collagen vitrified membrane, which decreased to 429 kPa when mixed with Matrigel. In the present case, elastin made it possible to increase the flexibility of the biological membrane and reduced its Young's modulus (173 ± 37 kPa). Both methods, the bulge test and the AFM, have their own limitations and operating challenges. On one hand, Young's moduli obtained with the bulge test depend on the accuracy of the membrane thickness measurement, often difficult to determine for hydrogel membranes. The accurate estimation of the deflection amplitude is an additional challenge, due to the not well defined membrane-liquid interface. On the other hand, the assessment of mechanical properties of thin, soft and suspended membrane is challenging with the AFM technique. In fact, the interaction

of the tip with the membrane leads to local deformations that are linked to the mechanical properties of the material but also induces the membrane to deflect, creating a measurement artifact. Complex set-ups^{291,292} are needed to circumvent this problem. In the present case, thick layers of the respective materials were produced on glass slides and measured for their stiffness. The Young's moduli obtained using the bulge test were in the same order of magnitude than those determined by AFM.

The properties of collagen scaffolds, especially their mechanical and transport properties, depend on several parameters, such as the protein source and concentration, gelation pH, and temperature, among others. Each of these factors can dramatically affect the mechanical properties of membranes.²⁹³ In this study, we identified protein concentration as a key parameter affecting the Young's modulus of membranes. The flexibility of the vitrified CE-membrane was directly dependent on the ratio between collagen and elastin, and an increase in elastin concentration over collagen led to larger deflections. However, decreasing the concentration of collagen could prevent gelation and the complete formation of hydrogel CE-membranes. Another parameter affecting the mechanical properties of biological membranes is gelation temperature. The self-assembly process occurs at a faster rate at higher temperatures, which can reduce the diameter of fibrils.^{294,295,296} In this study, lower gelation temperatures (4°C vs. 37°C in the normal procedure) increased the gelation time and potentially the size of the fibers. That may explain the difference in Young's modulus for the hydrogel CE-membrane obtained at 4°C and at 37°C. These results suggest that membranes with a wide range of stiffness values (i.e., 0.8–200 kPa) can be generated by modifying the fabrication procedure

and certain parameters such as protein concentration and gelation temperature, thus reproducing the stiffness of healthy tissues such as the brain (0.5–1 kPa)²⁹⁷ lung (1–5 kPa)²⁹⁸, and skin (50 kPa)²⁹⁹, as well as fibrotic tissues³⁰⁰

The mechanical properties of the surrounding substrate greatly influence cell morphology^{301,302}, proliferation,³⁰³ adhesion,³⁰⁴ migration, migration,³⁰⁵ and differentiation.^{306,307} In particular, the stiffness of the ECM critically determines cell morphology and specifically cell spreading. We observed that fibroblasts cultured on stiff membranes (PDMS and CE-vitrified) have a significantly larger surface and lower CSI than those grown on soft materials (hydrogel CE-membrane), which is in agreement with similar studies.^{256,308} However, the surface area did not differ between substrates exposed to 200 kPa and those exposed to 400 kPa. Unlike the process for PDMS membranes, the biological membranes did not require any preliminary treatment for cell culture.

Conclusion

This study describes the mechanical characterization of new flexible biological membranes using the bulge test method compared with AFM. The results obtained with the non-destructive bulge technique were in the same order of magnitude to those obtained by AFM. The results showed that the bulge test is a robust and reproducible technique to determine the Young's modulus of thin biological suspended membranes. Stiffnesses as low as 1 kPa could be assessed in an uncomplicated manner. The membranes presented in this study can be modified to

reproduce the physiological or pathophysiological microenvironments of various tissues. In addition, these biological membranes fabricated out of natural materials are not subject to the limitations of synthetic materials regarding composition and functionalization. However, in contrast to synthetic membranes, such as PDMS, the biochemical and mechanical properties of the CE-membranes are coupled, which may present limitations, as the effects of these properties cannot be investigated separately. Nevertheless, biological membranes present other advantages, such as a simple production process. These membranes can be stored for long periods of time (at least 2 weeks) without significant effects on stiffness. In summary, biological membranes provide the organs-on-chip and the tissue engineering communities with a powerful tool that can be tuned at will to reproduce the *in vivo* ECM mechanical and biochemical properties among others. Their integration into organs-on-chip devices has already started as reported by several groups^{266,268,280, 285}. There is little doubt that the years to come will see an increase in the development of organs-on-chip with integrated biological, stretchable or not, membranes exposed to mechanical forces, such as flow or mechanical stress.

Acknowledgments

The authors thank the Swiss National Science Foundation for its financial support (project number: 185365) as well as the Microscopy Imaging Facility of the University of Bern (MIC) for its assistance. B. Putz acknowledges funding from the EMPA POSTDOCS-II program, in the frame of the EU-H2020 Marie Skłodowska-Curie grant (Nr. 754364). GEF acknowledges funding from H2020 - UE Framework Programme for Research & Innovation (2014-2020);

ERC-2017-CoG; InCell; Project number 773091. VC acknowledges funding from the EU-H2020 Marie Skłodowska-Curie grant (Nr. 754354).

Supplementary Figures

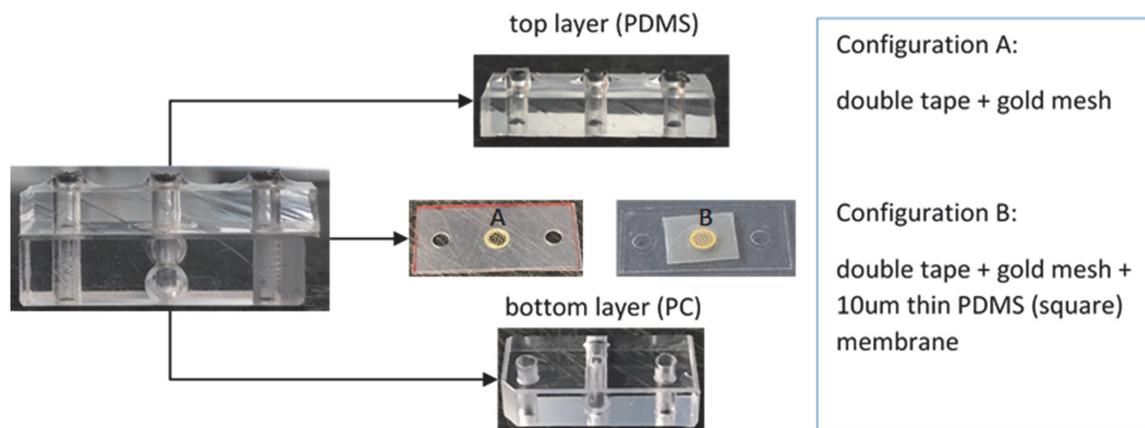


Figure 4.5 (Chip design):

The chip was made of a PDMS top layer and a polycarbonate (PC) bottom layer, between which either A) a collagen-elastin membrane or B) a PDMS membrane supported by a gold mesh was sandwiched. The gold mesh was bonded to the PDMS top part with a double tape (Arcare 90445-5, Adhesives Research, Glen Mark, PA, USA) punched with 2mm in diameter holes.

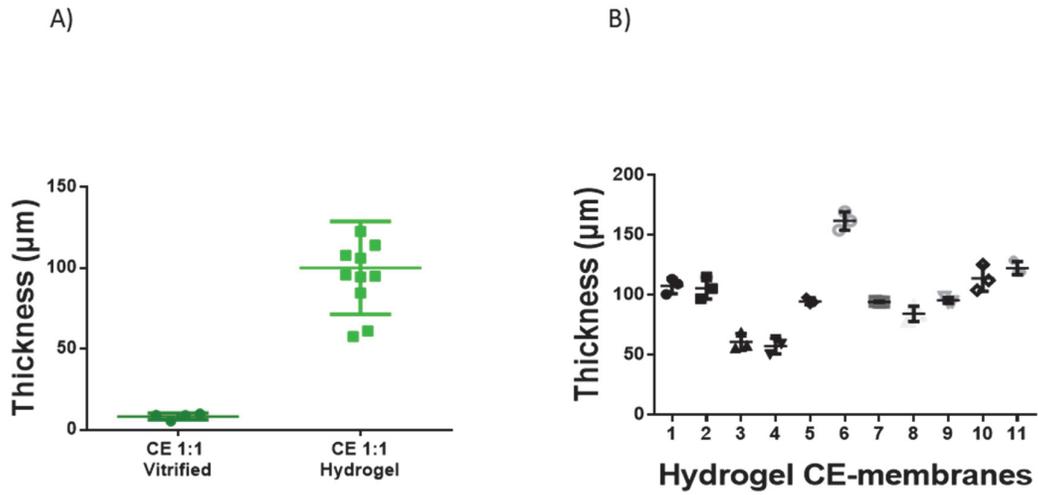


Figure 4.6 (Thickness of the vitrified and hydrogel-based biological membranes):

The volume of the collagen-elastin solution pipetted on the gold mesh is $32\mu\text{l}$ for both membranes ($1.6\ \mu\text{L}/\text{cm}^2$). In contrast to the hydrogel membrane, the vitrified membrane is dried following the dispensing of the CE solution. This influences the final thickness of the membrane (Figure 4.6A). For each hydrogel CE-membrane, 3 measurements were taken in the central hexagon. The thickness variation across the hexagon was below 12% (Figure 4.6B).

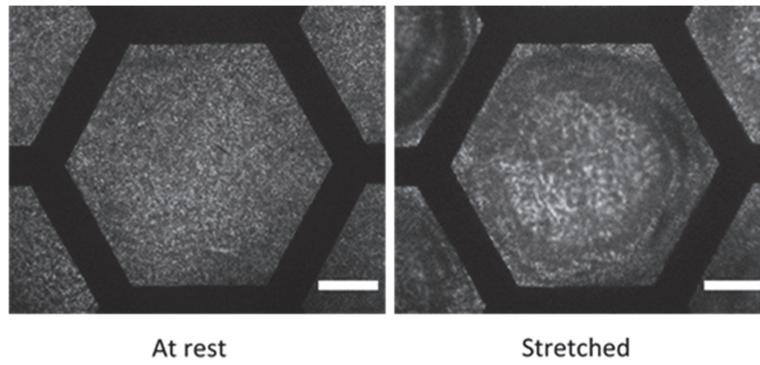


Figure 4.7 (Representative image of a hydrogel CE-membrane at rest and after exposure to a negative pressure of -1.1 kPa):

The images were acquired by AxioPlan2 Zeiss Microscope via reflective light. Scale bar: 100 μm .

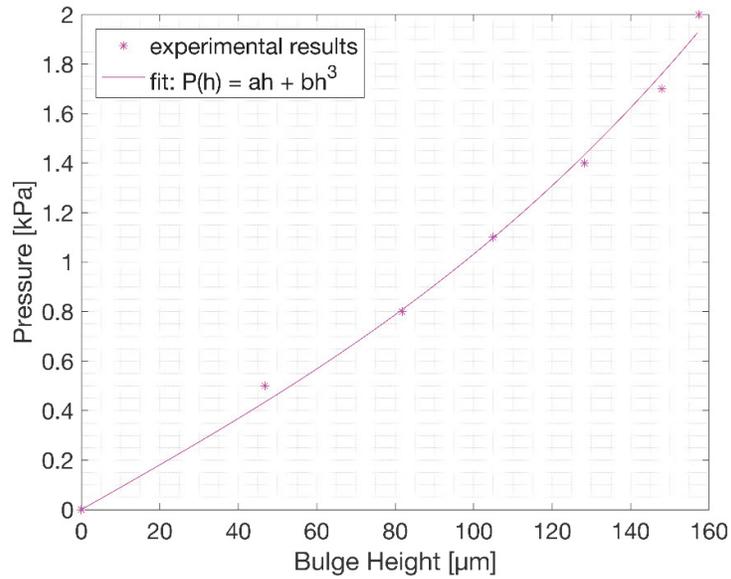


Figure 4.8 (Determination of the Young's modulus based on the pressure-deflection curve of the hydrogel CE-membrane):

The fitting curve was based on the bulge equation ($P = ah + bh^3$), with P and h , being the pressure and the bulge height, and a and b two constants. The least-squares method (MATLAB) was used to fit the experimental pressure-deflection data, resulting in a coefficient of determination R^2 (here $R^2=0.9953$). The Young's modulus E was then extracted from the constant b from the fitting curve (here $E_{\text{hydrogel}} = 0.7 \text{ kPa}$).

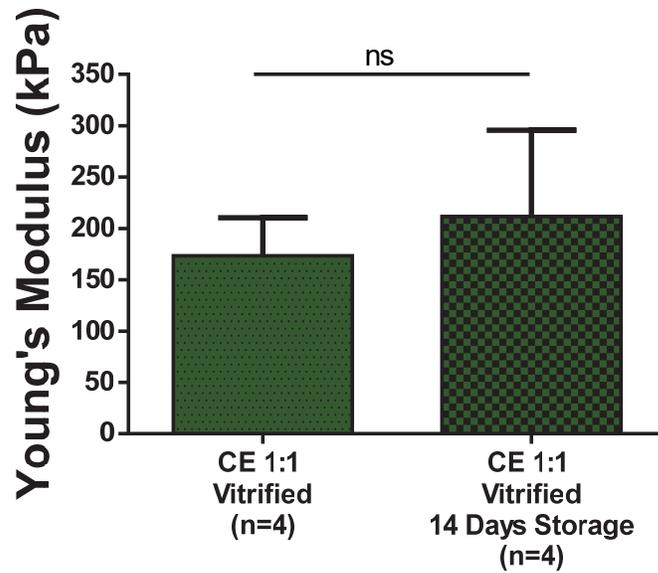


Figure 4.9 (Impact of the storage of the vitrified CE-membrane on its mechanical properties):

The vitrified CE-membrane has been dried for 48h at room temperature and then stored for two weeks. No significant difference of the Young's modulus has been observed between membranes tested before and after storage (173 ± 37 kPa after the production versus 212 ± 84 kPa after two weeks storage).

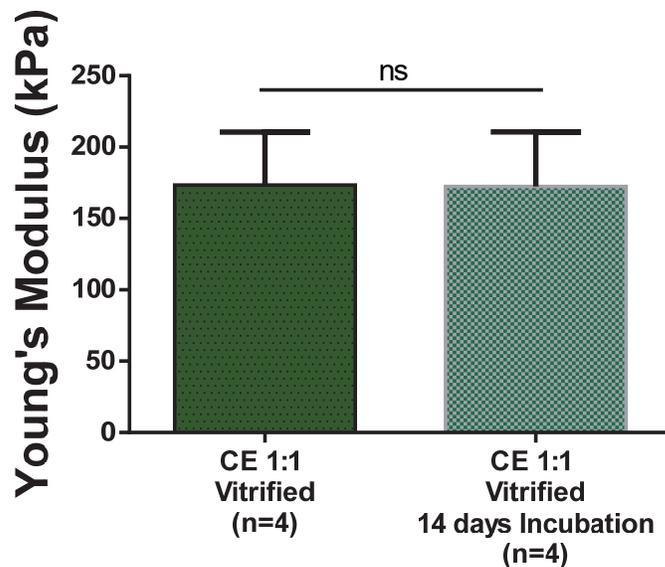


Figure 4.10 (Impact of a 2-weeks immersion in physiological medium on the mechanical properties of the vitrified CE-membrane):

To simulate the impact on the stiffness of a long-term cell culture, the vitrified CE-membrane was immersed during two weeks in physiological medium. The vitrified CE-membrane has been rehydrated with cell culture media, then incubated for two weeks. No significant difference of the Young's modulus has been observed between membranes tested before and after being immersed in physiological medium for two weeks (173 ± 37) kPa after the production versus 172 ± 38 kPa after two weeks immersion).

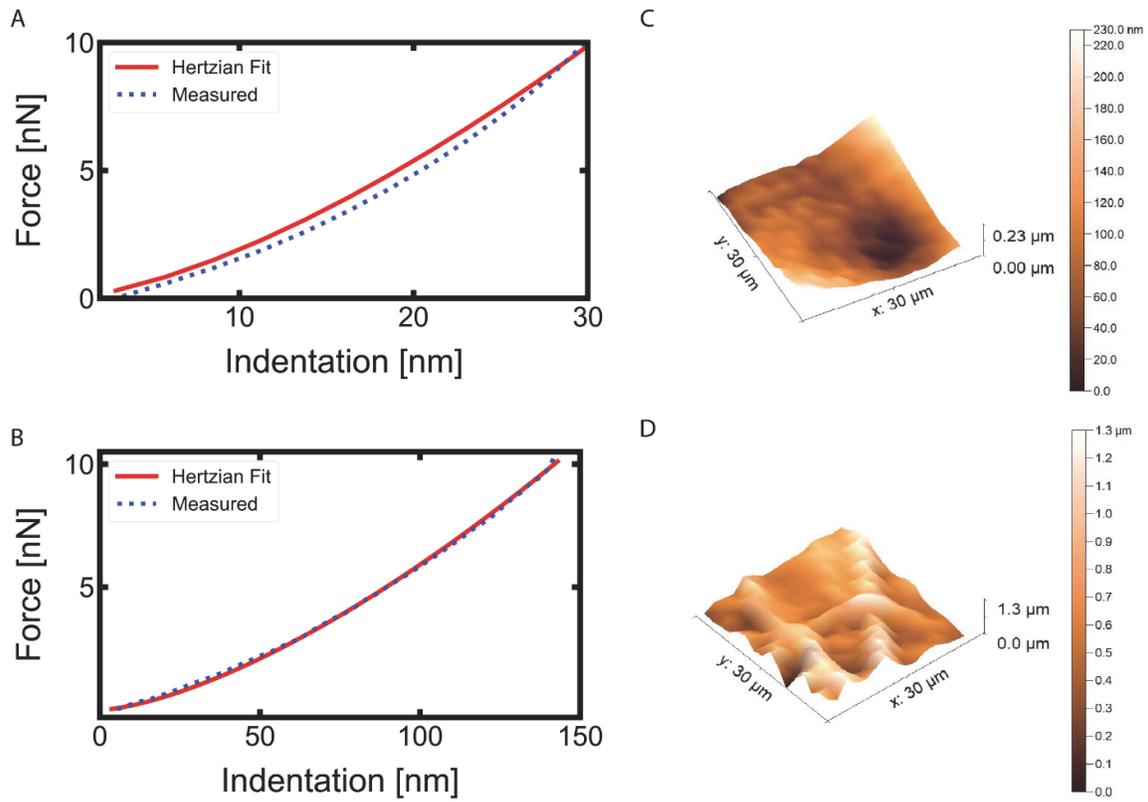


Figure 4.11 (Force-volume image and force curves obtained by AFM):

The modulus of the vitrified CE membrane and of the PDMS membrane were measured using AFM. The figure A and B are the force-indentation curves of PDMS and the CE membrane respectively, whereas figures C and D are their corresponding force-volume images

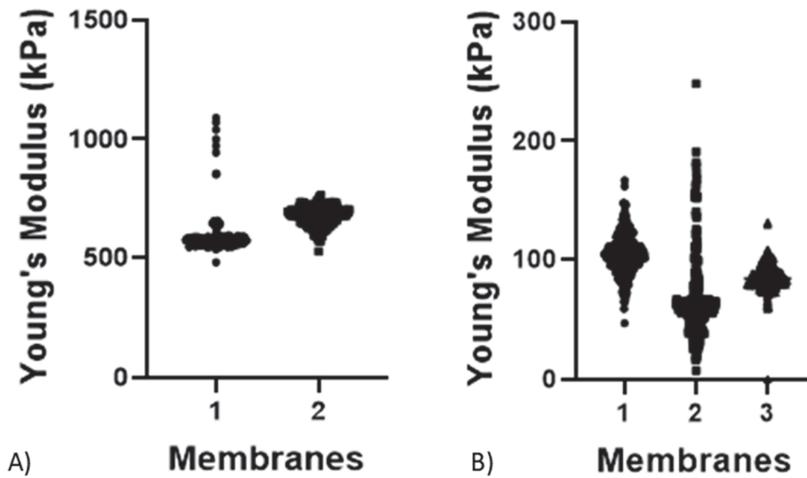


Figure 4.12 (Young Modulus variance measured by AFM):

The AFM method provides the value of the local stiffness. A minimum of 256 measurements was carried out to quantify the stiffness of the membrane. The distribution of the measurements obtained for the PDMS membrane and vitrified CE-membrane are indicated in figures A and B, respectively. The coefficient of variation is smaller than 13% for the PDMS membrane is larger than 12% for the CE-membrane.

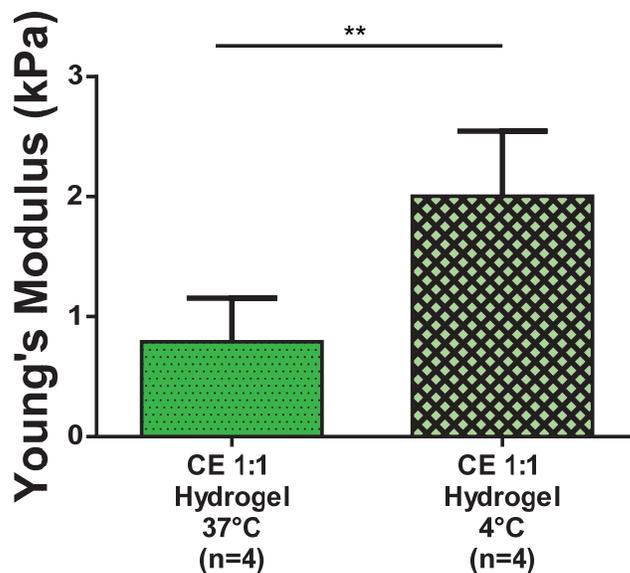


Figure 4.13 (Membrane production: Impact of the gelation temperature on the Young's modulus during the production of the hydrogel CE-membrane):

Following the dispensing of the CE-solution on the gold mesh, hydrogel membranes were produced with different gelation temperatures. The hydrogel solution of the first set of membranes was crosslinked at 37°C for 1h, whereas the second set of membranes had a lower gelation temperature (4°C) and longer incubation time (overnight). At lower gelation temperature, the resulted membrane presented a significantly higher stiffness than at 37°C (0.79 ± 0.36 kPa at 37°C against 2.0 ± 0.54 kPa at 4°C).

5. AFM imaging of Clathrin Mediated Endocytosis

5.1 Introduction

This chapter presents preliminary results of our efforts to image clathrin self-assembly in a more biologically relevant system, ideally inside living cells. The first step to observing clathrin self-assembly in cells is to image pre-formed clathrin coated pits in unroofed cells. Further work should aim to imaging these unroofed cells in a dynamic fashion to potentially observe maturation and growth of these structures. Once technology to image with AFMs inside living cells matures³⁰⁹ it might become possible to observe this process by AFM *in vivo*.

5.1.1 Clathrin mediated endocytosis

The specific process we wish to image is clathrin-mediated endocytosis: a well-known method by which cells selectively absorb material (such as metabolites, hormones, proteins, or viruses). A simplified diagram of the process is shown in Figure 5.1a. In brief, a cargo ligand will bind to its receptor on the outer surface of a cell membrane, which will recruit adaptor proteins and clathrin triskelia (composed of three clathrin heavy chains and three clathrin light chains) to the site.

Once the coat is assembled, actin filaments polymerize near the forming vesicle with several regulatory components, including the Wiskott–Aldrich syndrome protein (WASP) family proteins, which play a major role in activating actin filament nucleation (by actin-related protein complexes), myosin motor proteins and dynamin. Since the binding energy is insufficient to finalize the process, the vesicle will eventually be cleaved off with assistance of

scission-related proteins, dynamin, and BAR (Bin, amphiphysin and Rvs) domain proteins such as amphiphysins and endophilins. This step requires a large amount of GTPase dynamin to assemble the neck of the clathrin pit, and GTP for further constriction and membrane fission. Two models are proposed for this constriction. In the first, slower model (taking a few seconds) dynamin binds to GTP and creates a tight helical constriction around the neck, leading to hemifission. In the second, faster model (taking around 100 ms), dynamin would assemble around the neck in a looser form, and GTP hydrolysis would create the energy leading to tighter constriction and hemifission. Endocytic events are usually spatially defined, meaning they occur on certain parts of the cell membrane, but can occasionally appear to be initiated at random sites (possibly when adaptor proteins collide with the plasma membrane by stochastic collision).³¹⁰

In some occasions, rather than forming a pit, the clathrin triskelia will create a plaque at the site of endocytosis, with a similarly hexagonal pattern, but larger surface area (up to 500nm) and longer duration (up to 15 minutes).³¹¹ This makes it more convenient for imaging with slower, large range AFM methods, such as ORT. There remains some uncertainty in how the two variations of the process are related, particularly since they are not both present in every cell type.^{310,312,313} It has been found that appearance of plaques may be more likely when there is increased tension on the cell membrane³¹⁴, and may also signify stronger adhesion of the cell.³¹² Cholesterol depletion, for example with Methyl- β -Cyclodextrin (M β CD)³¹⁵, has been shown to create flat clathrin lattices even in cells when these are uncommon.^{316,317} The stability of the structure can be determined, for example, by the proportion of hexagons present in the plaque.

5.1.2 Imaging of unroofed cells

Since it was first observed by electro microscopy in 1975³¹⁸, clathrin and its vesicles have become a popular topic of study, eventually also with AFM.³¹⁹ Since it is otherwise difficult to locate the vesicles on a cell membrane, combining fluorescent imaging with AFM provided a solution.³²⁰

AFM imaging of clathrin pits on the interior side of the membrane was possible after the unroofing of the cells, and light fixation using paraformaldehyde and glutaraldehyde for better crosslinking. Unroofing, or removal of the top membrane and cytoplasmic components of a cell, can be achieved in several different ways. For example, the sandwich method involves pressing the cell between two surfaces, usually poly-L-lysine (PLL) coated glass and removing the top with the membrane adhered to it.^{321,322} This method is relatively simple and requires less preparation, but results in more undesirable residue on the sample. Alternatively, it is possible to use ultrasonication, where the cells are briefly exposed to a low-power ultrasonic current through a probe tilted at 45 degrees placed a few millimeters from the adhered cells in KHMgE buffer. The buffer is magnesium rather than calcium based to adapt to the intracellular environment, and includes protease inhibitors such as AEBSF (4-(2-aminoethyl) benzenesulfonyl fluoride hydrochloride) and EGTA (ethylene glycol tetraacetic acid), as well as DTT (dithiothreitol). PLL can be added for 10 seconds prior to ultrasonication to improve adhesion. Immediately after a few seconds of ultrasonication, the cells are rinsed with the same buffer and lightly fixed with 0.5-2% paraformaldehyde and glutaraldehyde.^{323,324} Although this method requires a specific setup and longer preparation, it reveals very clean samples.

5.2 Methods

5.2.1 Unroofing

For cholesterol-depleted samples, cells were incubated in M β CD medium of 30 min prior to unroofing.

KHMgE buffer is prepared in advance and is composed of 30 mM HEPES, at pH 7.4, 1 mM EGTA, 3 mM MgCl₂, 70 mM KCl, and 1 mM DTT. 0.1 mM AEBSF is added just before the start of the unroofing.

The ultrasonic homogenizer used in this protocol is the Model 150VT³²⁵ from BioLogics, Inc., with a 4 mm titanium stepped micro tip.

The unroofing protocol is based on³²⁶. Cells on coverslips were first rinsed with PBS. The coverslips were placed for 10 s in PLL solution (0.5 mg/mL PLL dissolved in PBS), and washed three times (a few seconds each) in hypotonic KHMgE (one part KHMgE with two parts of distilled water). With the resulting swelling, the cells burst easily with ultrasonication. Immediately after washing in hypotonic solution, the cells were ultrasonicated with a probe (5 minimum power pulses of 1 second each) in isotonic KHMgE. Unroofed cells were rinsed in fresh KHMgE buffer and fixed for 10 min with 1% glutaraldehyde and 1% paraformaldehyde in KHMgE buffer. Fixed samples were washed twice with KHMgE buffer and used for AFM measurements.

5.2.2 AFM imaging

AFM images were taken with a modified setup of the Bruker Dimension Icon³²⁷, where an inverted microscope is added to allow better visualization of biosamples prior to imaging. This

allowed us to locate the clathrin-dense areas based on the RFP-labelled clathrin light chain A (CLCA) and GFP-labelled dynamin 2 (DYN-2). AFM images were taken with Scanasyt Fluid+ cantilevers³²⁸ at 1 Hz line rate and 2 kHz ORT rate in PeakForce mode keeping the setpoint below 500 pN. All images were processed in Gwyddion³²⁹.

5.3 Results

Using fluorescence to locate areas of concentrated endocytic activity, we were able to image a large range of the unroofed cell membrane. An example of this overlay is shown in Figure 5.1b.

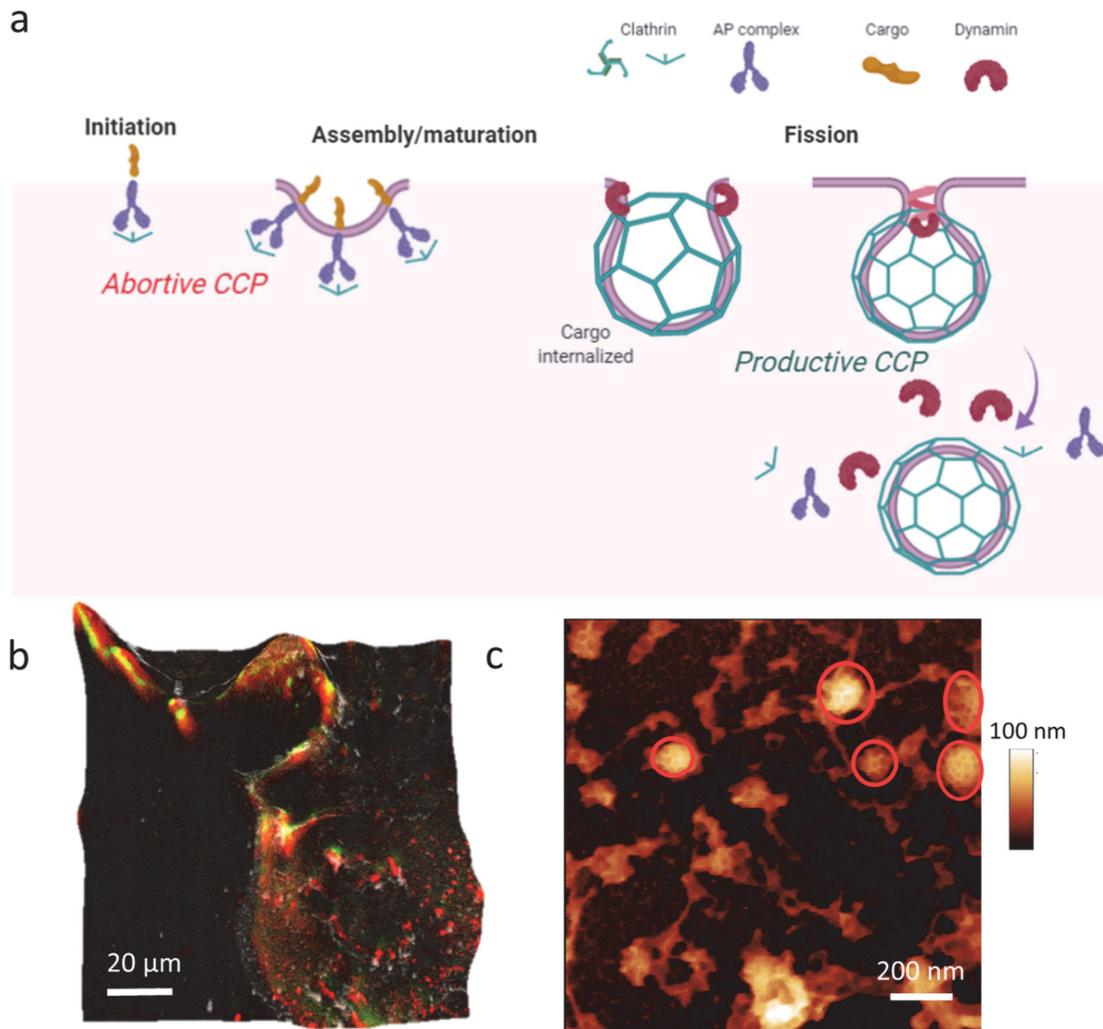


Figure 5.1 (Imaging clathrin on unroofed fixed cells): a) A simplified diagram of a cell membrane taking up material via clathrin mediated endocytosis, showing the main proteins involved (clathrin, the AP complex and dynamin) The diagram also show the stage at which abortive CCP is still possible. The diagram was created with [BioRender.com](https://www.biorender.com). b) Overlay of AFM and fluorescence for large area of an unroofed and fixed SKMEL-2 cell. RFP-labelled CLC and GFP-labelled DYN-2 are visible as red and green intensity areas respectively. The AFM image was obtained in off-resonance tapping mode at 1 Hz line rate. c) Clathrin pits (circled in red) on an unroofed and fixed SKMEL-2 cell, imaged in off-resonance tapping mode at 1 Hz line rate. Notably, most clathrin structures are pits when the membrane is not modified.

When the unroofed cell membrane is fixed, clathrin vesicles are clearly visible, as shown in Figure 5.1c. However, without fixing the membrane, it is difficult to image the membrane at sufficient speed and for sufficient duration. The time of clathrin-mediated endocytosis is usually in the scale of seconds,³³⁰ which is a difficult frame rate to achieve with the current setup. An example of an attempt to image the same cell type without fixing the membrane is shown in Figure 5.2a.

Cholesterol depletion stiffens the membrane³³⁰, changing the duration and shape of endocytic structures.³³¹ This is predominantly due to the role of lipids and cholesterol in membrane trafficking³¹⁷, where the presence of specific sterols is crucial for membrane bending and ultrastructure³¹⁶. An example of this change in structure is shown in Figure 5.2b, where we can observe flatter clathrin structured circled in red. These are often composed primarily of hexagons and have a much lower height³³².

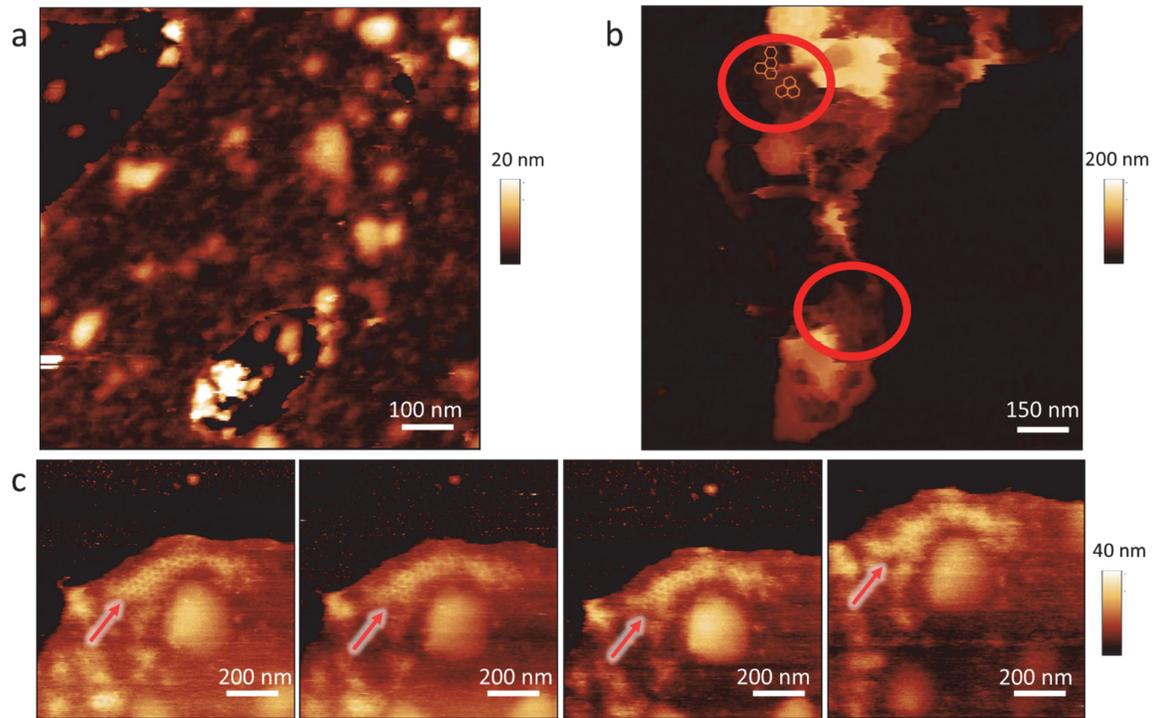


Figure 5.2 (Effects of cholesterol depletion on imaging clathrin on unroofed cells): a) Unroofed non-fixed SKMEL-2 cell imaged in off-resonance tapping mode at 1 Hz line rate. Structures on the membrane are distorted or removed (the image gives a representative example of several sections that were imaged, where there are no resolvable features visible on the membrane) possibly due to the force of the AFM tip and the duration required for imaging. b) Clathrin structures imaged on an M β CD-treated unroofed and fixed SKMEL-2 cell. The sample was imaged in off-resonance tapping mode at 1 Hz line rate. Flatter structures with a hexagonal pattern are visible and marked in red. c) Clathrin plaque (indicated with red arrow) imaged on an M β CD-treated unroofed (not fixed) SKMEL-2 cell. The sample was imaged in off-resonance tapping mode at 2 Hz line rate.

Since cholesterol depletion slows the process of endocytosis to the timescale of minutes³¹⁷, it was used to facilitate the imaging of non-fixed clathrin structures on unroofed SKMEL cells, as shown in Figure 5.2c. This was done in conjunction with other methods used to preserve the

cell membrane without using overly destructive modifications, such as protease inhibitors (particularly 4-(2-Aminoethyl) Benzenesulfonyl Fluoride (AEBSF) and other water-soluble protease inhibitor cocktails³³³) and transferring the sample on ice between the steps of taking it from the incubator until imaging.

5.4 Discussion and future work

This preliminary work shows that we can reproduce the imaging of clathrin pits with our AFM setup. Unlike with EM, we do not need to do any aggressive modifications to the sample as required in EM³²⁴. This makes AFM a potential candidate for imaging unroofed cells without the necessity of fixing them, allowing us to image a semi in-vivo sample where clathrin mediated endocytosis is still active and can potentially be imaged with dynamics. However, we are still limited by the efficiency at which the imaging can be done. This is mostly due to the limits of imaging speed that can be reached with AFM setups that are appropriate for imaging this type of complex biosample at an appropriate range. We can slow the process using, for example, protease inhibitors, cooling, or cholesterol depletion. However, even if the process is slowed and stabilized enough for imaging to be possible, the modifications that were done to the cell before or after unroofing will have an effect on the CME process that may render the data obtained unreliable.

A proposed solution would be to continue to upgrade a large-range PORT-based AFM setups such as DriveAFM to optimize it for imaging this type of sample, since the eventual purpose of PORT-based systems is to improve control over forces used on the sample while maintaining

speed.³³⁴ While preliminary data was obtained with a prototype version of this setup, improvements need to be made in terms of noise elimination and speed in order to reach appropriate imaging quality. When it is possible to obtain reliable data of non-fixed cells, it would be interesting to use a combination of fluorescence and AFM to track the proteins responsible for the different stages of endocytosis and potential defects.

With improved speed and range, imaging of clathrin on unroofed cells or even in-vivo will become more efficient. However, slowing the endocytic process with cholesterol depletion may still be useful in studies of molecular interactions in CME. For example, we hope to investigate the role of HSC70 and Auxilin,³³⁵⁻³³⁸ usually associated with uncoating of the internalized clathrin vesicles, in the initial steps of endocytosis. Clathrin exchange will still occur in cells depleted of cholesterol,³³⁹ and HSC70 is responsible for chaperoning clathrin to the membrane³⁴⁰. It would therefore be interesting to observe the effects of these molecules on the shaping of vesicles on the membrane.

While the current work on the use of cholesterol depletion to image clathrin mediated endocytosis on unroofed cells without fixing them is not scientifically conclusive, it provides a starting point for future progress in obtaining data on the structure of clathrin structures with minimal damage to the sample.

6. Discussion and future work

6.1 Contributions of the thesis and remaining challenges

6.1.1 Setting Parameters in PORT

The first part of the thesis discusses the parameters used in PORT imaging. There is a need for controlled tip-sample interaction forces, which, thus far, have not been investigated for dynamic imaging in PORT. Work has already been done in measuring the dynamic force of individual taps in PORT imaging⁴², but its effects while imaging simplified sample (such as 3PS) has not been investigated. We observed the effects of changing PORT rate, scan rate, as well as changing the laser power and PORT amplitude on the sample. The precise forces were not defined, but we were able to see the difference on the imaging quality and sample destruction. While there are force estimation models available for tapping mode^{341,342}, these are very limited for ORT, and not yet done for PORT. Some approximations can be made based on dynamic impact force data⁴², however this does not account for the overall forces during imaging. From experimental approximations, the dynamic forces are still significant (in the nN scale). While tapping mode forces can be reduced by limiting the tapping amplitude³⁴³, this is currently more difficult to do with PORT, as there are additional noise sources that have not yet been resolved, which mostly require mechanical and electrical component optimization. The work presented shows that increasing the amplitude of PORT can lead to sample damage, which we attribute to a combination of force and temperature resulting from the increased laser power. The effects of increasing laser power have been investigated in other imaging modes, and should be adapted for bioimaging.³⁴⁴ While effects of laser power on temperature can be modelled using appropriate software³⁴⁵, this is not necessarily representative for the

temperature effects on the sample. Experimentally, this can be done, for example, by observing the phase transition of lipid bilayers from ripple to fluid phase.³⁴⁶ It would also be possible to observe a range of temperature points using different lipid blends with a variety of melting points.^{347–349}

Continuous work is being done to improve the HS-AFM setup in general. This means it should be possible to scan complete images at “video rate” (several frames per second) with sufficient resolution for the observed phenomena, without causing damage to the sample. Currently, one focus is on the efficiency of the cantilevers. By developing shorter cantilevers with higher actuation efficiency, we can increase PORT rate and imaging speed without the need of increasing laser power. This is due to the heat transfer efficiency of shorter cantilevers, but can also be improved by increasing the absorbency of the cantilever coating material.^{41,350} This does not come without related issues. For example, the increased cantilever sensitivity requires higher sensitivity of the photodiode detector for sufficient SNR. The detection bandwidth of the photodiode detector is currently in the magnitude of 10 MHz.³⁵¹ The lack of linearity in the photothermal drive laser itself can also contribute to instabilities.

Tapping mode and related modes are currently still the most popular for use in HS-AFM. PORT offers a high-speed improvement to other excitation methods used in ORT, since only the cantilever requires excitation, although this is still limited to below the resonance frequency. In scanner-driven off-resonance tapping modes, the modulation frequency is kept below the scanner frequency (in most cases a few kHz, but in some cases up to 31.5 kHz³⁵²) to prevent distortions.³⁵³ Even in PORT, however, the feedback can be distorted by artificial factors, and we can have issues with the error in spring constant calibration or curve fitting. By resolving

these issues and adding adequate improvements (data acquisition speed, faster control systems), the improved control of force offered by PORT makes it a good candidate for integration with other imaging methods, such as superresolution or TIRF microscopy.

6.1.2 Use of PORT for imaging self assembly

Unlike with end-point measurements, where the samples are dried at specific time points of assembly prior to imaging,^{354,355} HS-AFM of dynamic self-assembly allows us to observe the error correction real time, and observe a constant rate of change rather than averaged datasets. Not only is this more time-efficient, but it also allows us to observe error corrections and formations that are a result of previous events. Unfortunately, this does not come without challenges. The increase in speed comes at the cost of range¹⁴⁷, which makes it difficult to observe events at a larger scale (in the case of the setup used in this work, 1.6 μm). Additionally, the output is often very large datasets that need to be batch-processed, which often requires a script specific to the type of molecule.³⁵⁶

In this thesis, the effects of structural flexibility and binding strength on self-assembly are investigated using a simplified 3PS system. The difference in stability of resulting crystals is observed through HS-AFM imaging as well as simulations. Structural variations in individual molecules and their effects on self-assembly are less commonly investigated, as it is difficult to observe at high speed in complex systems. By observing these effects in a simplified DNA 3PS system, we can attempt to transfer the observations to biologically relevant examples.

In hexagonal monomer lattice structures found in nature, formation of other polygons disturb the stability, which is also the case in clathrin.³⁵⁷ This can give further insight on how details

such as binding affinity and defects in arm structure can affect the assembly process. If we were to observe clathrin directly, this is complex due to the additional components required for proper interaction and doesn't allow us to focus on the structural effects. An attempt to image clathrin triskelia assembling on mica with HS-PORT-AFM is shown in Figure 6.1.

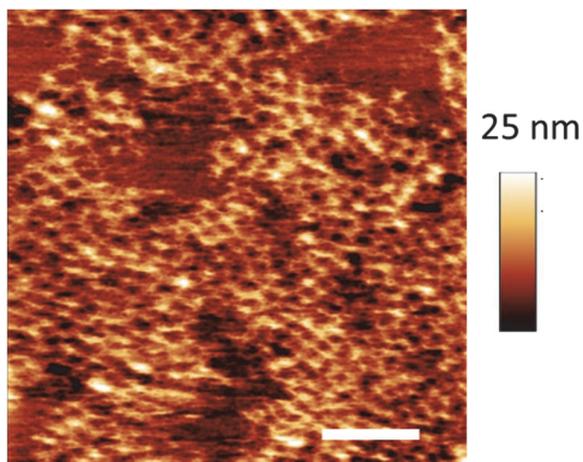


Figure 6.1 (Clathrin triskelia covering a mica surface imaged on the high-speed AFM): Scale bar 200 nm

In future work, we hope to modify the branches of the 3PS to include a bend, mimicking the structure of clathrin, by bending the arms. Preliminary work has already been done on observing in-vitro clathrin assembly, but the added complexity makes it difficult to reliably image at sufficient speed.

6.1.3 Imaging of self-assembling structures in-vivo membrane

One of the main challenges of AFM imaging on unroofed cell membranes is the complexity of contents that contribute to the degradation of the molecules of interest. In spite of the use of

enzyme inhibitors and proper rinsing^{326,333}, it is difficult to image structures of interest for a sufficient time when the sample isn't fixed. Since the structures are often not fully attached to the membrane (e.g. a semi-formed clathrin bud), imaging forces may displace them and tamper with their formation.

Current examples of large-range HS-AFM have already made steps towards overcoming challenges such as reducing noise and preventing mechanical instabilities, an improved scanner resonance frequency.³⁵⁸ Some attempts of large-range bio-imaging have already been published, but are still done at frame rates slower than many significant biological processes³⁵⁹. A HS-AFM system with adequate balance between speed, scan range and tip-sample force control for cell-scale imaging is not yet available. Our group is working towards developing a large-range PORT-based AFM that should eventually enable high-speed imaging. Ideally, this would be combined with super-resolution imaging techniques, which can also reach sub-second imaging rates (e.g. STORM)³⁶⁰. In order to achieve this, both techniques need to have reached sufficient optimization, and then be aligned to a precision of at least 10 nm or below.³⁶¹ Progress in PORT-based AFM setups for large range images should also enable combined fluorescent-AFM imaging of live samples in real time. NanosurfTM, for example, uses Viewport to navigate the sample with a combination of fluorescent imaging and AFM simultaneously.³⁶² This improves the efficiency of locating regions dense with the structures of interest.

6.2 Closing Statement

Despite its potential, AFM is not without challenges. Imaging artifacts, improper sample preparation, and issues with any of the components of the AFM can influence the quality of

acquired data, demanding careful experimental design and data interpretation. Furthermore, the pursuit of ever-increasing resolution and accuracy drives ongoing advancements in AFM instrumentation and data analysis techniques. The use of AFM for bioengineering application continues to evolve as we add to the development of individual components. By continuous upgrade of the current PORT-HS-AFM, as well as the tip-scanning PORT setup, we may eventually move towards imaging larger and more complex biological samples. This research work sets an example of the adaptability of the open source HS-PORT AFM in the realm of bioimaging.

Appendix

Supplementary Information to Chapter 3

The following appendix is the supplementary material to Chapter 3 and includes supplementary information referred to in the main body of the thesis. My contribution involves the final steps of sample preparation for high speed imaging, as well as the high speed imaging, video processing and analysis.

Extended Methods

Oligonucleotides.

All DNA tiles designed in this study are based on the original 3-point-star (3PS) motif³⁶³. The modifications on the DNA sequences of the 3PS motif were made following the principles presented by Seeman¹³³: All 4 nucleotide-long subsequences of individual DNA strands are (1) unique, (2) not self-complementary (e.g. TGCA) and (3) includes both purine and pyrimidine. The same rule applies for the 4 nt-long subsequences that are on a continuous DNA duplex but span a junction.

All oligonucleotides used in this study were either bought from Integrated DNA Technologies, Inc. or synthesized in house on OligoMaker (TAG Copenhagen) following standard synthesis protocols. The sequences are listed in Table 7.1.

Purification of DNA tiles.

Preparation methods of individual DNA tiles can be found in the main text Materials and Methods. The annealed product was loaded on a 3% agarose (Sigma) gel and the gel was run

at 60 V for 150 minutes in an ice-cooled water bath. The running buffer contained 0.5x TBE (Thermo Scientific, 44.5 mM Tris, 44.5 mM boric acid and 1mM EDTA; pH 8.0) and 10 mM MgAc₂. The band corresponding to the DNA motif was excised with a surgical blade and loaded in a Freeze 'N Squeeze gel extraction spin column (Bio-Rad). The column was centrifuged for 20 minutes at 3000 RCF and 4 °C. To replace the buffer with the storing buffer (same with the annealing buffer), the flow through was collected and pipetted to a Vivaspin 500, MWCO 3000 (Sartorius). After an initial spin at 3000 RCF for 30 minutes, 300 µL of 1x storing buffer was added to the solution and centrifuged again at 3000 RCF for 90 minutes. This last step was repeated one more time to ensure that the buffer is replaced.

Native PAGE.

6% polyacrylamide gels were prepared following standard protocols. The gels were run at 120 V for 50 min in 0.5xTBE. The gels were stained with SYBR Gold (Sigma) and imaged with ChemiDoc MP (Bio-Rad).

Further details on analyses of AFM images.

After opening of an image through a third-party developed script³⁶⁴ in MATLAB³⁶⁵, the routine includes standard practices, such as: median line differences removal, adaptive thresholding to identify background, polynomial surface fitting of the background and median line removal using background as reference³⁶⁶. We iterated the process a second time after resizing the image to a standard pixel width of 0.34 nm. Finally, we applied a gaussian filter with standard deviation of 2 pixels and capped the final values between 2% and 98% of the values in the image.

For segmentation and skeletonization, a first enhancement of the contrast between foreground and background is obtained by applying a custom filter based on a kernel of radii equal to the size of the particle of interest and intensity that would reduce progressively from the center to the border, in a way that would take into account the different orientations that a particle can assume. Initial thresholding and average filtering of the background are then applied to further enhance the image. Afterwards, a preliminary skeletonization step based on the watershed transform is performed. Using the preliminary skeleton, we perform a second, more precise thresholding to obtain a mask. This mask is then further processed to enhance holes, remove full areas and fill scars. For the steady state images, when automatic filling of scars would fail due their excessive thickness, we would resort to manual correction of the original image and restart the process.

Finally, the mask is refined through morphological operators and a 4-connected skeleton is extracted through a standard skeletonization algorithm.

The polygon and particle detection part are based on the hypothesis that segments in an image connect the centers of two particles. Therefore, we proceed with the identification of segments in the skeletonized image considering that a segment is either: (1) shared by two polygons, (2) isolated or (3) forming an angle with another one. For each isolated connected component in the foreground, we try to divide it in segments based on principle 1 and then apply a Ramer-Douglas-Peucker algorithm (based on the native one implemented in MATLAB) in order to identify all the vertices in each segmented line. To facilitate the vertex detection algorithm, when possible, we define a list of initial candidate vertices, consisting of branched points and

the point that is furthest away from the center of mass. Finally, each vertex is the center of a 3PS-particle and polygons can be identified by counting their vertices.

Finally, we check how many polygons and particles (and eventual properties like being in contact with the background) a connected component has and stores it in dedicated matrices.

Detailed protocol for patchy-particle simulations.

The current version of the engine used is made available online. Main modifications from the engine developed by Hedges³⁶⁷ involve separation in modules of the different subparts of the script, a dedicated routine to parse input conditions for each simulation from a json file, the definition of a new potential and variables, and implementations of moves to change the states of the patch.

The interaction between particles is calculated as pairwise potential with the following formulation:

$$H_{(r_{ij}, \theta_i, \theta_j, p_i, p_j)} = \begin{cases} \infty, & r_{ij} < \sigma \\ -\varepsilon p_i p_j, & \sigma < r_{ij} < \sigma + \delta \wedge \theta_i < \theta_{pw} \wedge \theta_j < \theta_{pw} \\ 0, & \text{otherwise} \end{cases}$$

Eq. 0-1

In this formula, r_{ij} is the center-to-center distance between the two interacting particles, i and j ; d_p is the diameter of a particle; r_c is the cutoff distance for the interaction; the term ε represent

the energetic contribution of the binding; θ_i is the smallest angle formed by the direction of any of the patches in particle i and the line connecting the centers, similarly θ_j is the smallest angle formed by the direction of any of the patches in particle j and said line; θ_{pw} represents the maximum angle at which the interaction can happen; p_i and p_j are respectively the states of the aforementioned patches in i and j and they can either assume a value of 0 or a value of 1. This formulation corresponds to a standard Kern-Frenkel potential³⁶⁸, with the addition that both patches need to be in close state to be active.

To evaluate the acceptance of moves we implement a classical Metropolis scheme³⁶⁹ where the variation of Free Energy G between the original configuration “ a ” and the resulting configuration “ b ” is calculated as follow:

$$\Delta G_{a \rightarrow b} = \Delta H_{a \rightarrow b} + \Delta P_{a \rightarrow b} + S$$

Eq. 0-2

$\Delta H_{a \rightarrow b}$ represents the free energy variation between the two configurations based on changes on the aforementioned pairwise potential. $\Delta P_{a \rightarrow b}$ is the free energy variation resulting from switching a patch state while moving from a to b , based on the probability of the patch being in “open” state, P_o , when not interacting with others.

Since we have only 2 possible states the specific formulation of the second term is:

$$\Delta P_{a \rightarrow b} = \begin{cases} 0, & p_a = p_b \\ \log\left(\frac{P_o}{1-P_o}\right), & p_a = 0 \wedge p_b = 1 \\ \log\left(\frac{1-P_o}{P_o}\right), & p_a = 1 \wedge p_b = 0 \end{cases}$$

Eq. 0-3

Where p_a represent the state of the patch in state a and p_b represent the state of the patch in state b .

S is a biasing potential taking into account the resistance to change due to the local unbinding to mica. This term is equal to a designed value if the particle in state a is already interacting with others otherwise it is 0. This term represents the hypothesis that a monomer interacting with another engages with the mica surface better than an isolated one. This is supported experimentally by the fact that isolated monomers could not be resolved and yet dimers can be clearly observed in an AFM image.

The units of length in the simulations are normalized using as reference length the diameter of a particle (16 nm in our case), the energy is normalized by the inverse of the thermodynamic beta and angles are measured in radians.

Simulations are performed in 2D placing 1500 particles over an area of 150x150 normalized units ($\sim 1.6 \times 1.6 \mu\text{m}^2$), matching densities measured for our low-density images. The total number of steps is 2.4×10^7 for each simulation. The interaction cutoff is set at 1.03, implying that a π - π stacking would have a width of 0.6 nm. θ_{pw} has been tested between 0.06 and 0.40 radians (used for Figure 3.5) while ε has been tested between 2 to 10 (used for Figure 3.4). In Figure 3.5, ε was kept at 6. S, when a particle is interacting with others, has a value of 6, otherwise 0.

Particle positions and orientations are initialized randomly, while each patch state is initialized to 0.

Specifications for simulations of isolated monomers in solutions.

The protocol followed the one reported in Materials and Methods. Production runs consisted of 1.85×10^8 steps. 9 replicas were performed for each monomer, respectively: short, long flexible and long rigid. During analysis we discard the first 1×10^7 steps and considered frames collected every 5×10^5 steps. In Figure 3.5 are reported for each compound characteristic configurations and the RMSF computed over all the trajectories.

Specifications for simulations of isolated monomers on surface.

In a similar fashion to what has been done in Materials and Methods, we prepared flat *de novo* designs of our monomers. However, these models have been used to select the starting configurations from the trajectories simulated in the previous section as follows: for each monomer, we selected as starting configuration the one that would have the lower RMSD compared to the manually constructed flat models. Afterwards, we manually aligned the starting structures to a plane perpendicular to the y axis using OxView^{370,371}, and then applied the rest of the protocol described in Materials and Methods. In this context, we run simulations

while implementing two repulsion planes, confining the compound in a layer of around 2 nm, starting with a force constant of 0.3 for the minimization. Additionally, we increased the steps in the minimization process to 7.5e6. Throughout the equilibration NVT simulations we slowly increased the force of the repulsion plane, by setting the associated parameter to: 0.3, 0.6, 0.9, 1.2, 1.5, 1.8 and 2.1. The last was then kept throughout the last equilibration run and production. Production runs consisted in 1.35e8 steps. 12 replicas were performed for each monomer. During analysis we would discard the first 1e7 steps and considered frames collected every 5e5 steps.

In Figure 0.11 are reported for each compound characteristic configurations and the RMSF computed over all the trajectories; end to end distance are plotted in Figure 0.13.

Supplementary Figures and Tables

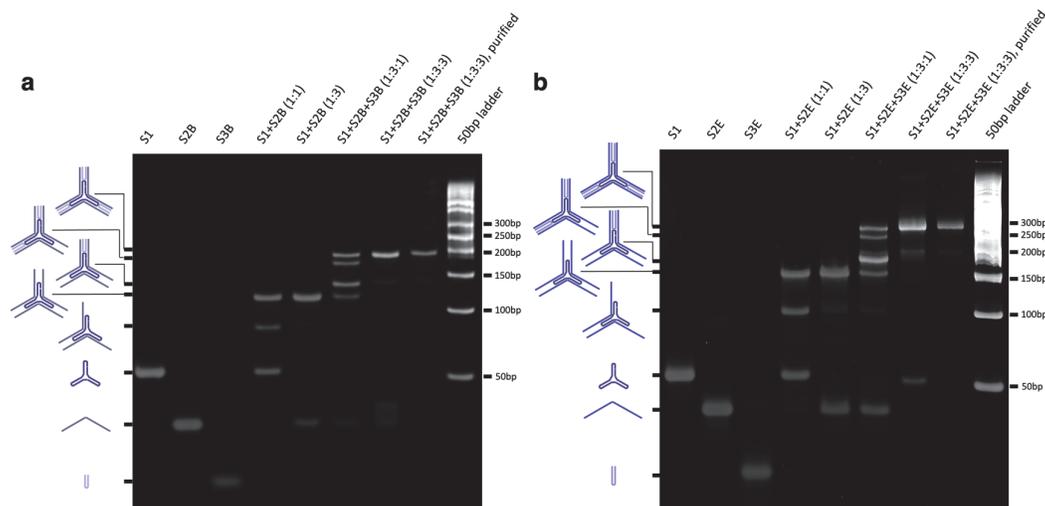


Figure 0.1: Native PAGE (6%) analysis of the formation of (a) short GCTA and (b) long GCTA DNA 3PS.

The compositions of the samples and the structures corresponding to each band are shown above and on left of the gels respectively.

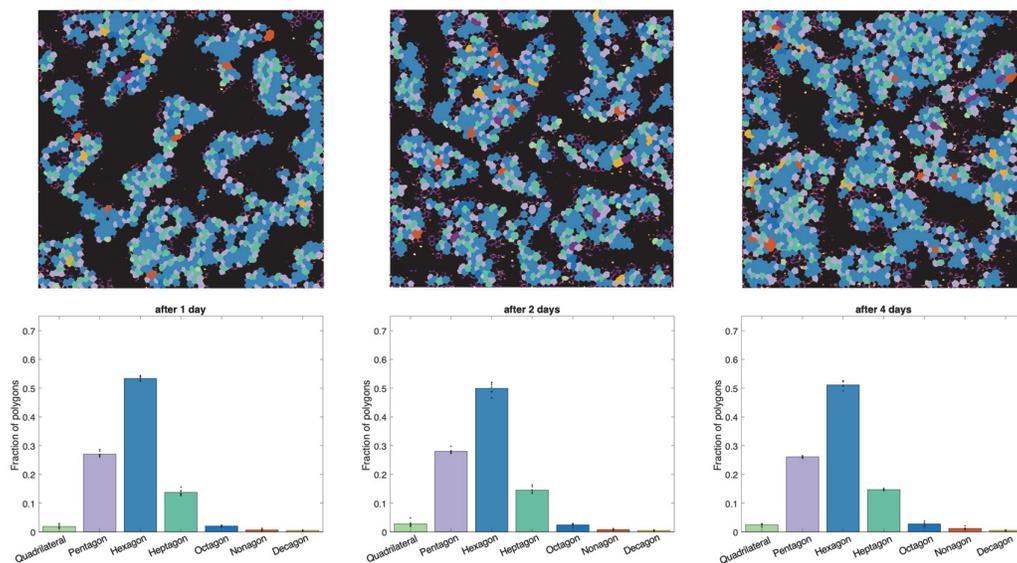


Figure 0.2: The evolution of the assembly after 1-4 days.

Bars present a weighted mean based on the number of monomers observed in an image. Each black dot represents the fraction of a polygon in a unique $750 \times 750 \mu\text{m}^2$ area. After a day of incubation, the distribution of polygons remains constant, prompting us to opt for a one-day incubation period on mica. While the surface coverage continues to increase gradually due to the slow evaporation of the sample, the assembly properties remain unaltered.

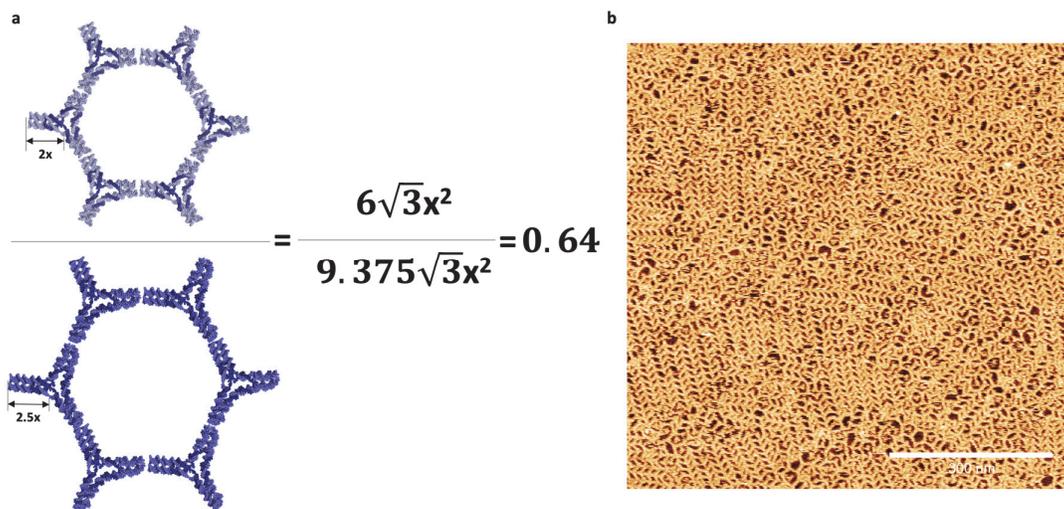


Figure 0.3: DNA concentration for AFM experiments.

a, Long 3PS concentration. x indicates a turn of dsDNA. To cover the surface as much as short 3PS, $0.64 \times 6\text{nM} = 3.84\text{nM}$ of long 3PS was used in the experiments. **b**, Overcrowding. In the cases of excessively high concentration, some blunt-end interactions are disrupted and the 3PS pack in a denser final form that minimizes the void between them.

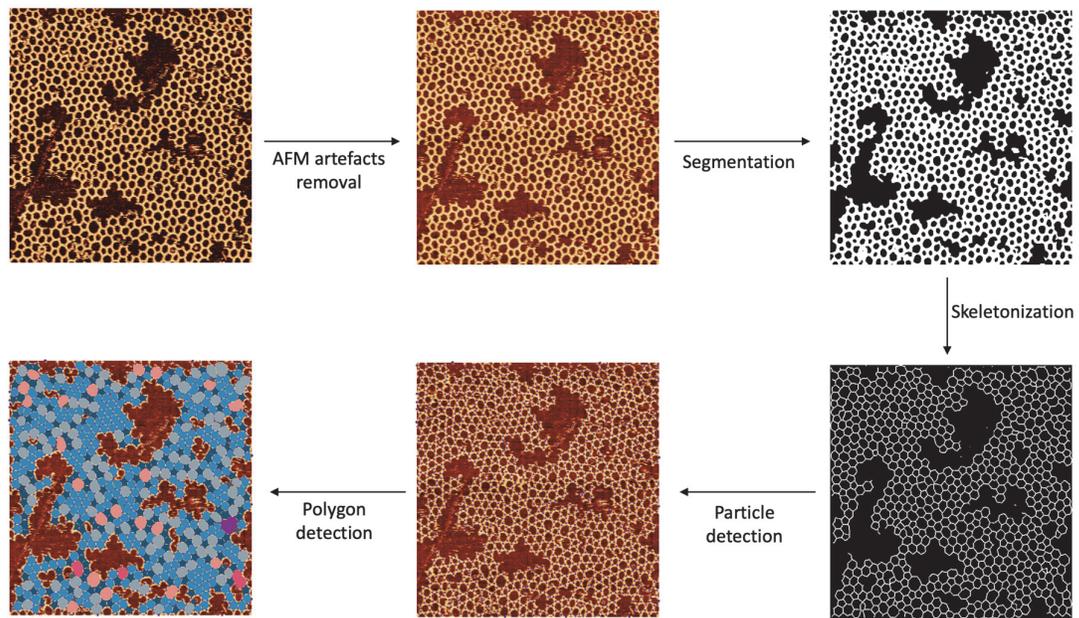


Figure 0.4: Image processing and analysis flowchart

The typical image processing and analysis workflow includes (1) AFM artefact removal, (2) segmentation, (3) skeletonization, (4) particle detection, and (5) polygon detection.

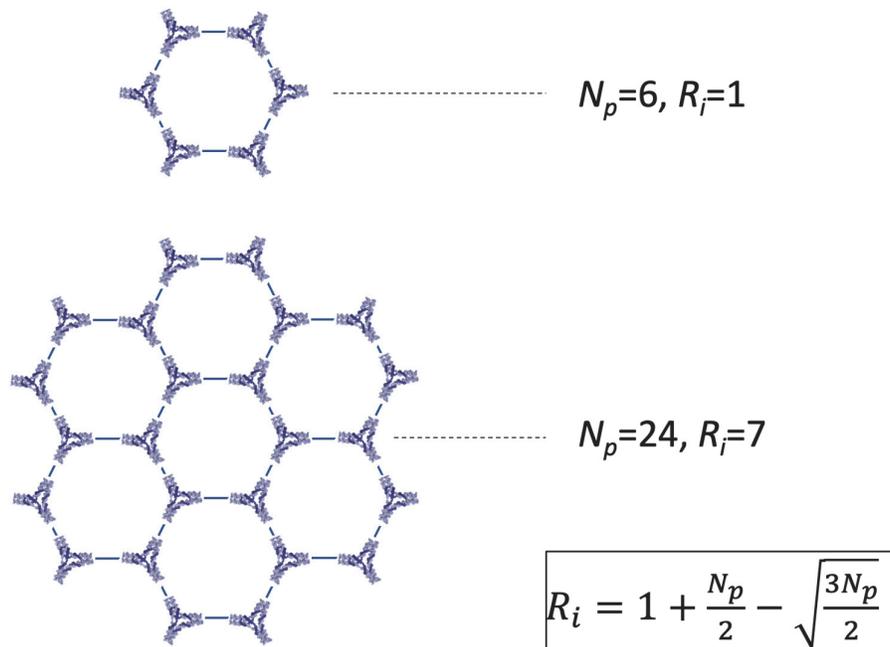


Figure 0.5: Ideal island for the calculation of Network Density (ND).

ND is the ratio between the number of rings present in an island and the number of rings in an ideal island (R_i) formed by an equivalent number of particles (N_p). The term "ideal island" refers to a flawlessly radial structure devoid of any defects.

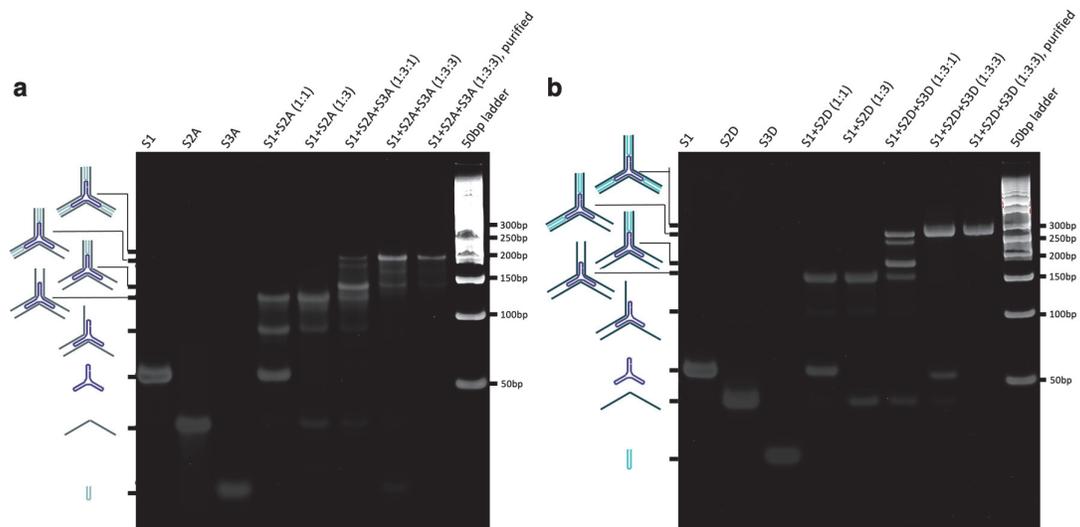


Figure 0.6: Native PAGE (6%) analysis of the formation of (a) short TATA and (b) long TATA 3PS.

The compositions of the samples and the structures corresponding to each band are shown above and on left of the gels respectively.

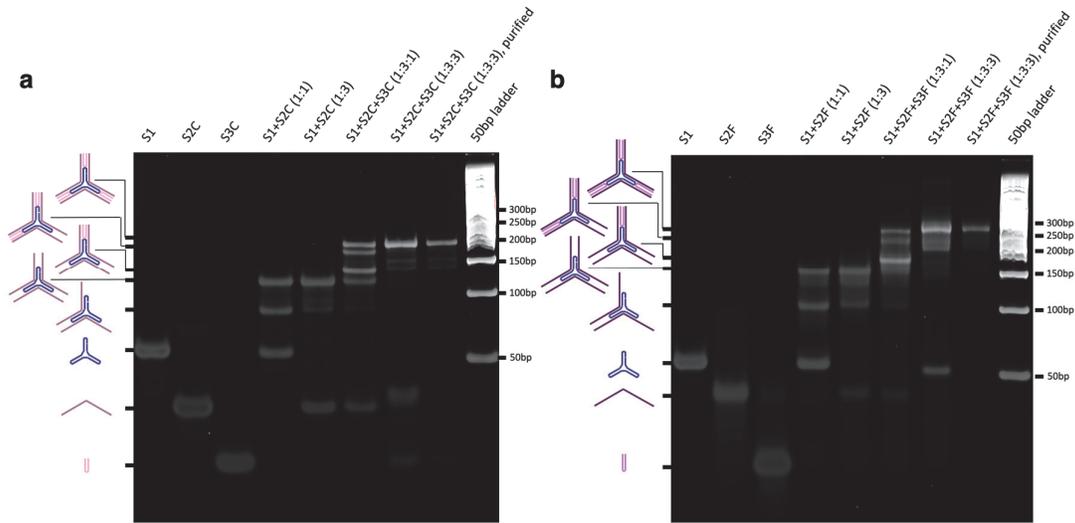


Figure 0.7: Native PAGE (6%) analysis of the formation of (a) short GCGC and (b) long GCGC 3PS.

The compositions of the samples and the structures corresponding to each band are shown above and on left of the gels respectively.

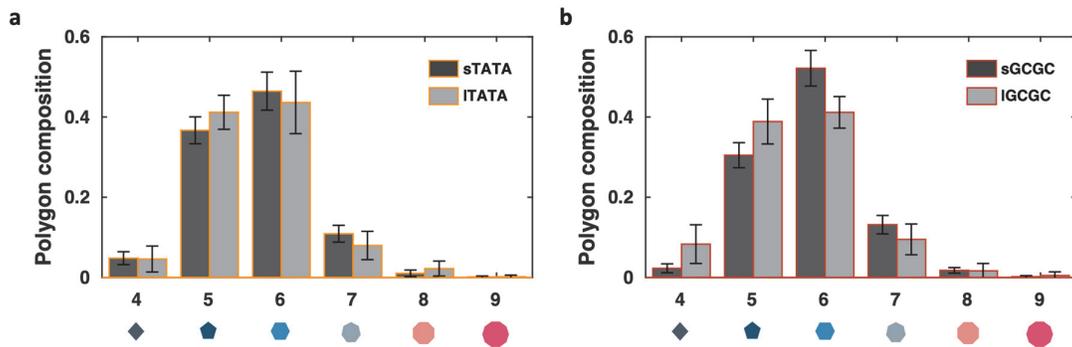


Figure 0.8: Polygon compositions at the steady-state for (a) TATA and (b) GCGC.

The polygon composition of TATA and GCGC 3PS after a day of incubation on mica. The bars include the data of at least 12 images ($750 \times 750 \mu\text{m}^2$) per condition and they present a weighted mean based on the monomers observed in an image. Error bars indicates the standard deviation.

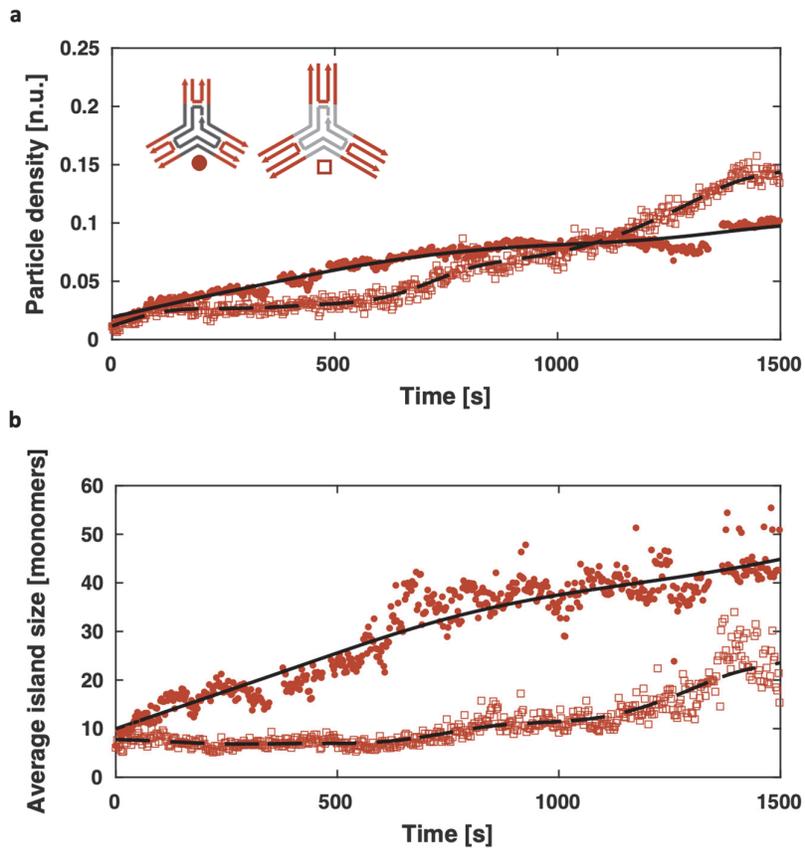


Figure 0.9: Dynamic self-assembly of short and long GCGC.

a, particle density on mica as a function of time. The number of particles on surface monotonically increases for both long and short 3PS. **b**, average island size as a function of time. The islands formed by the short 3PS continuously increases with the arrival of more monomers on the surface. This strongly supports the growth phase of the assembly mechanisms, with every new monomer attaching to an existing island. Contrary, the islands formed by the long 3PS lack any kind of growth, meaning all incoming monomers try to make new nuclei. This changes around 1000s, where the surface density is so high, the small islands start to coalesce.

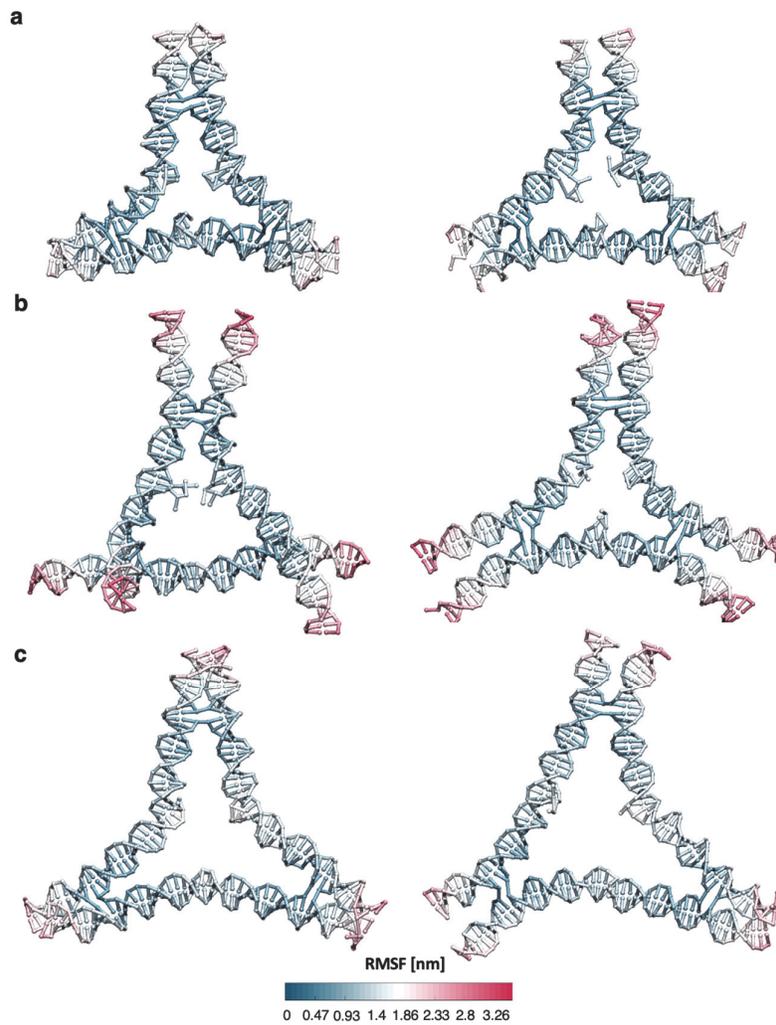


Figure 0.10: OxDNA simulation frames of (a) short, (b) long flexible and (c) long rigid DNA 3PS in solution.

The left frames display the conformations with the lowest RMSD when compared to the average conformation.

The right frames depict the conformations closest to the flat ones.

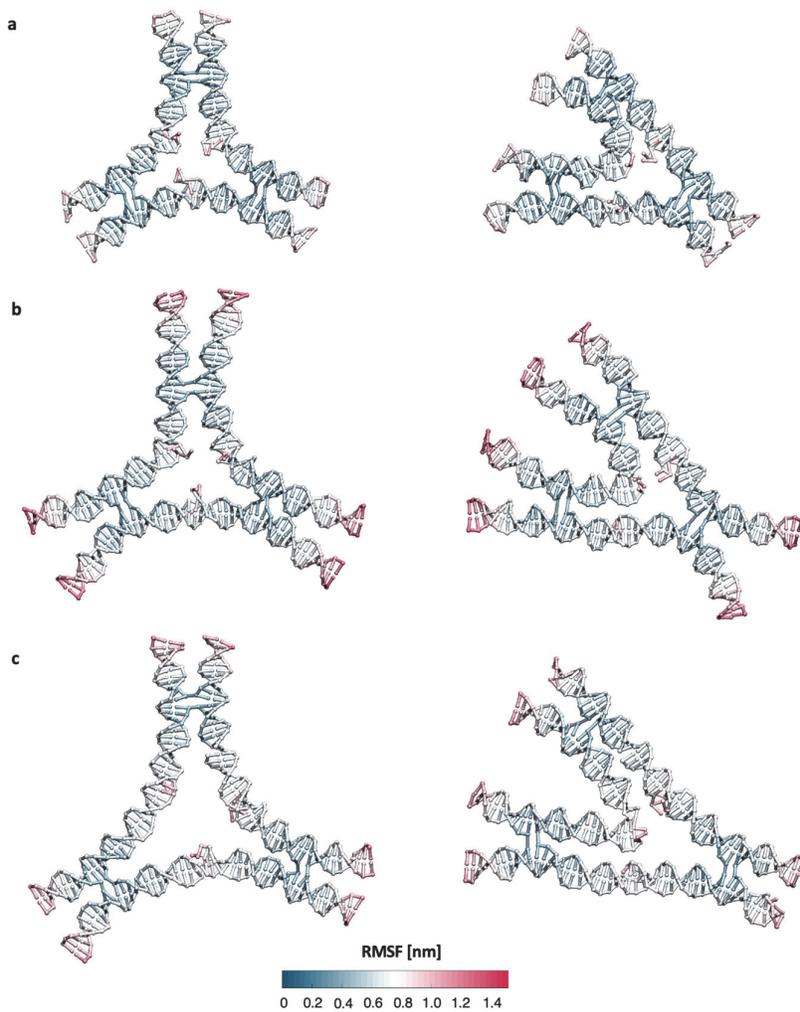


Figure 0.11: OxDNA simulation frames of (a) short, (b) long flexible and (c) long rigid DNA 3PS confined on the surface.

The left frames display the conformations with the lowest Root Mean Square Deviation (RMSD) when compared to the average conformation. The right frames depict the conformations with the highest RMSD.

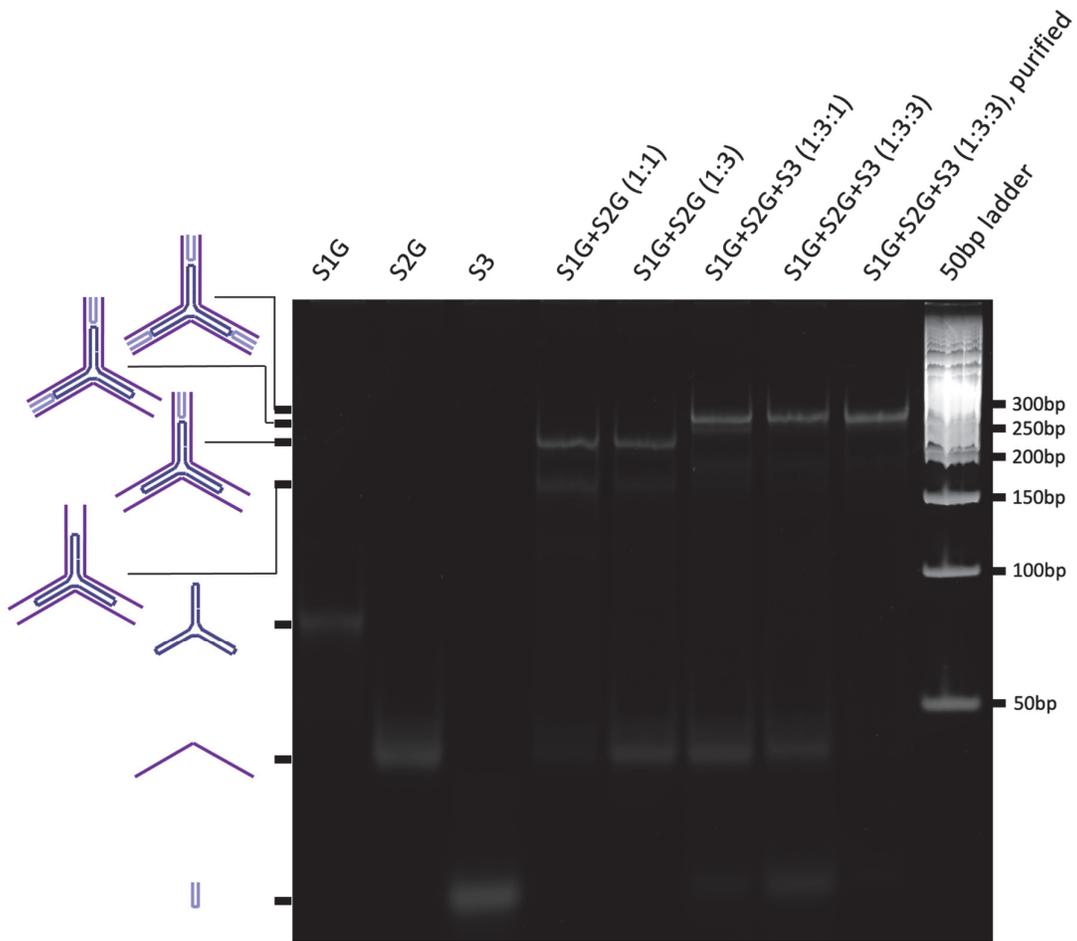


Figure 0.12: Native PAGE (6%) analysis of the formation of long rigid (LR) 3PS.

The compositions of the samples and the structures corresponding to each band are shown above and on left of the gel respectively.

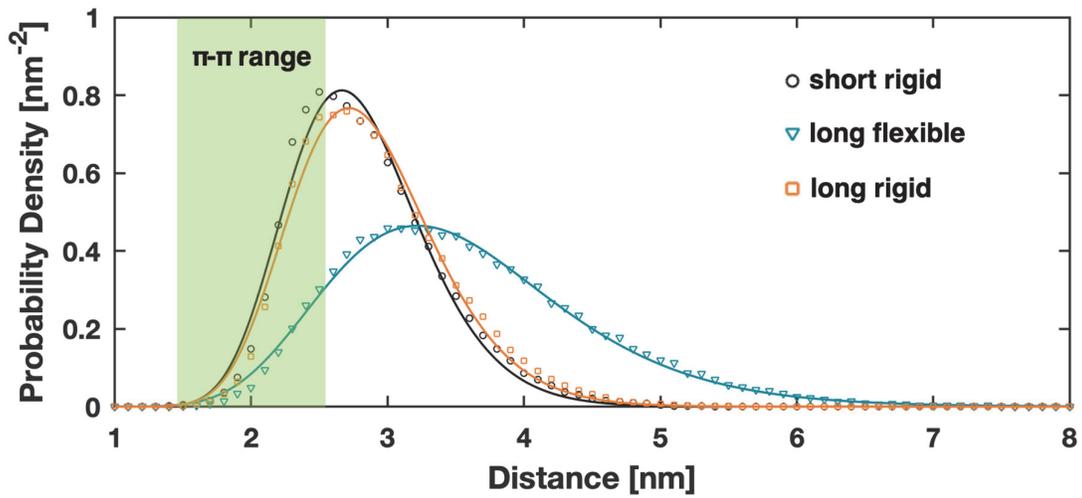


Figure 0.13: Probability distribution function of 3PS end-to-end distances based on OxDNA simulations.

Each 3PS was forced to be in a plane as explained in the Extended Methods. The data for the short rigid and long flexible are already reported in Figure 3.4b. Long rigid 3PS having a similar end-to-end distance distribution to short 3PS is a strong indication that their interface flexibility is similar.

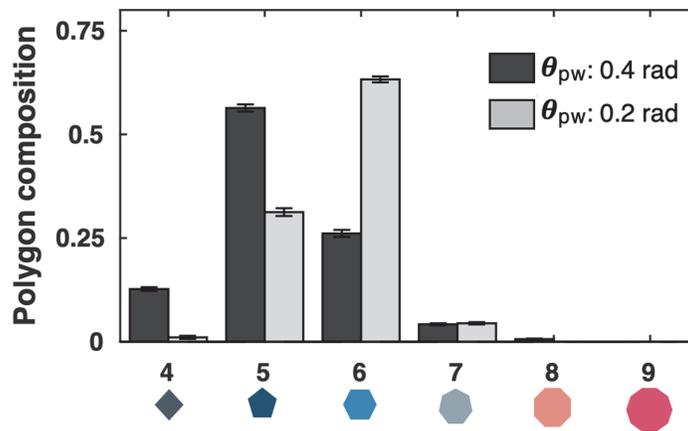


Figure 0.14: Polygon composition in the patchy particle simulations.

In this set of simulations ε , P_o were 6 and 0.3 respectively. Since the fraction of hexagons we measure *in vitro* is ~ 0.5 which is included in the interval observed *in silico* ($0.24 < x < 0.67$), we expect the patch widths that correctly represent our constructs to be bound between 0.2 and 0.4 radians.

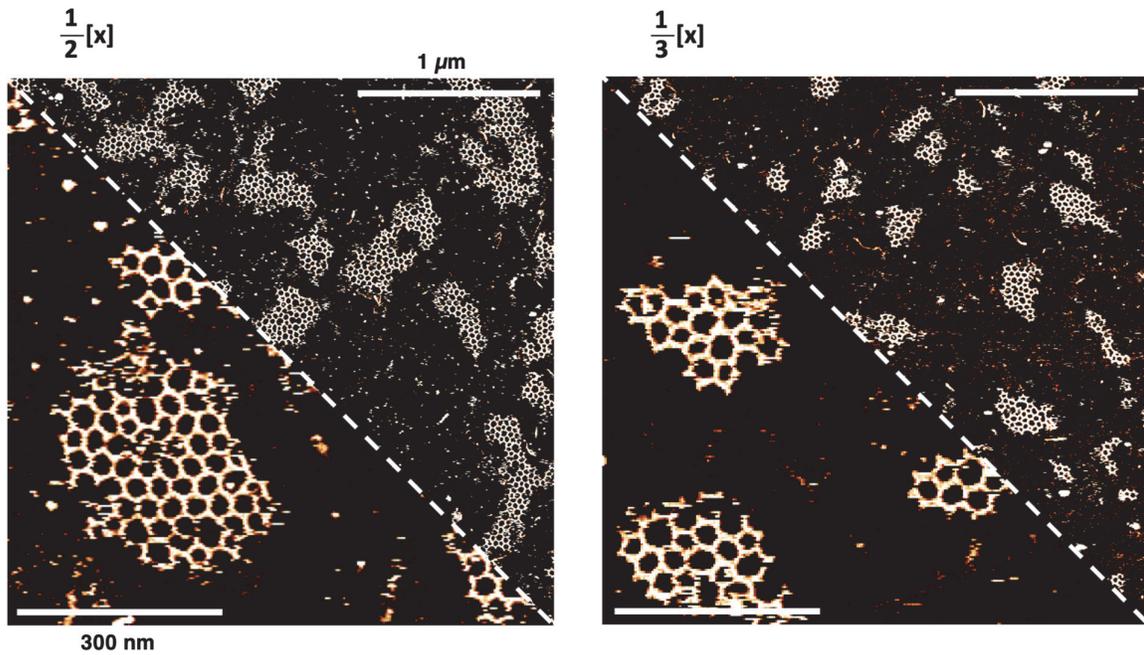
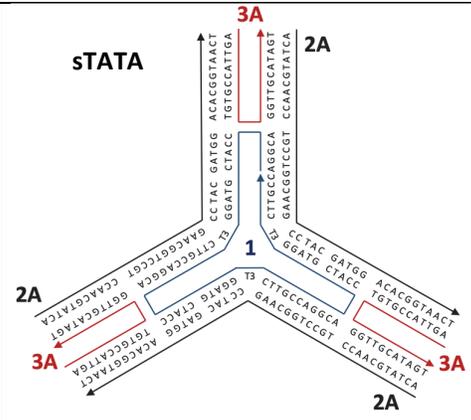
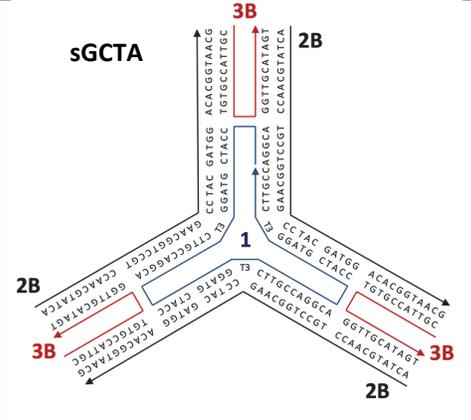
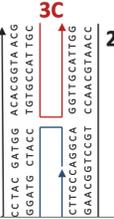
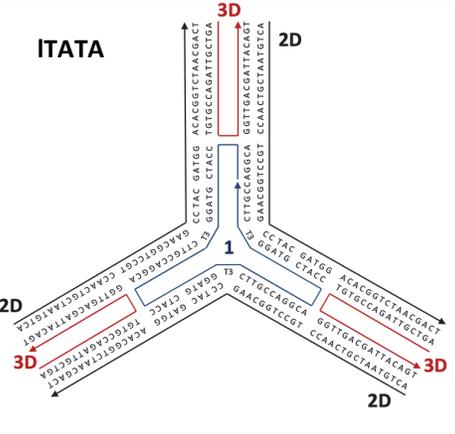
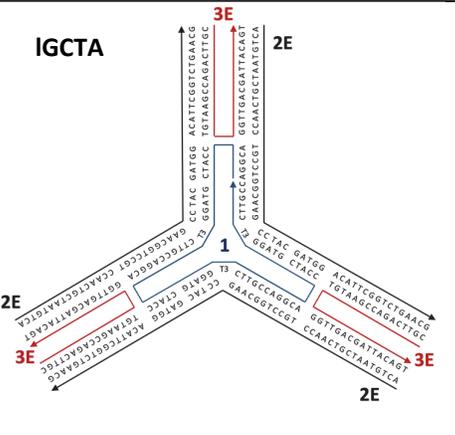
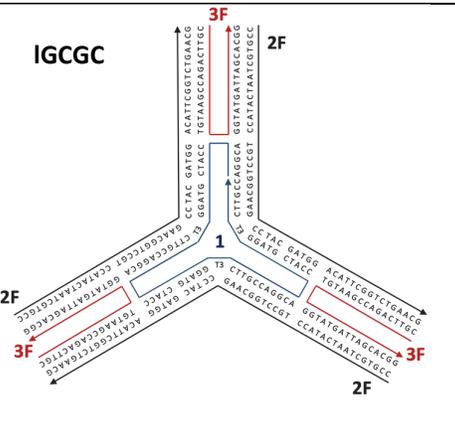


Figure 0.15: AFM images of the long rigid 3PS self-assembly at lower concentrations

Long rigid 3PS assembles into radial islands at lower concentrations demonstrating its similar assembly mechanisms as short 3PS.

Table 0-1. DNA motifs and the base sequences of the strands.

Motif	Strand	Sequence
Present in all motifs except long rigid	1	5'-AGGCACCATCGTAGGTTTCTTGC CAGGCACCATCGTAGGTTTCTTGCC AGGCACCATCGTAGGTTTCTTGCC-3'
 <p>sTATA</p>	2A	5'-ACTATGCAACCTGCCTGGCAAGC CTACGATGGACACGGTAACT-3'
	3A	5'-AGTTACCGTGTGGTTGCATAGT-3'
 <p>sGCTA</p>	2B	5'-ACTATGCAACCTGCCTGGCAAGC CTACGATGGACACGGTAAACG-3'
	3B	5'-CGTTACCGTGTGGTTGCATAGT-3'
	2C	5'-CCAATGCAACCTGCCTGGCAAGC CTACGATGGACACGGTAAACG-3'

<p>sGCGC</p> 	<p>3C</p>	<p>5'-CGTTACCGTGTGGTTGCATTGG-3'</p>
<p>ITATA</p> 	<p>2D</p>	<p>5'-ACTGTAATCGTCAACCTGCCTGGC AAGCCTACGATGGACACGGTCTAAC GACT-3'</p>
	<p>3D</p>	<p>5'-AGTCGTTAGACCGTGTGGTTGAC GATTACAGT-3'</p>
<p>IGCTA</p> 	<p>2E</p>	<p>5'-ACTGTAATCGTCAACCTGCCTGGC AAGCCTACGATGGACATTGGGTCTG AACG-3'</p>
	<p>3E</p>	<p>5'-CGTTCAGACCGAATGTGGTTGA CGATTACAGT-3'</p>
<p>IGCGC</p> 	<p>2F</p>	<p>5'-CCGTGCTAATCATACTGCCTGGC AAGCCTACGATGGACATTGGGTCTG AACG-3'</p>
	<p>3F</p>	<p>5'-CGTTCAGACCGAATGTGGTATGATT AGCACGG-3'</p>

	1B 5'-AGTAGGCACCAGTCGGATACAGG CTTGACATAGTAGGCACCAGTCGGA TACAGGCTTGACATAGTAGGCACCA GTCGGATACAGGCTTGACAT-3'
	2G 5'-ACTATGCAACCTGCCTACTATGTC AAGTTTCCTGTATCCGACTGGACACG GTAACG-3'

Supplementary Movies

<https://www.biorxiv.org/content/10.1101/2023.09.04.556250v1.supplementary-material>

Movie S1. Dynamic self-assembly of short GCGC

Movie S2. Dynamic self-assembly of long GCGC

Movie S3. Dynamic self-assembly of short GCTA

Movie S4. Dynamic self-assembly of long GCTA

Movie S5. Dynamic self-assembly of short TATA

Movie S6. Dynamic self-assembly of long TATA

Movie S7. Patchy-particle simulation of short

Movie S8. Patchy-particle simulation of long

Movie S9. Patchy-particle simulation of diffusion limited aggregates

Movie S10. Patchy-particle simulation of monomeric gas

References

1. Binnig, G., Quate, C. F. & Gerber, Ch. Atomic Force Microscope. *Phys. Rev. Lett.* **56**, 930–933 (1986).
2. Smith, D. P. E., Binnig, G. & Quate, C. F. Atomic point-contact imaging. *Applied Physics Letters* **49**, 1166–1168 (1986).
3. Hansma, P. K., Elings, V. B., Marti, O. & Bracker, C. E. Scanning tunneling microscopy and atomic force microscopy: application to biology and technology. *Science* **242**, 209–216 (1988).
4. Marti, O. *et al.* Atomic force microscopy of an organic monolayer. *Science* **239**, 50–52 (1988).
5. Marti, O. *et al.* Scanning probe microscopy of biological samples and other surfaces. *J Microsc* **152**, 803–809 (1988).
6. Worcester, D. L., Miller, R. G. & Bryant, P. J. Atomic force microscopy of purple membranes. *J Microsc* **152**, 817–821 (1988).
7. Drake, B. *et al.* Imaging Crystals, Polymers, and Processes in Water with the Atomic Force Microscope. *Science* **243**, 1586–1589 (1989).
8. Tian, X. *et al.* Investigation of micro-surface potential of coals with different metamorphism by AFM. *Measurement: Journal of the International Measurement Confederation* **172**, (2021).
9. Wozniak, M. J., Glowacka, A. & Kozubowski, J. A. Magnetic properties of austeno-ferritic stainless steel after cathodic hydrogen charging. *Journal of Alloys and Compounds* **404–406**, 626–629 (2005).
10. Rief, M., Gautel, M., Oesterhelt, F., Fernandez, J. M. & Gaub, H. E. Reversible Unfolding of Individual Titin Immunoglobulin Domains by AFM. *Science* **276**, 1109–1112 (1997).
11. Khan, M. K., Wang, Q. Y. & Fitzpatrick, M. E. 1 - Atomic force microscopy (AFM) for materials characterization. in *Materials Characterization Using Nondestructive Evaluation (NDE) Methods*

- (eds. Hübschen, G., Altpeter, I., Tschuncky, R. & Herrmann, H.-G.) 1–16 (Woodhead Publishing, 2016). doi:10.1016/B978-0-08-100040-3.00001-8.
12. Amrein, M. W. & Stamov, D. Atomic force microscopy in the life sciences. in *Springer Handbooks* 1469–1505 (Springer, 2019). doi:10.1007/978-3-030-00069-1_31.
 13. Quate, C. F. The AFM as a tool for surface imaging. *Surface Science* **299–300**, 980–995 (1994).
 14. Optical Imaging. *National Institute of Biomedical Imaging and Bioengineering*
<https://www.nibib.nih.gov/science-education/science-topics/optical-imaging>.
 15. AFM Principles.
https://www.weizmann.ac.il/Chemical_Research_Support/surflab/peter/afmworks/.
 16. Putman, C. A. J., De Grooth, B. G., Van Hulst, N. F. & Greve, J. A detailed analysis of the optical beam deflection technique for use in atomic force microscopy. *Journal of Applied Physics* **72**, 6–12 (1992).
 17. Putman, C. A. J., de Grooth, B. G., van Hulst, N. F. & Greve, J. A theoretical comparison between interferometric and optical beam deflection technique for the measurement of cantilever displacement in AFM. *Ultramicroscopy* **42–44**, 1509–1513 (1992).
 18. Dukic, M., Adams, J. D. & Fantner, G. E. Piezoresistive AFM cantilevers surpassing standard optical beam deflection in low noise topography imaging. *Sci Rep* **5**, 16393 (2015).
 19. Xia, F. & Youcef-Toumi, K. Review: Advanced Atomic Force Microscopy Modes for Biomedical Research. *Biosensors* **12**, 1116 (2022).
 20. Zhong, Q., Inniss, D., Kjoller, K. & Elings, V. B. Fractured polymer/silica fiber surface studied by tapping mode atomic force microscopy. *Surface Science* **290**, L688–L692 (1993).
 21. Martin, Y., Williams, C. C. & Wickramasinghe, H. K. Atomic force microscope–force mapping and profiling on a sub 100-Å scale. *Journal of Applied Physics* **61**, 4723–4729 (1987).

22. Rosa-Zeiser, A., Weilandt, E., Hild, S. & Marti, O. The simultaneous measurement of elastic, electrostatic and adhesive properties by scanning force microscopy: pulsed-force mode operation. *Meas. Sci. Technol.* **8**, 1333 (1997).
23. Passeri, D. *et al.* Magnetic force microscopy. *Biomatter* **4**, e29507 (2014).
24. Harnessing the Strengths of Electrical AFM Modes for Nanoscale Investigation. *AZoNano.com* <https://www.azonano.com/article.aspx?ArticleID=6655> (2023).
25. Kouzeki, T., Tatezono, S. & Yanagi, H. Electrochromism of Orientation-Controlled Naphthalocyanine Thin Films. *J. Phys. Chem.* **100**, 20097–20102 (1996).
26. Wiley-VCH - Atomic Force Microscopy in Liquid. <https://www.wiley-vch.de/de/fachgebiete/naturwissenschaften/chemie-11ch/analytische-chemie-11ch1/atomic-force-microscopy-in-liquid-978-3-527-32758-4>.
27. Casuso, I., Kodera, N., Le Grimmelc, C., Ando, T. & Scheuring, S. Contact-Mode High-Resolution High-Speed Atomic Force Microscopy Movies of the Purple Membrane. *Biophys J* **97**, 1354–1361 (2009).
28. Scheuring, S. *et al.* Nanodissection and high-resolution imaging of the Rhodospseudomonas viridis photosynthetic core complex in native membranes by AFM. *Proc Natl Acad Sci U S A* **100**, 1690–1693 (2003).
29. Reviakine, I., Bergsma-Schutter, W. & Brisson, A. Growth of Protein 2-D Crystals on Supported Planar Lipid Bilayers Imaged *in Situ* by AFM. *Journal of Structural Biology* **121**, 356–362 (1998).
30. Müller, D. J., Engel, A., Carrascosa, J. L. & Vélez, M. The bacteriophage ϕ 29 head–tail connector imaged at high resolution with the atomic force microscope in buffer solution. *The EMBO Journal* **16**, 2547–2553 (1997).

31. Czajkowsky, D. M., Sheng, S. & Shao, Z. Staphylococcal alpha-hemolysin can form hexamers in phospholipid bilayers. *J Mol Biol* **276**, 325–330 (1998).
32. Goldsbury, C., Kistler, J., Aebi, U., Arvinte, T. & Cooper, G. J. S. Watching amyloid fibrils grow by time-lapse atomic force microscopy¹. *Journal of Molecular Biology* **285**, 33–39 (1999).
33. Bezanilla, M. *et al.* Motion and enzymatic degradation of DNA in the atomic force microscope. *Biophys J* **67**, 2454–2459 (1994).
34. Stoffler, D., Goldie, K. N., Feja, B. & Aebi, U. Calcium-mediated structural changes of native nuclear pore complexes monitored by time-lapse atomic force microscopy¹. *Journal of Molecular Biology* **287**, 741–752 (1999).
35. Hansma, P. K. *et al.* Tapping mode atomic force microscopy in liquids. *Applied Physics Letters* **64**, 1738–1740 (1994).
36. Ratcliff, G. C., Erie, D. A. & Superfine, R. Photothermal modulation for oscillating mode atomic force microscopy in solution. *Appl. Phys. Lett.* **72**, 1911–1913 (1998).
37. Ge, G. *et al.* MAC mode atomic force microscopy studies of living samples, ranging from cells to fresh tissue. *Ultramicroscopy* **107**, 299–307 (2007).
38. Hong, J. W., Khim, Z. G., Hou, A. S. & Park, S. Tapping mode atomic force microscopy using electrostatic force modulation. *Applied Physics Letters* **69**, 2831–2833 (1996).
39. Scanning attractive force microscope using photothermal vibration | Journal of Vacuum Science & Technology B | AIP Publishing.
<https://pubs.aip.org/avs/jvb/article/9/2/1318/1030384/Scanning-attractive-force-microscope-using>.

40. Kiracofe, D., Kobayashi, K., Labuda, A., Raman, A. & Yamada, H. High efficiency laser photothermal excitation of microcantilever vibrations in air and liquids. *Review of Scientific Instruments* **82**, 013702 (2011).
41. Penedo, M. *et al.* Photothermal excitation efficiency enhancement of cantilevers by electron beam deposition of amorphous carbon thin films. *Sci Rep* **10**, 17436 (2020).
42. Nievergelt, A. P., Banterle, N., Andany, S. H., Gönczy, P. & Fantner, G. E. High-speed photothermal off-resonance atomic force microscopy reveals assembly routes of centriolar scaffold protein SAS-6. *Nat Nanotechnol* **13**, 696–701 (2018).
43. Labuda, A. *et al.* Tapping Mode AFM Imaging in Liquids with blueDrive Photothermal Excitation. *Microscopy Today* **26**, 12–17 (2018).
44. blueDrive Photothermal Excitation for AFM | Asylum Research. *Oxford Instruments* <https://afm.oxinst.com/outreach/afm-bluedrive-photothermal-excitation>.
45. Pletikapić, G., Berquand, A., Radić, T. M. & Svetličić, V. QUANTITATIVE NANOMECHANICAL MAPPING OF MARINE DIATOM IN SEAWATER USING PEAK FORCE TAPPING ATOMIC FORCE MICROSCOPY(1). *J Phycol* **48**, 174–185 (2012).
46. De Pablo, P. J., Colchero, J., Gómez-Herrero, J. & Baró, A. M. Jumping mode scanning force microscopy. *Applied Physics Letters* **73**, 3300–3302 (1998).
47. Soppera, O. & Carre, C. Pulsed force mode AFM characterization of photopatterned polymers films. in *5th IEEE Conference on Nanotechnology, 2005*. 705–708 vol. 2 (2005). doi:10.1109/NANO.2005.1500863.
48. Sotres, J., Lostao, A., Gómez-Moreno, C. & Baró, A. M. Jumping mode AFM imaging of biomolecules in the repulsive electrical double layer. *Ultramicroscopy* **107**, 1207–1212 (2007).

49. Young, T. J. *et al.* The use of the PeakForce™ quantitative nanomechanical mapping AFM-based method for high-resolution Young's modulus measurement of polymers. *Meas. Sci. Technol.* **22**, 125703 (2011).
50. Schillers, H., Medalsy, I., Hu, S., Slade, A. L. & Shaw, J. E. PeakForce Tapping resolves individual microvilli on living cells. *J Mol Recognit* **29**, 95–101 (2016).
51. Chopinet, L., Formosa, C., Rols, M. P., Duval, R. E. & Dague, E. Imaging living cells surface and quantifying its properties at high resolution using AFM in QI™ mode. *Micron* **48**, 26–33 (2013).
52. Kaimaki, D.-M., Smith, B. E. & Durkan, C. On the use of nanomechanical atomic force microscopy to characterise oil-exposed surfaces. *RSC Adv.* **8**, 6680–6689 (2018).
53. Adams, J. D. *et al.* High-speed imaging upgrade for a standard sample scanning atomic force microscope using small cantilevers. *Review of Scientific Instruments* **85**, 093702 (2014).
54. Nanosurf - AFM - Atomic Force Microscopes - Nanosurf. <https://www.nanosurf.com/en/>.
55. Barrett, R. C. & Quate, C. F. High-speed, large-scale imaging with the atomic force microscope. *Journal of Vacuum Science & Technology B: Microelectronics and Nanometer Structures Processing, Measurement, and Phenomena* **9**, 302–306 (1991).
56. Walters, D. A. *et al.* Short cantilevers for atomic force microscopy. *Review of Scientific Instruments* **67**, 3583–3590 (1996).
57. Walters, D. A. *et al.* Atomic force microscopy using small cantilevers. in *Micromachining and Imaging* vol. 3009 43–47 (SPIE, 1997).
58. Viani, M. B. *et al.* Small cantilevers for force spectroscopy of single molecules. *Journal of Applied Physics* **86**, 2258–2262 (1999).

59. Chand, A., Viani, M. B., Schaffer, T. E. & Hansma, P. K. Microfabricated small metal cantilevers with silicon tip for atomic force microscopy. *Journal of Microelectromechanical Systems* **9**, 112–116 (2000).
60. Olympus Micro Cantilevers : BioLever fast. https://probe.olympus-global.com/en/product/bl_ac10ds_a2/.
61. Ando, T. *et al.* A high-speed atomic force microscope for studying biological macromolecules. *Proc Natl Acad Sci U S A* **98**, 12468–12472 (2001).
62. Humphris, A. D. L., Miles, M. J. & Hobbs, J. K. A mechanical microscope: High-speed atomic force microscopy. *Applied Physics Letters* **86**, 034106 (2005).
63. Humphris, A. D. L., Hobbs, J. K. & Miles, M. J. Ultrahigh-speed scanning near-field optical microscopy capable of over 100 frames per second. *Applied Physics Letters* **83**, 6–8 (2003).
64. Kindt, J. H., Fantner, G. E., Cutroni, J. A. & Hansma, P. K. Rigid design of fast scanning probe microscopes using finite element analysis. *Ultramicroscopy* **100**, 259–265 (2004).
65. Fantner, G. E. *et al.* Components for high speed atomic force microscopy. *Ultramicroscopy* **106**, 881–887 (2006).
66. Croft, D., Shed, G. & Devasia, S. Creep, Hysteresis, and Vibration Compensation for Piezoactuators: Atomic Force Microscopy Application. *Journal of Dynamic Systems, Measurement, and Control* **123**, 35–43 (1999).
67. Fantner, G. E. *et al.* Data acquisition system for high speed atomic force microscopy. *Review of Scientific Instruments* **76**, 026118 (2005).
68. Viani, M. B. *et al.* Probing protein–protein interactions in real time. *Nat Struct Mol Biol* **7**, 644–647 (2000).

69. Hölscher, H., Allers, W., Schwarz, U. D., Schwarz, A. & Wiesendanger, R. Determination of Tip-Sample Interaction Potentials by Dynamic Force Spectroscopy. *Phys. Rev. Lett.* **83**, 4780–4783 (1999).
70. Kielar, C., Zhu, S., Grundmeier, G. & Keller, A. Quantitative Assessment of Tip Effects in Single-Molecule High-Speed Atomic Force Microscopy Using DNA Origami Substrates. *Angew Chem Int Ed Engl* **59**, 14336–14341 (2020).
71. Xu, X., Carrasco, C., de Pablo, P. J., Gomez-Herrero, J. & Raman, A. Unmasking Imaging Forces on Soft Biological Samples in Liquids When Using Dynamic Atomic Force Microscopy: A Case Study on Viral Capsids. *Biophys J* **95**, 2520–2528 (2008).
72. Hatzopoulos, G. N. *et al.* Tuning SAS-6 architecture with monobodies impairs distinct steps of centriole assembly. *Nat Commun* **12**, 3805 (2021).
73. Nievergelt, A. P., Brillard, C., Eskandarian, H. A., McKinney, J. D. & Fantner, G. E. Photothermal Off-Resonance Tapping for Rapid and Gentle Atomic Force Imaging of Live Cells. *International Journal of Molecular Sciences* **19**, 2984 (2018).
74. Bauër, P. *et al.* A new method to measure mechanics and dynamic assembly of branched actin networks. *Scientific Reports* **7**, 15688 (2017).
75. Brill-Karniely, Y. Mechanical Measurements of Cells Using AFM: 3D or 2D Physics? *Frontiers in Bioengineering and Biotechnology* **8**, (2020).
76. Chang, Y.-R. *et al.* Automated AFM force curve analysis for determining elastic modulus of biomaterials and biological samples. *J Mech Behav Biomed Mater* **37**, 209–218 (2014).
77. Chaudhuri, O., Parekh, S. H., Lam, W. A. & Fletcher, D. A. Combined atomic force microscopy and side-view optical imaging for mechanical studies of cells. *Nature Methods* **6**, 383–387 (2009).

78. Haase, K. & Pelling, A. E. Investigating cell mechanics with atomic force microscopy. *J R Soc Interface* **12**, (2015).
79. Sahin, O., Magonov, S., Su, C., Quate, C. F. & Solgaard, O. An atomic force microscope tip designed to measure time-varying nanomechanical forces. *Nature Nanotechnology* **2**, 507–514 (2007).
80. Puricelli, L., Galluzzi, M., Schulte, C., Podestà, A. & Milani, P. Nanomechanical and topographical imaging of living cells by Atomic Force Microscopy with colloidal probes. *Review of Scientific Instruments* **86**, 033705 (2015).
81. Kontomaris, S. V., Malamou, A. & Stylianou, A. A New Approach for the AFM-Based Mechanical Characterization of Biological Samples. *Scanning* **2020**, 2896792 (2020).
82. Liu, H. *et al.* In Situ Mechanical Characterization of the Cell Nucleus by Atomic Force Microscopy. *ACS Nano* **8**, 3821–3828 (2014).
83. Garcia, R. Nanomechanical mapping of soft materials with the atomic force microscope: methods, theory and applications. *Chemical Society Reviews* **49**, 5850–5884 (2020).
84. Atomic Force Microscopy and Dissection of Gap Junctions | Science.
<https://www.science.org/doi/10.1126/science.1910206>.
85. Hansma, H. G. *et al.* Reproducible imaging and dissection of plasmid DNA under liquid with the atomic force microscope. *Science* **256**, 1180–1184 (1992).
86. Hoh, J. H. & Schoenenberger, C. A. Surface morphology and mechanical properties of MDCK monolayers by atomic force microscopy. *J Cell Sci* **107 (Pt 5)**, 1105–1114 (1994).
87. CHARACTERIZATION OF POLYMER SURFACES WITH ATOMIC FORCE MICROSCOPY | Annual Review of Materials Research.
<https://www.annualreviews.org/doi/10.1146/annurev.matsci.27.1.175>.

88. Garcia, R. & Herruzo, E. T. The emergence of multifrequency force microscopy. *Nature Nanotech* **7**, 217–226 (2012).
89. Intermodulation atomic force microscopy | Applied Physics Letters | AIP Publishing.
<https://pubs.aip.org/aip/apl/article/92/15/153106/326213/Intermodulation-atomic-force-microscopy>.
90. Rodriguez, B. J., Callahan, C., Kalinin, S. V. & Proksch, R. Dual-frequency resonance-tracking atomic force microscopy. *Nanotechnology* **18**, 475504 (2007).
91. Martínez, N. F. *et al.* Bimodal atomic force microscopy imaging of isolated antibodies in air and liquids. *Nanotechnology* **19**, 384011 (2008).
92. Garcia, R. & Proksch, R. Nanomechanical mapping of soft matter by bimodal force microscopy. *European Polymer Journal* **49**, 1897–1906 (2013).
93. Rodríguez, T. R. & García, R. Compositional mapping of surfaces in atomic force microscopy by excitation of the second normal mode of the microcantilever. *Applied Physics Letters* **84**, 449–451 (2004).
94. Raman, A. *et al.* Mapping nanomechanical properties of live cells using multi-harmonic atomic force microscopy. *Nature Nanotech* **6**, 809–814 (2011).
95. Stark, R. W. & Heckl, W. M. Fourier transformed atomic force microscopy: tapping mode atomic force microscopy beyond the Hookian approximation. *Surface Science* **457**, 219–228 (2000).
96. Damircheli, M. & Eslami, B. Design of V-shaped cantilevers for enhanced multifrequency AFM measurements. *Beilstein J. Nanotechnol.* **11**, 1525–1541 (2020).
97. Shamsudhin, N., Rothuizen, H., Nelson, B. J. & Sebastian, A. Multi-frequency atomic force microscopy: A system-theoretic approach. *IFAC Proceedings Volumes* **47**, 7499–7504 (2014).

98. Olubowale, O. H. *et al.* "May the Force Be with You!" Force–Volume Mapping with Atomic Force Microscopy. *ACS Omega* **6**, 25860–25875 (2021).
99. Radmacher, M., Cleveland, J. P., Fritz, M., Hansma, H. G. & Hansma, P. K. Mapping interaction forces with the atomic force microscope. *Biophysical Journal* **66**, 2159–2165 (1994).
100. Baselt, D. R. & Baldeschwieler, J. D. Imaging spectroscopy with the atomic force microscope. *Journal of Applied Physics* **76**, 33–38 (1994).
101. Efremov, Y. M., Shpichka, A. I., Kotova, S. L. & Timashev, P. S. Viscoelastic mapping of cells based on fast force volume and PeakForce Tapping. *Soft Matter* **15**, 5455–5463 (2019).
102. Quantitative Mechanical Property Mapping at the Nanoscale with PeakForce QNM - The Nanoscale World. <http://nanoscaleworld.bruker-axs.com/nanoscaleworld/media/p/418.aspx>.
103. Krottil, H.-U. *et al.* Pulsed force mode: a new method for the investigation of surface properties. *Surface and Interface Analysis* **27**, 336–340 (1999).
104. Expanding Atomic Force Microscopy with Hybrid Mode Imaging. <https://www.ntmdt-si.com/resources/applications/expanding-atomic-force-microscopy-with-hybrid-mode-imaging>.
105. QI™ Mode - NanoWizard® 4 NanoScience AFM - JPK BioAFM | Bruker. <https://www.jpk.com/products/atomic-force-microscopy/qi-mode/pid1205>.
106. PinPoint™ Nanomechanical Mode. <https://www.parksystems.com/index.php/park-spm-modes/97-mechanical-properties/3601-pinpoint-nanomechanical-mode>.
107. Bahrami, A., Bailly, C. & Nysten, B. Spatial resolution and property contrast in local mechanical mapping of polymer blends using AFM dynamic force spectroscopy. *Polymer* **165**, 180–190 (2019).

108. Kontomaris, S. V., Malamou, A. & Stylianou, A. The Hertzian theory in AFM nanoindentation experiments regarding biological samples: Overcoming limitations in data processing. *Micron* **155**, 103228 (2022).
109. Bustamante, C. *et al.* Circular DNA molecules imaged in air by scanning force microscopy. *Biochemistry* **31**, 22–26 (1992).
110. Shlyakhtenko, L. S. *et al.* A cruciform structural transition provides a molecular switch for chromosome structure and dynamics. *J Mol Biol* **296**, 1169–1173 (2000).
111. Vesenka, J. *et al.* Substrate preparation for reliable imaging of DNA molecules with the scanning force microscope. *Ultramicroscopy* **42-44 (Pt B)**, 1243–1249 (1992).
112. Mukherjee, S., Mondal, S., Acharya, S. & Bagchi, B. DNA Solvation Dynamics. *J. Phys. Chem. B* **122**, 11743–11761 (2018).
113. Lindsay, S. M. *et al.* STM and AFM images of nucleosome DNA under water. *J Biomol Struct Dyn* **7**, 279–287 (1989).
114. Ido, S. *et al.* Beyond the Helix Pitch: Direct Visualization of Native DNA in Aqueous Solution. *ACS Nano* **7**, 1817–1822 (2013).
115. Pyne, A., Thompson, R., Leung, C., Roy, D. & Hoogenboom, B. W. Single-Molecule Reconstruction of Oligonucleotide Secondary Structure by Atomic Force Microscopy. *Small* **10**, 3257–3261 (2014).
116. Leung, C. *et al.* Atomic Force Microscopy with Nanoscale Cantilevers Resolves Different Structural Conformations of the DNA Double Helix. *Nano Lett.* **12**, 3846–3850 (2012).
117. Brack, C. DNA electron microscopy. *CRC Crit Rev Biochem* **10**, 113–169 (1981).
118. Thundat, T. *et al.* Atomic force microscopy of DNA on mica and chemically modified mica. *Scanning Microsc* **6**, 911–918 (1992).

119. Bezanilla, M., Manne, S., Laney, D. E., Lyubchenko, Y. L. & Hansma, H. G. Adsorption of DNA to Mica, Silylated Mica, and Minerals: Characterization by Atomic Force Microscopy. *Langmuir* **11**, 655–659 (1995).
120. Bustamante, C. & Rivetti, C. Visualizing protein-nucleic acid interactions on a large scale with the scanning force microscope. *Annu Rev Biophys Biomol Struct* **25**, 395–429 (1996).
121. Bustamante, C., Rivetti, C. & Keller, D. J. Scanning force microscopy under aqueous solutions. *Curr Opin Struct Biol* **7**, 709–716 (1997).
122. Hansma, H. G., Bezanilla, M., Zenhausern, F., Adrian, M. & Sinsheimer, R. L. Atomic force microscopy of DNA in aqueous solutions. *Nucleic Acids Res* **21**, 505–512 (1993).
123. Yang, J., Takeyasu, K. & Shao, Z. Atomic force microscopy of DNA molecules. *FEBS Lett* **301**, 173–176 (1992).
124. Mou, J., Czajkowsky, D. M., Zhang, Y. & Shao, Z. High-resolution atomic-force microscopy of DNA: the pitch of the double helix. *FEBS Lett* **371**, 279–282 (1995).
125. Lyubchenko, Y., Shlyakhtenko, L., Harrington, R., Oden, P. & Lindsay, S. Atomic force microscopy of long DNA: imaging in air and under water. *Proc Natl Acad Sci U S A* **90**, 2137–2140 (1993).
126. Lindsay, S. M., Lyubchenko, Y. L., Gall, A. S., Shlyakhtenko, L. S. & Harrington, R. E. Imaging DNA molecules chemically bound to a mica surface. in *Scanning Probe Microscopies* vol. 1639 84–90 (SPIE, 1992).
127. Lyubchenko, Y. L., Oden, P. I., Lampner, D., Lindsay, S. M. & Dunker, K. A. Atomic force microscopy of DNA and bacteriophage in air, water and propanol: the role of adhesion forces. *Nucleic Acids Res* **21**, 1117–1123 (1993).

128. Lyubchenko, Y. L., Shlyakhtenko, L. S. & Gall, A. A. Atomic force microscopy imaging and probing of DNA, proteins, and protein DNA complexes: silatrane surface chemistry. *Methods Mol Biol* **543**, 337–351 (2009).
129. Shlyakhtenko, L. S. *et al.* Silatrane-based surface chemistry for immobilization of DNA, protein-DNA complexes and other biological materials. *Ultramicroscopy* **97**, 279–287 (2003).
130. Shlyakhtenko, L. S., Potaman, V. N., Sinden, R. R., Gall, A. A. & Lyubchenko, Y. L. Structure and dynamics of three-way DNA junctions: atomic force microscopy studies. *Nucleic Acids Res* **28**, 3472–3477 (2000).
131. Tiner, W. J., Potaman, V. N., Sinden, R. R. & Lyubchenko, Y. L. The structure of intramolecular triplex DNA: atomic force microscopy study¹¹Edited by I. Tinoco. *Journal of Molecular Biology* **314**, 353–357 (2001).
132. Seeman, N. C. & Sleiman, H. F. DNA nanotechnology. *Nature Reviews Materials* **3**, 17068 (2017).
133. Seeman, N. C. Nucleic acid junctions and lattices. *Journal of Theoretical Biology* **99**, 237–247 (1982).
134. Kallenbach, N. R., Ma, R.-I. & Seeman, N. C. An immobile nucleic acid junction constructed from oligonucleotides. *Nature* **305**, 829–831 (1983).
135. He, Y., Chen, Y., Liu, H., Ribbe, A. E. & Mao, C. Self-Assembly of Hexagonal DNA Two-Dimensional (2D) Arrays. *J. Am. Chem. Soc.* **127**, 12202–12203 (2005).
136. Kilchherr, F. *et al.* Single-molecule dissection of stacking forces in DNA. *Science* **353**, aaf5508 (2016).
137. Burley, S. K. & Petsko, G. A. Aromatic-Aromatic Interaction: A Mechanism of Protein Structure Stabilization. *Science* **229**, 23–28 (1985).

138. Rutledge, L. R., Campbell-Verduyn, L. S. & Wetmore, S. D. Characterization of the stacking interactions between DNA or RNA nucleobases and the aromatic amino acids. *Chemical Physics Letters* **444**, 167–175 (2007).
139. Chen, J. & Seeman, N. C. Synthesis from DNA of a molecule with the connectivity of a cube. *Nature* **350**, 631–633 (1991).
140. Ke, Y., Ong, L. L., Shih, W. M. & Yin, P. Three-Dimensional Structures Self-Assembled from DNA Bricks. *Science* **338**, 1177–1183 (2012).
141. Yan, X., Huang, S., Wang, Y., Tang, Y. & Tian, Y. Bottom-Up Self-Assembly Based on DNA Nanotechnology. *Nanomaterials* **10**, 2047 (2020).
142. Guthold, M. *et al.* Following the assembly of RNA polymerase-DNA complexes in aqueous solutions with the scanning force microscope. *Proc Natl Acad Sci U S A* **91**, 12927–12931 (1994).
143. Crampton, N. *et al.* Fast-scan atomic force microscopy reveals that the type III restriction enzyme EcoP15I is capable of DNA translocation and looping. *Proc Natl Acad Sci U S A* **104**, 12755–12760 (2007).
144. Kaur, P. *et al.* High-speed AFM imaging reveals DNA capture and loop extrusion dynamics by cohesin-NIPBL. *Journal of Biological Chemistry* **299**, 105296 (2023).
145. Kielar, C., Ramakrishnan, S., Fricke, S., Grundmeier, G. & Keller, A. Dynamics of DNA Origami Lattice Formation at Solid–Liquid Interfaces. *ACS Appl. Mater. Interfaces* **10**, 44844–44853 (2018).
146. Suzuki, Y., Endo, M., Yang, Y. & Sugiyama, H. Dynamic Assembly/Disassembly Processes of Photoresponsive DNA Origami Nanostructures Directly Visualized on a Lipid Membrane Surface. *J. Am. Chem. Soc.* **136**, 1714–1717 (2014).

147. Nievergelt, A. P. *et al.* Large-Range HS-AFM Imaging of DNA Self-Assembly through In Situ Data-Driven Control. *Small Methods* **3**, 1900031 (2019).
148. Rossi-Gendron, C. *et al.* Isothermal self-assembly of multicomponent and evolutive DNA nanostructures. *Nat. Nanotechnol.* **18**, 1311–1318 (2023).
149. Lutsko, J. F. How crystals form: A theory of nucleation pathways. *Science Advances* **5**, eaav7399 (2019).
150. Jun, Y.-S. *et al.* Classical and Nonclassical Nucleation and Growth Mechanisms for Nanoparticle Formation. *Annual Review of Physical Chemistry* **73**, 453–477 (2022).
151. Yang, Y. *et al.* A self-standing three-dimensional covalent organic framework film. *Nat Commun* **14**, 220 (2023).
152. Yuan, C. *et al.* Hierarchically oriented organization in supramolecular peptide crystals. *Nature Reviews Chemistry* **3**, 567–588 (2019).
153. De Yoreo, J. J. *et al.* Crystallization by particle attachment in synthetic, biogenic, and geologic environments. *Science* **349**, aaa6760 (2015).
154. Kuznetsov, Yu. G., Malkin, A. J. & McPherson, A. AFM studies of the nucleation and growth mechanisms of macromolecular crystals. *Journal of Crystal Growth* **196**, 489–502 (1999).
155. Rubbo, M. Basic concepts in crystal growth. *Crystal Research and Technology* **48**, 676–705 (2013).
156. Puri, S. Kinetics of Phase Transitions. in *Kinetics of Phase Transitions* (CRC Press, 2009).
157. Caroprese, V. *et al.* Structural flexibility dominates over binding strength for supramolecular crystallinity. 2023.09.04.556250 Preprint at <https://doi.org/10.1101/2023.09.04.556250> (2023).

158. Judge, R. A., Jacobs, R. S., Frazier, T., Snell, E. H. & Pusey, M. L. The Effect of Temperature and Solution pH on the Nucleation of Tetragonal Lysozyme Crystals. *Biophysical Journal* **77**, 1585–1593 (1999).
159. Botsaris, G. D. Secondary Nucleation — A Review. in *Industrial Crystallization* (ed. Mullin, J. W.) 3–22 (Springer US, Boston, MA, 1976). doi:10.1007/978-1-4615-7258-9_1.
160. Lindenmeyer, P. H. Surface area and secondary nucleation theory. *Nature* **269**, 396–397 (1977).
161. Linse, S. Monomer-dependent secondary nucleation in amyloid formation. *Biophys Rev* **9**, 329–338 (2017).
162. Karthika, S., Radhakrishnan, T. K. & Kalaichelvi, P. A Review of Classical and Nonclassical Nucleation Theories. *Crystal Growth & Design* **16**, 6663–6681 (2016).
163. Leubner, I. H. Particle nucleation and growth models. *Current Opinion in Colloid & Interface Science* **5**, 151–159 (2000).
164. Van Leeuwen, C. & Van Der Eerden, J. P. Nucleation growth processes: A Monte Carlo simulation. *Surface Science* **64**, 237–250 (1977).
165. Zeng, C., Vitale-Sullivan, C. & Ma, X. In Situ Atomic Force Microscopy Studies on Nucleation and Self-Assembly of Biogenic and Bio-Inspired Materials. *Minerals* **7**, 158 (2017).
166. KADLER, K. E., HOLMES, D. F., TROTTER, J. A. & CHAPMAN, J. A. Collagen fibril formation. *Biochemical Journal* **316**, 1–11 (1996).
167. Cisneros, D. A., Hung, C., Franz, C. M. & Muller, D. J. Observing growth steps of collagen self-assembly by time-lapse high-resolution atomic force microscopy. *Journal of Structural Biology* **154**, 232–245 (2006).

168. Gisbert, V. G., Benaglia, S., Uhlig, M. R., Proksch, R. & Garcia, R. High-Speed Nanomechanical Mapping of the Early Stages of Collagen Growth by Bimodal Force Microscopy. *ACS Nano* **15**, 1850–1857 (2021).
169. Lehto, T., Miaczynska, M., Zerial, M., Müller, D. J. & Severin, F. Observing the growth of individual actin filaments in cell extracts by time-lapse atomic force microscopy. *FEBS Letters* **551**, 25–28 (2003).
170. Fukuda, S. & Ando, T. Faster high-speed atomic force microscopy for imaging of biomolecular processes. *Review of Scientific Instruments* **92**, 033705 (2021).
171. Wijeratne, S. S., Marchan, M. F., Tresback, J. S. & Subramanian, R. Atomic force microscopy reveals distinct protofilament-scale structural dynamics in depolymerizing microtubule arrays. *Proceedings of the National Academy of Sciences* **119**, e2115708119 (2022).
172. Müller, K. M., Arndt, K. M. & Plückthun, A. Model and Simulation of Multivalent Binding to Fixed Ligands. *Analytical Biochemistry* **261**, 149–158 (1998).
173. Bruncsics, B., Errington, W. J. & Sarkar, C. A. MVsim is a toolset for quantifying and designing multivalent interactions. *Nat Commun* **13**, 5029 (2022).
174. Lei, K. *et al.* Cancer-cell stiffening via cholesterol depletion enhances adoptive T-cell immunotherapy. *Nat Biomed Eng* **5**, 1411–1425 (2021).
175. Ando, T. High-speed atomic force microscopy and its future prospects. *Biophys Rev* **10**, 285–292 (2017).
176. Uchihashi, T. & Scheuring, S. Applications of high-speed atomic force microscopy to real-time visualization of dynamic biomolecular processes. *Biochim Biophys Acta Gen Subj* **1862**, 229–240 (2018).

177. Eghiaian, F., Rico, F., Colom, A., Casuso, I. & Scheuring, S. High-speed atomic force microscopy: Imaging and force spectroscopy. *FEBS Letters* **588**, 3631–3638 (2014).
178. Umeda, K., McArthur, S. J. & Kodera, N. Spatiotemporal resolution in high-speed atomic force microscopy for studying biological macromolecules in action. *Microscopy* **72**, 151–161 (2023).
179. Nievergelt, A. P., Banterle, N., Andany, S. H., Gönczy, P. & Fantner, G. E. High-speed photothermal off-resonance atomic force microscopy reveals assembly routes of centriolar scaffold protein SAS-6. *Nat Nanotechnol* **13**, 696–701 (2018).
180. Heath, G. R. & Scheuring, S. High-speed AFM height spectroscopy reveals μ s-dynamics of unlabeled biomolecules. *Nat Commun* **9**, 1–11 (2018).
181. *High-Speed Atomic Force Microscopy in Biology*.
182. Jiao, F., Cannon, K. S., Lin, Y.-C., Gladfelter, A. S. & Scheuring, S. The hierarchical assembly of septins revealed by high-speed AFM. *Nature Communications* **11**, 5062 (2020).
183. PeakForce Tapping. <https://www.bruker.com/en/products-and-solutions/microscopes/materials-afm/afm-modes/peakforce-tapping.html>.
184. Wang, S. & Hao, C. Principle and Application of Peak Force Tapping Mode Atomic Force Microscope. in *International Conference on Cognitive based Information Processing and Applications (CIPA 2021)* (eds. J. Jansen, B., Liang, H. & Ye, J.) 671–679 (Springer, Singapore, 2022). doi:10.1007/978-981-16-5854-9_86.
185. Avakyan, N., Conway, J. W. & Sleiman, H. F. Long-Range Ordering of Blunt-Ended DNA Tiles on Supported Lipid Bilayers. *J. Am. Chem. Soc.* **139**, 12027–12034 (2017).
186. Wang, R., Kuzuya, A., Liu, W. & C. Seeman, N. Blunt-ended DNA stacking interactions in a 3-helix motif. *Chemical Communications* **46**, 4905–4907 (2010).

187. Parikka, J. M., Sokołowska, K., Markešević, N. & Toppari, J. J. Constructing Large 2D Lattices Out of DNA-Tiles. *Molecules* **26**, 1502 (2021).
188. Lipid-DNA Method.
http://sabatini.wi.mit.edu/sabatini_public/reverse_transfection/lipid_dna_method.htm.
189. Pyne, A. L. B. *et al.* Base-pair resolution analysis of the effect of supercoiling on DNA flexibility and major groove recognition by triplex-forming oligonucleotides. *Nat Commun* **12**, 1053 (2021).
190. Vincenzo Caroprese *et al.* Structural flexibility dominates over binding strength for supramolecular crystallinity. *bioRxiv* 2023.09.04.556250 (2023)
doi:10.1101/2023.09.04.556250.
191. Components for high-speed atomic force microscopy optimized for low phase-lag | IEEE Conference Publication | IEEE Xplore. <https://ieeexplore.ieee.org/document/8014104>.
192. SPM Controller/Software. EPFL <https://www.epfl.ch/labs/lbni/spm-controller-software/>.
193. Open Hardware. EPFL <https://www.epfl.ch/labs/lbni/openhardware/>.
194. AFM head for small cantilevers, with photothermal drive. EPFL
<https://www.epfl.ch/labs/lbni/smallleverhead/>.
195. BioLever. *AppNano* <https://www.appnano.com/product-page/biolever>.
196. Gwyddion – Pygwy tutorial. <http://gwyddion.net/documentation/pygwy.php>.
197. Stahl, S. W., Puchner, E. M. & Gaub, H. E. Photothermal cantilever actuation for fast single-molecule force spectroscopy. *Review of Scientific Instruments* **80**, 073702 (2009).
198. Kangül, M., Asmari, N., Andany, S. H., Penedo, M. & Fantner, G. E. Enhanced feedback performance in off-resonance AFM modes through pulse train sampling. Preprint at <https://doi.org/10.48550/arXiv.2306.16013> (2023).

199. Giessibl, F. J. Advances in atomic force microscopy. *Rev. Mod. Phys.* **75**, 949–983 (2003).
200. Ando, T. High-Speed Atomic Force Microscopy (AFM). in *Encyclopedia of Biophysics* (ed. Roberts, G. C. K.) 984–987 (Springer, Berlin, Heidelberg, 2013). doi:10.1007/978-3-642-16712-6_478.
201. Vekilov, P. G. Nucleation. *Crystal Growth & Design* **10**, 5007–5019 (2010).
202. Vekilov, P. G. Phase diagrams and kinetics of phase transitions in protein solutions. *J. Phys.: Condens. Matter* **24**, 193101 (2012).
203. Puri, S. Kinetics of Phase Transitions. *Phase Transitions* **77**, 407–431 (2004).
204. Yang, Y. *et al.* A self-standing three-dimensional covalent organic framework film. *Nat Commun* **14**, 220 (2023).
205. Yuan, C. *et al.* Hierarchically oriented organization in supramolecular peptide crystals. *Nat Rev Chem* **3**, 567–588 (2019).
206. De Yoreo, J. J. *et al.* Crystallization by particle attachment in synthetic, biogenic, and geologic environments. *Science* **349**, aaa6760 (2015).
207. Stupp, S. I. *et al.* Supramolecular Materials: Self-Organized Nanostructures. *Science* **276**, 384–389 (1997).
208. Malshe, A. *et al.* Bio-inspired functional surfaces for advanced applications. *CIRP Annals* **62**, 607–628 (2013).
209. Ferguson, M. L. *et al.* Clathrin Triskelia Show Evidence of Molecular Flexibility. *Biophysical Journal* **95**, 1945–1955 (2008).
210. Morris, K. L. *et al.* Cryo-EM of multiple cage architectures reveals a universal mode of clathrin self-assembly. *Nat Struct Mol Biol* **26**, 890–898 (2019).

211. Paraan, M. *et al.* The structures of natively assembled clathrin-coated vesicles. *Sci. Adv.* **6**, eaba8397 (2020).
212. Yu, A. *et al.* TRIM5 α self-assembly and compartmentalization of the HIV-1 viral capsid. *Nat Commun* **11**, 1307 (2020).
213. Kiessling, L. L., Strong, L. E. & Gestwicki, J. E. Principles for multivalent ligand design. *Annual Reports in Medicinal Chemistry, Vol 35* **35**, 321–330 (2000).
214. Varshey, D. B., Sander, J. R. G., Friščić, T. & MacGillivray, L. R. Supramolecular Interactions. in *Supramolecular Chemistry* (eds. Gale, P. A. & Steed, J. W.) smc003 (John Wiley & Sons, Ltd, Chichester, UK, 2012). doi:10.1002/9780470661345.smc003.
215. Pyles, H., Zhang, S., De Yoreo, J. J. & Baker, D. Controlling protein assembly on inorganic crystals through designed protein interfaces. *Nature* **571**, 251–256 (2019).
216. Zhang, S., Alberstein, R. G., De Yoreo, J. J. & Tezcan, F. A. Assembly of a patchy protein into variable 2D lattices via tunable multiscale interactions. *Nat Commun* **11**, 3770 (2020).
217. Ben-Sasson, A. J. *et al.* Design of biologically active binary protein 2D materials. *Nature* **589**, 468–473 (2021).
218. Zhang, T., Lyu, D., Xu, W., Mu, Y. & Wang, Y. Programming Self-Assembled Materials With DNA-Coated Colloids. *Front. Phys.* **9**, 672375 (2021).
219. Wang, Y. *et al.* Synthetic Strategies Toward DNA-Coated Colloids that Crystallize. *J. Am. Chem. Soc.* **137**, 10760–10766 (2015).
220. Vilanova, N., De Feijter, I. & Voets, I. K. Synthesis and Characterization of Supramolecular Colloids. *JoVE* 53934 (2016) doi:10.3791/53934.
221. Mitchell, J. S., Glowacki, J., Grandchamp, A. E., Manning, R. S. & Maddocks, J. H. Sequence-Dependent Persistence Lengths of DNA. *J. Chem. Theory Comput.* **13**, 1539–1555 (2017).

222. Wei, B., Dai, M. & Yin, P. Complex shapes self-assembled from single-stranded DNA tiles. *Nature* **485**, 623–626 (2012).
223. Xin, Y. *et al.* Environment-Dependent Stability and Mechanical Properties of DNA Origami Six-Helix Bundles with Different Crossover Spacings. *Small* **18**, 2107393 (2022).
224. He, Y. *et al.* Hierarchical self-assembly of DNA into symmetric supramolecular polyhedra. *Nature* **452**, 198-U41 (2008).
225. He, Y., Chen, Y., Liu, H., Ribbe, A. E. & Mao, C. Self-Assembly of Hexagonal DNA Two-Dimensional (2D) Arrays. *J. Am. Chem. Soc.* **127**, 12202–12203 (2005).
226. Nievergelt, A. P. *et al.* Large-Range HS-AFM Imaging of DNA Self-Assembly through In Situ Data-Driven Control. *Small Methods* **3**, 1900031 (2019).
227. Avakyan, N., Conway, J. W. & Sleiman, H. F. Long-Range Ordering of Blunt-Ended DNA Tiles on Supported Lipid Bilayers. *J. Am. Chem. Soc.* **139**, 12027–12034 (2017).
228. The MathWorks Inc. (2022). Statistics and Machine Learning Toolbox Documentation, Natick, Massachusetts: The MathWorks Inc.
229. Friedkin, N. E. The development of structure in random networks: an analysis of the effects of increasing network density on five measures of structure. *Social Networks* **3**, 41–52 (1981).
230. Ando, T. High-speed atomic force microscopy and its future prospects. *Biophys Rev* **10**, 285–292 (2018).
231. Ando, T. *High-Speed Atomic Force Microscopy in Biology: Directly Watching Dynamics of Biomolecules in Action*. (Springer Berlin Heidelberg, Berlin, Heidelberg, 2022). doi:10.1007/978-3-662-64785-1.

232. Nievergelt, A. P., Banterle, N., Andany, S. H., Gönczy, P. & Fantner, G. E. High-speed photothermal off-resonance atomic force microscopy reveals assembly routes of centriolar scaffold protein SAS-6. *Nature Nanotech* **13**, 696–701 (2018).
233. Ouldrige, T. E., Louis, A. A. & Doye, J. P. K. Structural, mechanical, and thermodynamic properties of a coarse-grained DNA model. *The Journal of Chemical Physics* **134**, 085101 (2011).
234. Snodin, B. E. K. *et al.* Introducing improved structural properties and salt dependence into a coarse-grained model of DNA. *The Journal of Chemical Physics* **142**, 234901 (2015).
235. Frenkel, D., Smit, B. & Ratner, M. A. *Understanding Molecular Simulation: From Algorithms to Applications*. *Physics Today* **50**, 66–66 (1997).
236. Pawar, A. B. & Kretzschmar, I. Fabrication, Assembly, and Application of Patchy Particles: Fabrication, Assembly, and Application *Macromol. Rapid Commun.* **31**, 150–168 (2010).
237. Doye, J. P. K. *et al.* Controlling crystallization and its absence: proteins, colloids and patchy models. *Physical Chemistry Chemical Physics* **9**, 2197–2205 (2007).
238. Reinhardt, A., Schreck, J. S., Romano, F. & Doye, J. P. K. Self-assembly of two-dimensional binary quasicrystals: a possible route to a DNA quasicrystal. *J. Phys.: Condens. Matter* **29**, 014006 (2017).
239. Rovigatti, L., Russo, J. & Romano, F. How to simulate patchy particles. *Eur. Phys. J. E* **41**, 59 (2018).
240. Kern, N. & Frenkel, D. Fluid-fluid coexistence in colloidal systems with short-ranged strongly directional attraction. *Journal of Chemical Physics* **118**, 9882–9889 (2003).
241. Ising, E. Beitrag zur Theorie des Ferromagnetismus. *Z. Physik* **31**, 253–258 (1925).
242. Brush, S. G. History of the Lenz-Ising Model. *Rev. Mod. Phys.* **39**, 883–893 (1967).

243. Rovigatti, L., de las Heras, D., Tavares, J. M., Telo da Gama, M. M. & Sciortino, F. Computing the phase diagram of binary mixtures: A patchy particle case study. *The Journal of Chemical Physics* **138**, 164904 (2013).
244. Witten, T. A. & Sander, L. M. Diffusion-Limited Aggregation, a Kinetic Critical Phenomenon. *Phys. Rev. Lett.* **47**, 1400–1403 (1981).
245. Hurd, A. J. & Schaefer, D. W. Diffusion-Limited Aggregation in Two Dimensions. *Phys. Rev. Lett.* **54**, 1043–1046 (1985).
246. Vicsek, T. Pattern Formation in Diffusion-Limited Aggregation. *Phys. Rev. Lett.* **53**, 2281–2284 (1984).
247. Benson, E. *et al.* DNA rendering of polyhedral meshes at the nanoscale. *Nature* **523**, 441–444 (2015).
248. Autodesk, INC. Maya [Internet]. 2019. Available from: <https://autodesk.com/maya>.
249. Suma, A. *et al.* TacoxDNA: A user-friendly web server for simulations of complex DNA structures, from single strands to origami. *J Comput Chem* **40**, 2586–2595 (2019).
250. Poppleton, E. *et al.* Design, optimization and analysis of large DNA and RNA nanostructures through interactive visualization, editing and molecular simulation. *Nucleic Acids Research* **48**, e72–e72 (2020).
251. Bohlin, J. *et al.* Design and simulation of DNA, RNA and hybrid protein–nucleic acid nanostructures with oxView. *Nat Protoc* **17**, 1762–1788 (2022).
252. Humphrey, W., Dalke, A. & Schulten, K. VMD: Visual molecular dynamics. *Journal of Molecular Graphics* **14**, 33–38 (1996).
253. http://www.ks.uiuc.edu/Research/vmd/mailling_list/vmd-l/att-32062/system_freeze.vmd.
254. <http://vmmc.xyz/>.

255. Humphrey, J. D., Dufresne, E. R. & Schwartz, M. A. Mechanotransduction and extracellular matrix homeostasis. *Nature Reviews Molecular Cell Biology* **15**, 802–812 (2014).
256. Yeh, Y., Ling, J., Chen, W., Lin, H. & Tang, M. Mechanotransduction of matrix stiffness in regulation of focal adhesion size and number : reciprocal regulation of caveolin-1 and β 1 integrin. *Scientific Reports* **7**, 1–14 (2017).
257. Balestrini, J. L. & Niklason, L. E. Extracellular Matrix as a Driver for Lung Regeneration. *Annals of Biomedical Engineering* **43**, 568–576 (2014).
258. Handorf, A. M., Zhou, Y., Halanski, M. A. & Li, W. J. Tissue stiffness dictates development, homeostasis, and disease progression. *Organogenesis* **11**, 1–15 (2015).
259. Huh, D., Matthews, B.D., Mammoto, A., Montoya-Zavala, M., Yuan Hsin, H., Ingber, D. E. Reconstituting Organ-Level Lung. *Science* **328**, 1662–1668 (2010).
260. Stucki, J. D. *et al.* Medium throughput breathing human primary cell alveolus-on- chip model. *Scientific Reports* **8**, 1–13 (2018).
261. Lind, J. U. *et al.* Instrumented cardiac microphysiological devices via multimaterial three-dimensional printing. *Nature Materials* **16**, 303–308 (2017).
262. Marsano, A. *et al.* Beating heart on a chip: A novel microfluidic platform to generate functional 3D cardiac microtissues. *Lab on a Chip* **16**, 599–610 (2016).
263. Tanyeri, M. & Tay, S. Viable cell culture in PDMS-based microfluidic devices. *Methods in Cell Biology* **148**, 3–33 (2018).
264. Toepke, M. W. & Beebe, D. J. PDMS absorption of small molecules and consequences in microfluidic applications. *Lab on a Chip* **6**, 1484–1486 (2006).
265. van Meer, B. J. *et al.* Small molecule absorption by PDMS in the context of drug response bioassays. *Biochemical and Biophysical Research Communications* **482**, 323–328 (2017).

266. Mondrinos, M. J., Yi, Y. S., Wu, N. K., Ding, X. & Huh, D. Native extracellular matrix-derived semipermeable, optically transparent, and inexpensive membrane inserts for microfluidic cell culture. *Lab on a Chip* **17**, 3146–3158 (2017).
267. Zamprogno, A. P., Wüthrich, S., Achenbach, S. & Stucki, J. D. Second - generation lung - on - a - chip array with a stretchable biological membrane. *bioRxiv* (2019).
268. Lee, J. S. *et al.* Placenta-on-a-chip: a novel platform to study the biology of the human placenta. *The Journal of Maternal-Fetal & Neonatal Medicine* **00**, 1–9 (2015).
269. Wang, C., Tanataweethum, N., Karnik, S. & Bhushan, A. Novel Microfluidic Colon with an Extracellular Matrix Membrane. *ACS Biomater. Sci. Eng.* **4**, 1377–1385 (2018).
270. Dong, C. & Lv, Y. Application of collagen scaffold in tissue engineering: Recent advances and new perspectives. *Polymers* **8**, 1–20 (2016).
271. Miranda-Nieves, D. & Chaikof, E. L. Collagen and Elastin Biomaterials for the Fabrication of Engineered Living Tissues. *ACS Biomaterials Science and Engineering* **3**, 694–711 (2017).
272. Krieg, M. *et al.* Atomic force microscopy-based mechanobiology. *Nature Reviews Physics* **1**, 41–57 (2019).
273. Nehls, S. & Janshoff, A. Elastic Properties of Pore-Spanning Apical Cell Membranes Derived from MDCK II Cells. *Biophysical Journal* **113**, 1822–1830 (2017).
274. Gonçalves, R. P. *et al.* Two-chamber AFM: Probing membrane proteins separating two aqueous compartments. *Nature Methods* **3**, 1007–1012 (2006).
275. Sheng, J. Y., Zhang, L. Y., Li, B., Wang, G. F. & Feng, X. Q. Bulge test method for measuring the hyperelastic parameters of soft membranes. *Acta Mechanica* **228**, 4187–4197 (2017).
276. Kraft, O. & Volkert, C. A. Mechanical testing of thin films and small structures. *Advanced Engineering Materials* **3**, 99–110 (2001).

277. Small, M. K. & Nix, W. D. Analysis of the accuracy of the bulge test in determining the mechanical properties of thin films. *Journal of Materials Research* **7**, 1553–1563 (1992).
278. Huang, C. K., Lou, W. M., Tsai, C. J., Wu, T. C. & Lin, H. Y. Mechanical properties of polymer thin film measured by the bulge test. *Thin Solid Films* **515**, 7222–7226 (2007).
279. Gao, J., Guo, D., Santhanam, S. & Fedder, G. K. Material Characterization and Transfer of Large-Area Ultra-Thin Polydimethylsiloxane Membranes. *Journal of Microelectromechanical Systems* **24**, 2170–2177 (2015).
280. Zamprogno, A. P., Wüthrich, S., Achenbach, S. & Stucki, J. D. Second - generation lung - on - a - chip array with a stretchable biological membrane. *bioRxiv* (2019).
281. Odermatt, P. D. *et al.* High-Resolution Correlative Microscopy: Bridging the Gap between Single Molecule Localization Microscopy and Atomic Force Microscopy. *Nano Letters* **15**, 4896–4904 (2015).
282. Frantz, C., Stewart, K. M. & Weaver, V. M. The extracellular matrix at a glance. *Journal of cell science* **123**, 4195–200 (2010).
283. Burgstaller, G. *et al.* The instructive extracellular matrix of the lung: Basic composition and alterations in chronic lung disease. *European Respiratory Journal* **50**, (2017).
284. Dunphy, S. E., Bratt, J. A. J., Akram, K. M., Forsyth, N. R. & El Haj, A. J. Hydrogels for lung tissue engineering: Biomechanical properties of thin collagen-elastin constructs. *Journal of the Mechanical Behavior of Biomedical Materials* **38**, 251–259 (2014).
285. Humayun, M., Chow, C. W. & Young, E. W. K. Microfluidic lung airway-on-a-chip with arrayable suspended gels for studying epithelial and smooth muscle cell interactions. *Lab on a Chip* **18**, 1298–1309 (2018).

286. Discher, D. E., Janmey, P. & Wang, Y. Tissue Cells Feel and Respond to the Stiffness of Their Substrate. *Science* **30**, 1139–1143 (2005).
287. Chang, Y. R. *et al.* Automated AFM force curve analysis for determining elastic modulus of biomaterials and biological samples. *Journal of the Mechanical Behavior of Biomedical Materials* **37**, 209–218 (2014).
288. McBane, J. E. *et al.* Evaluation of a Collagen-Chitosan Hydrogel for Potential Use as a Pro-Angiogenic Site for Islet Transplantation. *PLoS ONE* **8**, 1–15 (2013).
289. Ahearne, M., Yang, Y., Then, K. Y. & Liu, K. K. Non-destructive mechanical characterisation of UVA/riboflavin crosslinked collagen hydrogels. *British Journal of Ophthalmology* **92**, 268–271 (2008).
290. Joshi, J., Mahajan, G. & Kothapalli, C. R. Three-dimensional collagenous niche and azacytidine selectively promote time-dependent cardiomyogenesis from human bone marrow-derived MSC spheroids. *Biotechnology and Bioengineering* **115**, 2013–2026 (2018).
291. Elibol, K. *et al.* Visualising the strain distribution in suspended two-dimensional materials under local deformation. *Scientific Reports* **6**, 1–9 (2016).
292. Elibol, K., Hummel, S., Bayer, B. C. & Meyer, J. C. New imaging modes for analyzing suspended ultra-thin membranes by double-tip scanning probe microscopy. *Scientific Reports* **10**, 1–14 (2020).
293. Antoine, E. E., Vlachos, P. P. & Rylander, M. N. Review of collagen i hydrogels for bioengineered tissue microenvironments: Characterization of mechanics, structure, and transport. *Tissue Engineering - Part B: Reviews* **20**, 683–696 (2014).
294. Holder, A. J. *et al.* Control of collagen gel mechanical properties through manipulation of gelation conditions near the sol-gel transition. *Soft Matter* **14**, 574–580 (2018).

295. Raub, C. B. *et al.* Noninvasive assessment of collagen gel microstructure and mechanics using multiphoton microscopy. *Biophysical Journal* **92**, 2212–2222 (2007).
296. Achilli, M. & Mantovani, D. Tailoring mechanical properties of collagen-based scaffolds for vascular tissue engineering: The effects of pH, temperature and ionic strength on gelation. *Polymers* **2**, 664–680 (2010).
297. Leipzig, N. D. & Shoichet, M. S. The effect of substrate stiffness on adult neural stem cell behavior. *Biomaterials* **30**, 6867–6878 (2009).
298. Nawroth, J. C. *et al.* Stem cell-based Lung-on-Chips: The best of both worlds? *Advanced Drug Delivery Reviews* **140**, 12–32 (2019).
299. Engler, A. J., Rehfeldt, F., Sen, S. & Discher, D. E. Microtissue Elasticity: Measurements by Atomic Force Microscopy and Its Influence on Cell Differentiation. *Methods in Cell Biology* **83**, 521–545 (2007).
300. Hinz, B. Mechanical aspects of lung fibrosis: A spotlight on the myofibroblast. *Proceedings of the American Thoracic Society* **9**, 137–147 (2012).
301. Prager-Khoutorsky, M. *et al.* Fibroblast polarization is a matrix-rigidity-dependent process controlled by focal adhesion mechanosensing. *Nat Cell Biol* **13**, 1457–1465 (2011).
302. Mih, J. D. *et al.* A multiwell platform for studying stiffness-dependent cell biology. *PLoS ONE* **6**, 1–10 (2011).
303. Shkumatov, A. *et al.* Matrix stiffness-modulated proliferation and secretory function of the airway smooth muscle cells. *American Journal of Physiology - Lung Cellular and Molecular Physiology* **308**, L1125–L1135 (2015).
304. Yeung, T. *et al.* Effects of substrate stiffness on cell morphology, cytoskeletal structure, and adhesion. *Cell Motility and the Cytoskeleton* **60**, 24–34 (2005).

305. Plotnikov, S. V., Pasapera, A. M., Sabass, B. & Waterman, C. M. Force fluctuations within focal adhesions mediate ECM-rigidity sensing to guide directed cell migration. *Cell*. **151**, 1513–1527 (2012).
306. Steward, A. J. & Kelly, D. J. Mechanical regulation of mesenchymal stem cell differentiation. *Journal of Anatomy* **227**, 717–731 (2015).
307. Yang, C., Tibbitt, M. W., Basta, L. & Anseth, K. S. Mechanical memory and dosing influence stem cell fate. *Nature Materials* **13**, 645–652 (2014).
308. Mih, J. D., Marinkovic, A., Liu, F., Sharif, A. S. & Tschumperlin, D. J. Matrix stiffness reverses the effect of actomyosin tension on cell proliferation. *Journal of Cell Science* **125**, 5974–5983 (2012).
309. Penedo, M. *et al.* Visualizing intracellular nanostructures of living cells by nanoendoscopy-AFM. *Science Advances* **7**, eabj4990 (2021).
310. Kaksonen, M. & Roux, A. Mechanisms of clathrin-mediated endocytosis. *Nature Reviews Molecular Cell Biology* **19**, 313–326 (2018).
311. Kirchhausen, T. IMAGING ENDOCYTIC CLATHRIN STRUCTURES IN LIVING CELLS. *Trends Cell Biol* **19**, 596–605 (2009).
312. Lampe, M., Vassilopoulos, S. & Merrifield, C. Clathrin coated pits, plaques and adhesion. *Journal of Structural Biology* **196**, 48–56 (2016).
313. Saleem, M. *et al.* A balance between membrane elasticity and polymerization energy sets the shape of spherical clathrin coats. *Nature Communications* **6**, 6249 (2015).
314. Saffarian, S., Cocucci, E. & Kirchhausen, T. Distinct Dynamics of Endocytic Clathrin-Coated Pits and Coated Plaques. *PLOS Biology* **7**, e1000191 (2009).

315. Rodal, S. K. *et al.* Extraction of Cholesterol with Methyl- β -Cyclodextrin Perturbs Formation of Clathrin-coated Endocytic Vesicles. *MBoC* **10**, 961–974 (1999).
316. Anderson, R. H. *et al.* Sterols lower energetic barriers of membrane bending and fission necessary for efficient clathrin mediated endocytosis. *bioRxiv* 2021.01.31.428633 (2021) doi:10.1101/2021.01.31.428633.
317. Subtil, A. *et al.* Acute cholesterol depletion inhibits clathrin-coated pit budding. *Proc Natl Acad Sci U S A* **96**, 6775–6780 (1999).
318. Pearse, B. M. Clathrin: a unique protein associated with intracellular transfer of membrane by coated vesicles. *Proc Natl Acad Sci U S A* **73**, 1255–1259 (1976).
319. Le Grimmellec, C. *et al.* Imaging of the cytoplasmic leaflet of the plasma membrane by atomic force microscopy. *Scanning Microsc* **9**, 401–410; discussion 410-411 (1995).
320. Frankel, D. J. *et al.* Revealing the Topography of Cellular Membrane Domains by Combined Atomic Force Microscopy/Fluorescence Imaging. *Biophysical Journal* **90**, 2404–2413 (2006).
321. Galvanetto, N. Single-cell unroofing: probing topology and nanomechanics of native membranes. *Biochimica et Biophysica Acta (BBA) - Biomembranes* **1860**, 2532–2538 (2018).
322. Sato, F., Asakawa, H., Fukuma, T. & Terada, S. Semi- *in situ* atomic force microscopy imaging of intracellular neurofilaments under physiological conditions through the ‘sandwich’ method. *Microscopy* **65**, 316–324 (2016).
323. Usukura, J. *et al.* Use of the unroofing technique for atomic force microscopic imaging of the intra-cellular cytoskeleton under aqueous conditions. *Journal of Electron Microscopy* **61**, 321–326 (2012).
324. Heuser, J. The Production of ‘Cell Cortices’ for Light and Electron Microscopy. *Traffic* **1**, 545–552 (2000).

325. Model 150VT - Sonicators - Ultrasonic Homogenizers - Cell Disruptor.
<https://ultrasonichomogenizer.com/ultrasonic-homogenizer-model-150vt.html>.
326. Usukura, E., Narita, A., Yagi, A., Ito, S. & Usukura, J. An Unroofing Method to Observe the Cytoskeleton Directly at Molecular Resolution Using Atomic Force Microscopy. *Scientific Reports* **6**, 27472 (2016).
327. Dimension Icon AFM. <https://www.bruker.com/en/products-and-solutions/microscopes/materials-afm/dimension-icon-afm.html>.
328. ScanAsyst-Fluid | Veeco Probes | Bruker AFM Probes. <https://www.brukerafmprobes.com/p-3727-scanasyst-fluid.aspx>.
329. Gwyddion – Free SPM (AFM, SNOM/NSOM, STM, MFM, ...) data analysis software.
<http://gwyddion.net/>.
330. Granseth, B., Odermatt, B., Royle, S. J. & Lagnado, L. Clathrin-Mediated Endocytosis Is the Dominant Mechanism of Vesicle Retrieval at Hippocampal Synapses. *Neuron* **51**, 773–786 (2006).
331. Sochacki, K. A. *et al.* The structure and spontaneous curvature of clathrin lattices at the plasma membrane. *bioRxiv* 2020.07.18.207258 (2020) doi:10.1101/2020.07.18.207258.
332. Grove, J. *et al.* Flat clathrin lattices: stable features of the plasma membrane. *Mol Biol Cell* **25**, 3581–3594 (2014).
333. Morone, N., Usukura, E., Narita, A. & Usukura, J. Improved unroofing protocols for cryo-electron microscopy, atomic force microscopy and freeze-etching electron microscopy and the associated mechanisms. *Microscopy (Oxf)* **69**, 350–359 (2020).

334. Adams, J. D., Frederix, P. L. T. M. & Bippes, C. A. Breakthrough instruments and products: DriveAFM for high-performance atomic force microscopy. *Review of Scientific Instruments* **92**, 129503 (2021).
335. Young, A. *et al.* Hsc70-induced Changes in Clathrin-Auxilin Cage Structure Suggest a Role for Clathrin Light Chains in Cage Disassembly. *Traffic* **14**, 987–996 (2013).
336. Xing, Y. *et al.* Structure of clathrin coat with bound Hsc70 and auxilin: mechanism of Hsc70-facilitated disassembly. *EMBO J* **29**, 655–665 (2010).
337. Eisenberg, E. & Greene, L. E. Multiple roles of auxilin and hsc70 in clathrin-mediated endocytosis. *Traffic* **8**, 640–646 (2007).
338. Chang, H. C. *et al.* Hsc70 is required for endocytosis and clathrin function in *Drosophila*. *J Cell Biol* **159**, 477–487 (2002).
339. Moskowitz, H. S., Heuser, J., McGraw, T. E. & Ryan, T. A. Targeted chemical disruption of clathrin function in living cells. *Mol Biol Cell* **14**, 4437–4447 (2003).
340. Jiang, R., Gao, B., Prasad, K., Greene, L. E. & Eisenberg, E. Hsc70 Chaperones Clathrin and Primes It to Interact with Vesicle Membranes*. *Journal of Biological Chemistry* **275**, 8439–8447 (2000).
341. Keyvani, A. *et al.* Real-Time Estimation of the Tip-Sample Interactions in Tapping Mode Atomic Force Microscopy With a Regularized Kalman Filter. *IEEE Transactions on Nanotechnology* **19**, 274–283 (2020).
342. Bahrami, M. R. Dynamic analysis of atomic force microscope in tapping mode. *Vibroengineering Procedia* **32**, 13–19 (2020).
343. Umeda, K. *et al.* Architecture of zero-latency ultrafast amplitude detector for high-speed atomic force microscopy. *Applied Physics Letters* **119**, 181602 (2021).

344. Park, B. *et al.* Dual-pulse photoactivated atomic force microscopy. *Sci Rep* **11**, 17097 (2021).
345. Tremoço, F. *et al.* Predicting sample heating induced by cantilevers illuminated by intense light beams. *Results in Physics* **39**, 105718 (2022).
346. Takahashi, H., Miyagi, A., Redondo-Morata, L. & Scheuring, S. Temperature-Controlled High-Speed AFM: Real-Time Observation of Ripple Phase Transitions. *Small* **12**, 6106–6113 (2016).
347. Fidorra, M., Heimburg, T. & Seeger, H. M. Melting of individual lipid components in binary lipid mixtures studied by FTIR spectroscopy, DSC and Monte Carlo simulations. *Biochimica et Biophysica Acta (BBA) - Biomembranes* **1788**, 600–607 (2009).
348. Phase Transition Temperatures for Glycerophospholipids. *Avanti Polar Lipids (en-US)* <https://avantilipids.com/tech-support/physical-properties/phase-transition-temps>.
349. Connell, S. D. & Smith, D. A. The atomic force microscope as a tool for studying phase separation in lipid membranes (Review). *Molecular Membrane Biology* **23**, 17–28 (2006).
350. Inada, N., Asakawa, H., Kobayashi, T. & Fukuma, T. Efficiency improvement in the cantilever photothermal excitation method using a photothermal conversion layer. *Beilstein J. Nanotechnol.* **7**, 409–417 (2016).
351. High-Speed AFM Measurements | Zurich Instruments. <https://www.zhinst.com/en/blogs/what-it-takes-high-speed-afm-measurements> (2021).
352. Nievergelt, A. P., Erickson, B. W., Hosseini, N., Adams, J. D. & Fantner, G. E. Studying biological membranes with extended range high-speed atomic force microscopy. *Scientific Reports* **5**, 11987 (2015).
353. Xu, K. *et al.* Recent development of PeakForce Tapping mode atomic force microscopy and its applications on nanoscience. *Nanotechnology Reviews* **7**, 605–621 (2018).

354. Jansen, R., Dzwolak, W. & Winter, R. Amyloidogenic Self-Assembly of Insulin Aggregates Probed by High Resolution Atomic Force Microscopy. *Biophysical Journal* **88**, 1344–1353 (2005).
355. Zhang, S. *et al.* Coexistence of ribbon and helical fibrils originating from hIAPP20–29 revealed by quantitative nanomechanical atomic force microscopy. *Proceedings of the National Academy of Sciences* **110**, 2798–2803 (2013).
356. Beton, J. G. *et al.* TopoStats – A program for automated tracing of biomolecules from AFM images. *Methods* **193**, 68–79 (2021).
357. Chen, Z. & Schmid, S. L. Evolving models for assembling and shaping clathrin-coated pits. *Journal of Cell Biology* **219**, (2020).
358. Marchesi, A. *et al.* An ultra-wide scanner for large-area high-speed atomic force microscopy with megapixel resolution. *Sci Rep* **11**, 13003 (2021).
359. Schächtele, M., Kemmler, J., Rheinlaender, J. & Schäffer, T. E. Combined High-Speed Atomic Force and Optical Microscopy Shows That Viscoelastic Properties of Melanoma Cancer Cells Change during the Cell Cycle. *Advanced Materials Technologies* **7**, 2101000 (2022).
360. Jones, S. A., Shim, S.-H., He, J. & Zhuang, X. Fast, three-dimensional super-resolution imaging of live cells. *Nature Methods* **8**, 499–505 (2011).
361. Zhou, L., Cai, M., Tong, T. & Wang, H. Progress in the Correlative Atomic Force Microscopy and Optical Microscopy. *Sensors (Basel)* **17**, (2017).
362. Nanosurf Studio - Nanosurf. <https://www.nanosurf.com/en/software/listing-nsf-studio>.
363. He, Y., Chen, Y., Liu, H., Ribbe, A. E. & Mao, C. Self-assembly of hexagonal DNA two-dimensional (2D) arrays. *Journal of the American Chemical Society* **127**, 12202–12203 (2005).

364. Fricke, E. L. Gwyddion File Importer.
<https://www.mathworks.com/matlabcentral/fileexchange/32893-gwyddion-file-importer>
(2011).
365. Inc., T. M. MATLAB version: 9.13.0 (R2022b). Preprint at (2022).
366. No Title. http://www.ks.uiuc.edu/Research/vmd/mailling_list/vmd-l/att-32062/system_freeze.vmd.
367. Hedges, L. O. LibVMMC.
368. Kern, N. & Frenkel, D. Fluid-fluid coexistence in colloidal systems with short-ranged strongly directional attraction. *Journal of Chemical Physics* **118**, 9882–9889 (2003).
369. Frenkel, D. & Smit, B. Understanding molecular simulation: From algorithms to applications. *Understanding molecular simulation: From algorithms to applications* **50**, (1996).
370. Poppleton, E. *et al.* Design, optimization and analysis of large DNA and RNA nanostructures through interactive visualization, editing and molecular simulation. *Nucleic Acids Research* **48**, E72–E72 (2020).
371. Bohlin, J. *et al.* Design and simulation of DNA, RNA and hybrid protein–nucleic acid nanostructures with oxView. *Nature Protocols* **17**, 1762–1788 (2022).

Curriculum Vitae

Veronika Cencen

Nationality: Slovenian Date of birth: 30/09/1993

Email address: veronika.cencen.2@gmail.com Phone number: (+41) 0763818370

Home: Avenue du silo 5, 1020 Renens (Switzerland)

WORK EXPERIENCE

Application Scientist (Intern)

Nanosurf [09/2021 – 10/2022] Basel, Switzerland

- Assisted in product development and testing
- Bio-sample preparation and imaging

Visiting Research Fellow

Princeton University [07/2016 – 12/2016] Princeton, USA

- Developing a mathematical model for particle entry into mammalian cells

Intern

TMG-BMC [07/2012 – 07/2013] Ljubljana, Slovenia

- Recruitment of contacts for biomedical company

EDUCATION AND TRAINING

PhD in Bioengineering

EPFL (École Polytechnique Fédérale de Lausanne) [01/09/2018 – 18/01/2024]

Lausanne, Switzerland

Thesis: Advancements in Nanomechanical Characterization and Biomolecular Imaging with Atomic force Microscopy

M.A.Sc. in Biomedical Engineering

University of Ottawa [09/2014 – 12/2016]

Ottawa, Canada

Thesis: A Microfluidic Device for Transfection of Mammalian Cells Using Adjustable Shear Stress

B.Sc. in Biotechnology

University of Ljubljana [10/2011 – 07/2014]

Ljubljana, Slovenia

Thesis: Biotechnological approaches to the development of new therapies for treating obesity

LANGUAGES

Mother tongue(s): Slovenian | English

Other language(s): French B1 Russian A1 Chinese A1

SKILLS

Light and Fluorescence Microscopy / Electron Microscopy / Immunofluorescence / Microfabrication techniques such as Photolithography / Matlab/Simulink / Python / Cell Culture / Biosafety Level 2 practices / Atomic Force Microscopy / University Teaching

HOBBIES AND INTERESTS

Rhythmic gymnastics (former national team), trail running, ballet/modern dance, travel photography